



**Università degli Studi di Genova  
Facoltà di Ingegneria Meccanica**

**DITEC**

**Dipartimento di Termoeenergetica e Condizionamento Ambientale**

**A.A. 2001 / 2002**

**Tesi di Laurea**

**Experimental Investigation of Magnetohydrodynamics Effects in  
Molten Metals and Study of Homogeneity of Radioactive Mercury  
Amalgams**

**Relatore: Chiar.mo Prof. Ing. Claudio Pisoni**

**Allievo: Andrea Astone**



**Andrea Astone**

***Thesis***



## *Abstract*

### **Towards a High Power Proton Target**

The high neutrino output demanded for a neutrino factory requests a high power proton beam interacting with a static target. The additional circumstances of limited space and long term stability ask for development of novel concepts for such types of targets.

In our working group, part of the Neutrino Factory Working Group (NFWG) of CERN, we are investigating on the proton interaction with the mercury target. This is called the study of proton induced shocks in molten metal. In the US scheme for a neutrino factory the interaction between proton beam and the mercury jet target takes place inside a 20 Tesla solenoidal magnetic field, which serves as a focusing device for the produced particles. This field of study is referred to as Magneto Hydrodynamics (MHD).

The high power proton beam deposits a large amount of energy in the small volume of the target, which results in disruption. The aim is to establish experiments to study this phenomenon and to quantify the impact on the overall design of the target area. Shooting a high intensity proton beam into a steady mercury target is to subsequently observe the effects of the thermal shock induced by the energy deposition in the material. This experiment is part of a global study over high power proton target, which includes also the experiment performed at BNL [9] in spring 2001 to achieve more detailed results and to use the different proton energy of 2.2 GeV. Experiments are requested in order to deliver bench marks for numerical simulations [34].

The second part of the work aimed to investigate magneto-hydro-dynamic effects occurring in the target area. Injecting the liquid metal target at a speed of more than 10 m/s into a 20 Tesla solenoidal magnetic field causes forces on the liquid. The repulsion and pinching of the liquid jet will be studied experimentally. Numerical simulations will be compared with these results [35].

By the superposition of results achieved from these two experiments the feasibility of using a liquid metal target for a neutrino factory will be derived.

The third part of the thesis work concerns the development of a technique for radioactive mercury handling and disposal. A final design of a neutrino factory will produce a certain amount of radioactive mercury, which might be destined for disposal/storage. After separation of radioactive mercury by distillation the radioactive part could be stored. Storage could only be handled after solidification of it. The procedure chosen for solidification is to produce amalgam from the radioactive mercury. Small quantities for justification of the method are available from experiments at ISOLDE. As the quantity of used mercury will be relevant, the procedure developed will become the starting point of a production of industrial scale.

# Table of contents

## Part I

### Chapter 1

<b>The C.E.R.N</b>	<b>1</b>
1.1 What is C.E.R.N.	1
1.2 Exploration of the structure of matter	2
1.2.1 LINAC	3
1.2.2 Synchrotron	4
1.3 Elements of particle physics	7
1.3.1 What is matter made of?	7
1.3.2 Quarks	8
1.3.3 Leptons	9
1.3.4 Interactions	10
1.4 What holds matter together?	10
1.4.1 Hadrons	11
1.5 Anti particles, antimatter	12

### Chapter 2

<b>The Neutrino</b>	<b>13</b>
2.1 Neutrino history	13
2.2 What is a Neutrino?	15



2.3 Neutrino production	15
2.4 Neutrino oscillations	17
2.4.1 The solar neutrino problem	17
2.4.2 Neutrino oscillation parameterization	18
2.5 Neutrino detection	19
2.6 Achievement related to neutrino oscillations measurement	20
2.7 Why do we need an additional neutrino source?	20
2.7.1 Beam prerequisites	21
2.8 Neutrino Factory layout	22
2.8.1 Proton source	23
2.8.2 Accumulator ring and bunch compressor	23
2.8.3 Target	24
2.8.4 Transverse collection	26
2.8.5 Pion decay and phase rotation	28
2.8.6 Transverse cooling	29
2.8.7 Muon acceleration and decay	29

## Part II

### Thesis overview and aims

### Chapter 3

<b>Proton Induced Thermal Shocks in Molten Metal</b>	<b>30</b>
3.1 The ISOLDE facility	30
3.2 Experimental Set Up	32
3.2.1 The target	33
3.2.2 High-speed camera system	36
3.2.3 Trigger	37

3.2.4 Light source	39
3.3 Set up in ISOLDE target area	40
3.4 Beam parameters	41
3.5 Extracting Initial Explosion Velocities	43
3.6 Results' explanation	54
3.6.1 Number of protons	56
3.6.2 Spot size influence	57
3.6.3 Pulse length influence	57
3.6.4 Vertical scan effect	58
3.7 Jet's behavior analysis	59
3.7.1 Positions	62
3.7.2 Velocities	63
3.7.3 Jet shape analysis	64
3.8 Conclusions	66

## **Chapter 4**

<b>Interaction between a Mercury Jet and Magnetic Field</b>	<b>67</b>
4.1 Introduction	67
4.1.1 Magneto Hydrodynamics	67
4.1.2 Previous experiments	68
4.2 The experimental set up	68
4.2.1 The magnet	69
4.2.2 Concepts of the experimental set up	71
4.2.3 Flowchart	71
4.2.4 Pumping System	74
4.2.5 Jet Chamber	76
4.2.6 Acquisition system and optics	78
4.2.7 Mercury recovery system	79
4.3 Performance at GHMFL	82
4.4 Analysis	82

4.5 Conclusions and next tests	87
--------------------------------	----

## **Chapter 5**

### **Study of Homogeneity on Experimental Amalgams for Mercury Waste Consolidation 90**

5.1 Radioactivity	90
5.2 Aims of the study and motivations	91
5.3 Equipment	92
5.3.1 The capsule	92
5.3.2 Amalgamator	94
5.3.3 Precision balance	95
5.4 Test procedure and samples preparation	95
5.5 Optical microscope analysis	96
5.5.1 Samples preparation	96
5.5.2 Results	97
5.6 Scanning Electron Microscopy analysis	103
5.6.1 Amalgam powder observation	103
5.6.2 Amalgam samples analysis	105
5.7 EDS mapping analysis	110
5.7.1 Results	116
5.8 Samples observation in time	117
5.9 Micro hardness test	119
5.10 Conclusions	120

## **Bibliography 122**

## **Appendix 126**

## **Abbreviations 146**

## **Part I**

### **Introduction to the field of study**

# Chapter 1

## Introduction

### 1.1 What is C.E.R.N.

The European Center for Nuclear Research CERN is the European Laboratory for Particle Physics, the world's largest particle physics research center. Founded in 1954, the laboratory was one of the Europe's first joint ventures, and has become a shining example of international collaboration.

From the initial 12 signatories of the CERN convention, membership has grown to the present 20 Member States. The laboratory sits astride Franco-Swiss border west of Geneva at the foot of the Jura Mountains (Fig 1.1).



*Fig. 1.1: CERN's aerial prospective*

Fundamental research is CERN's reason of being, but the Laboratory also plays a vital role in developing the technologies of tomorrow. From materials science to computing, particle physics demands the ultimate in performance, making CERN an important test-bed for industry.

CERN's role is providing high-energy particles beams to scientists who use them for their experiments. The Laboratory is equipped with a complex of interlinked particles accelerators, who deliver beams of electrons, protons and ions as well as secondary beams composed of more exotic particles like positrons and antiprotons for all kind of experiment.

Those beams provided by CERN are used to explore matter at very high energies corresponding to the temperatures of the Big Bang era. Therefore CERN's scientists study millions of those events in trying to understand how, 15 billions of years ago, after its birth, Universe looked like.

## 1.2 Exploration of the structure of matter

For investigating matter's structure very special accelerators and detectors are necessary. These machines, accelerate particles to very high energy and make them dash together or against fixed targets allowing physicists to detect and discover new particles and forces that act among those particles. Two main families of accelerators are used for this purpose: circular (Figure 1.2) and linear (Figure 1.3). They exploit high intensity electric fields for accelerating charged particles to high energies. The longer a linac (linear accelerator) is, the higher the energy of the particles it can produce. A synchrotron (circular accelerator) achieves high energy by circulating particles several times before they hit their targets. Beam focusing and deviation, for circular accelerators, is provided by magnetic fields.

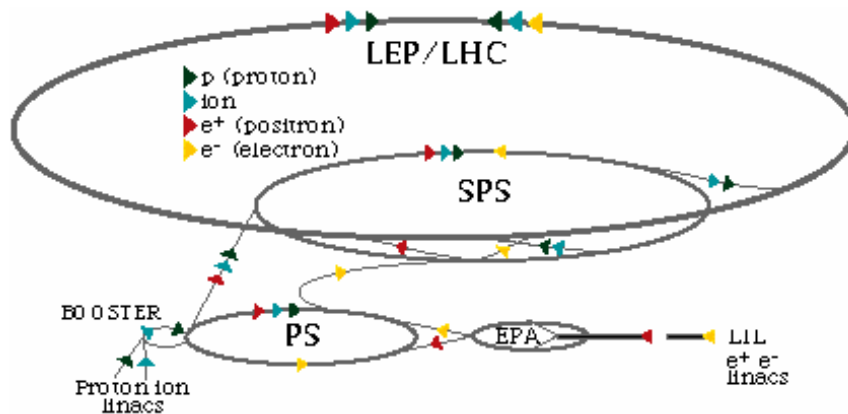


*Fig 1.2: CERN's accelerators chain: LINACs, Booster, PS, SPS and LEP/LHC synchrotrons*



*Fig 1.3: CERN's Linac*

Making particle colliding either in accelerators (for this reason called colliders) or smashing in fixed targets, new particles are produced. According to the famous Einstein's equation  $E=mc^2$  (where  $E$  is energy,  $m$  is mass and  $c$  is light's speed), matter is transformed in energy and energy in matter. Particles investigated by CERN have got very low energy (roughly  $10^{-6}$  J), but confined in a very small space: those energy concentrations yield in fact new particles, instable that can be studied and investigated for better understanding nature.

### 1.2.1 LINAC

A LINear ACcelerator, is a particle accelerator which accelerates charged particles - electrons, protons or heavy ions - in a straight line.

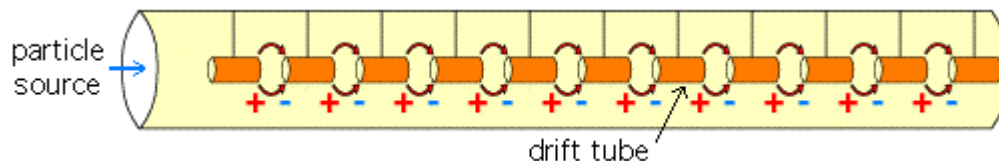


*Fig. 1.4: Linac, operation principle*

The drift tubes are necessary because an alternating field is used and without them, the field would alternately accelerate and decelerate the particles (Figure 1.4 and 1.5). The drift tubes shield the particles for the length of time that the field would be decelerating.

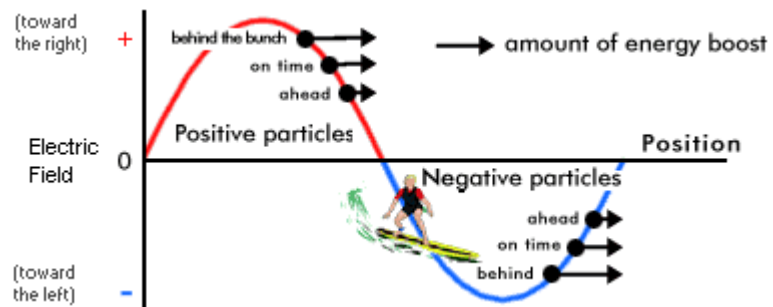


*Fig. 1.5: Electric field influence on a particle*

Charged particles enter on the left and are accelerated towards the first drift tube by an electric field. Once inside the drift tube, they are shielded from the field and drift through at a constant velocity. When they arrive at the next gap, the field accelerates them again until they reach the next drift tube. This continues, with the particles picking up more and more energy in each gap, until they exit the accelerator.

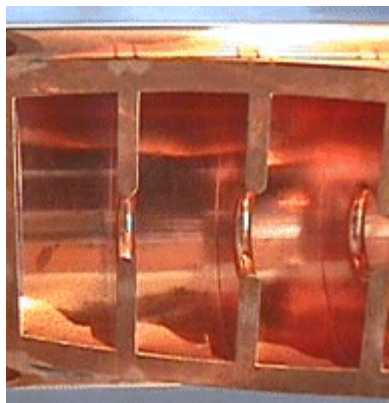


*Fig. 1.6: Cut of a beam pipe in LINAC*

### 1.2.2 Synchrotron

After eleven years operation, CERN's largest accelerator is LEP (Large Electron Positron collider), is now dismantled. It is a 27 km circumference ring that will be replaced by LHC (Large Hadron Collider) in the next future and represents CERN's biggest experiments of the last years.



The Large Electron Positron collider (LEP) was the biggest particle accelerator in the world. Housed deep underground at about 100 m depth, LEP collides electrons with positrons, inside its four particles detectors (Aleph, Delphi, L3, and Opal) which probe the electromagnetic and weak forces in minute detail.

Each of the detectors has been optimized differently to study various physics aspects. LEP was designed to study the electro-weak force, the mechanism that fuels the sun and is responsible for some forms of natural radioactivity. The weak force is carried between particles of matter by “messenger-particles” called  $W^+$ ,  $W^-$  and  $Z$ . In its first phase from 1989 to 1995, LEP achieved collision energies high enough to produce the  $Z$ . In its second phase, known as LEP 2 which began in 1996, LEP ran at twice this energy (105 GeV<sup>1</sup>), sufficient to produce  $W^+$  and  $W^-$  in pairs, completing studies of the weak force. Detection of millions of  $Z_0$  and hundreds of  $W$  has allowed the LEP experiments to make extremely precise tests of the Standard Model of particles and their interactions.

CERN's next big machine, due to start operating in 2006, is the Large Hadron Collider (LHC). LHC will be the last link of a chain of accelerators that already exist at CERN: Proton Synchrotron (PS), the laboratory's first proton accelerator built some 40 years ago and the Super Proton Synchrotron (SPS) which was constructed during the 1970s. These facilities will be exploited as injectors for LHC beams and will provide particles a first acceleration. LHC will substitute LEP and will be theater of next CERN's challenges. It is now under construction and will fit in LEP's tunnel and will operate at such high energies as 7 TeV; at those energies, theory strongly indicates that answers to some of the remaining questions will begin to emerge. It will be an accelerator which will bring protons into head-on collision at higher energies than ever achieved before to allow scientists to penetrate still further into the structure of matter and recreate the conditions prevailing in the Universe just  $10^{-12}$  seconds after the "Big Bang".

All along LHC's ring will be installed four detectors (Atlas, CMS, Alice and LHCb) each one with different aims. These detectors, or as they are called “experiments”, are enormous devices deeply buried underground. For their construction mighty works of civil engineering have begun to be erected, it means that tunnels, broad and deep wells and underground chambers to host those facilities are under construction.

One of the main goals of ATLAS (and LHC) program is to discover and study the Higgs particle. The search for the Higgs boson has already begun at the LEP collider. The Higgs particle is of critical importance in particle theories and is directly related to the concept of particle mass and therefore to all masses. The ATLAS detector at the LHC will be able to detect this particle if it exists.

Finding and studying Quark Gluon Plasma is ALICE's goal via collision of heavy ions in the LHC tunnel. Scientists believe there was a Big Bang from which everything in the Universe emerged. Fifteen billion years later, the Universe is so huge that it would take light billions of years to cross. All the particles which make up everyday matter, from which we and everything around us are made, had yet to form. The quarks and gluons, which in today's cold

---

<sup>1</sup> A GeV, or giga electron volt, is a unit of energy and it is also used as a unit of mass. Mass ( $m$ ) is just a form of energy ( $E$ ), as Einstein showed in his equation  $E=mc^2$ ,  $c$  is a constant (the speed of light). When high-energy particle beams collide, new particles are formed as energy is converted into matter. A proton corresponds to an energy of 0.938 GeV and its mass is 0.938 GeV/c [1].

Universe are locked up inside protons and neutrons, would have been too hot to stick together; matter in this state is called Quark Gluon Plasma.

LHCb experiment aims to find out the reason why, during the Big Bang, when equal amounts of matter and antimatter were created, antimatter disappeared and only matter remained.

The last experiment approved up to now for LHC project is CMS (Compact Muon Solenoid). The CMS detector will look for evidence of the theoretical Higgs particle, and is designed to recognize other particles that might function as alternative to the Higgs within the Standard Model.

Particle acceleration is not only a prerogative of LEP and LHC facilities, but it is used in other CERN's experiments as well. It is the case of the experiment called CNGS (CERN's Neutrino to Gran Sasso). This project, consists in producing a neutrino beam at CERN (basically of muon neutrino type) and sending it towards the Gran Sasso laboratory in Italy.

A beam of this type is generated from collision of protons and neutrons, in a graphite target, focusing the particles (pions and kaons in particular) in the desired direction. The pions and kaons decay in a flight at high energies. Muons, the products of such decay, by inertia continue to travel in generally the same direction as the particles that generated them. To direct neutrino to Gran Sasso, all that need to be done is to focus the pions and kaons in that direction (Figure 1.7). The decay of these particles in a vacuum tunnel of about one kilometer length creates the neutrino beam.

Because the low interaction with matter the most of neutrinos so produced will reach the target in Gran Sasso, Italy.



**Fig. 1.7: CNGS underground structure**

But why do we need to accelerate particles to such high energies? In collisions involving high-energy particles, some of the kinetic energy can be used to transform into new particles ( $E=mc^2$  means energy can be transformed into mass). The more massive the new particles, the larger the incoming energy must be to create them.

In recent years physicists have pushed to higher and higher energies, because much of the complexity observed at low energies may disappear when the energy becomes sufficiently high. Thus while  $\beta$  radioactivity and electromagnetism have been separately known for 100 years, it is only in the last 25 years that particle accelerators have provided beam energies sufficiently high to "unmask" the fundamental relationship between the two phenomena.

### 1.3 Elements of particle physics

#### 1.3.1 What is matter made of?

Particle physics: what is it? Particle physics is something different from the usual concept of physics, engineers are used to. Usually, while thinking about physics, one immediately thinks about mechanics, thermodynamics or electromagnetism, but physics is not only this, it is also particle physics and astronomy, is something that goes further common knowledge.

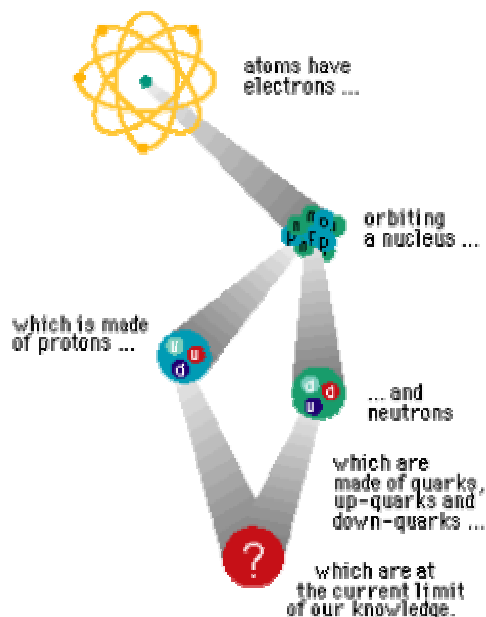


*Fig.1.8: Atoms' structure: beyond protons and neutrons*

This is a completely new universe that opens in front of new visitors that come in contact with CERN's environment. This is a little bit astonishing as engineers' field of study is related to a different scale of phenomenon. Therefore it is not so simple to get used to such a big quantity of new terms, concepts and measurement units referred to something that for an inexperienced eye could look like a labyrinth.

Particle's physics aim is to investigate matter's structure and to figure out laws who govern universe. This means that cosmology as well is involved in its dominion.

Protons, neutrons, electrons, are matter's basics structure components, however as illustrated in Figure 1.8, it is demonstrated that protons as well as neutrons are composite particles. Particle physics is the study of the basic particles of matter and the forces that act upon them. It also looks at how matter evolved in the Universe, especially in the first seconds of the Big Bang.

Dividing all particles in two main groups could make a first brief classification: Quarks and Leptons; these are the matter particles of the current Standard Model [2]. Today's firm belief is that ordinary matter is composed of only four building blocks. Those blocks are called up-quarks, down-quarks, electrons and electron-neutrinos.

### 1.3.2 Quarks

Quarks are in number of six and are respectively: up-quark, down-quark, charm-quark, strange quark, top-quark and bottom-quark (Table 1.1) [3]. They are quite different one from each other especially while looking at their mass. "Up", "down" and "strange" quarks, in fact are lighter than their fellows who are more massive than particles like proton. The weight scale increases passing from charm quark that weights nearly 1.5 time a proton to bottom quark about 5 times heavier up to top quark which is heavier than a factor 100. Nevertheless quark mass cannot be measured directly, but must be determined indirectly through their influence on Hadron properties.

*Table 1.1: Quarks*

Quarks	Mass (Gev/c <sup>2</sup> )	Electric Charge
U (up)	.005	+2/3
D (down)	.01	-1/3
C (charm)	1.5	+2/3
S (strange)	0.2	-1/3
T (top)	180	+2/3
B (bottom)	4.7	-1/3

Up-quarks and down-quarks are embedded inside protons and neutrons in atomic nucleus.

The electron seems to have no internal structure. However, the nucleons are composite particles, each containing three quarks. Like the electron, the quarks seem to have no structure. Only two types of quark, up-quark and down-quark, are needed to build the proton and the neutron. They have charges of  $+2/3$  and  $-1/3$  compared with the electron's charge of  $-1$  [4]. Other heavy particles produced in high energy collisions are composites, built from quarks, like the proton. However, these particles are much heavier because they include heavy quarks, which can be produced only at the higher energies. There are three heavier quarks called "charm", "bottom" and "top", which bring the total number of quarks to six.

### 1.3.3 Leptons

Six leptons are known: electron, electron-neutrino, muon, muon-neutrino, tau and tau-neutrino. These particles, unlike quarks are not confined inside Hadrons and are observed as physical particles as shown in Table 1.2.

The electron has a mass of  $0.000511 \text{ GeV}/c^2$  [5]. The electron is the least massive charged particle of any type. It is absolutely stable because conservation of energy and electric charge together forbid any decay.

The muons have a mass of  $0.106 \text{ GeV}/c^2$ . These are just like the electron but 210 times heavier. But unlike electrons, muons leave an average time of 2.2 microseconds. A muon will change into an electron, a  $\bar{\nu}_e$  and a  $\nu_\mu$ , shedding its extra mass as kinetic energy shared between the electron and two neutrinos. One of these is an anti electron-neutrino, related to the electron, while the other is a muon-neutrino, which is like a very light (possible massless) neutral version of the muon.

Muons readily pass through the electric fields inside matter with very little deflection. So, muons do not radiate and slow down as electrons do. However, they can cause ionization and this makes them readily detectable in matter, for example, with a Geiger counter.

**Tab. 1.2: Leptons**

Particle	Mass (Gev/c <sup>2</sup> )	Electr. Charge
electron-neutrino	$<2.2 \times 10^{-9}$	0
electron	.000511	-1
muon-neutrino	$<.00017$	0
muon	0.106	-1
tau-neutrino	$<.015$	0
tau	1.7771	-1

Tau ( $\tau$ ) lepton is also unstable. It is 3550 times heavier than the electron, and lives  $0.3 \text{ ps}^2$ . The tau-minus decays to produce its matching neutrino and a virtual W-minus boson. The tau can decay into the lighter electron or muon, or even to the particles known as pions. Whichever way it decays, it always produces its neutral lightweight counterpart, the tau-neutrino.

One more structureless particle must be added to complete the picture. This is a neutral and very light particle called the electron-neutrino, which behaves like an electron with no charge. Its name is electron-neutrino.

### 1.3.4 Interactions

The various matter and force-carrying particles weigh in with a wide range of masses. The photon, carrier of the electromagnetic force, and the gluons that carry the strong force, are massless, while the conveyors of the weak force, the  $W$  and  $Z$  particles, each weigh as much as 80 to 90 protons or as much as a reasonably sized nucleus. The most massive fundamental particle found so far is the top quark. It is twice as heavy as the  $W$  and  $Z$  particles, and weighs about the same as a nucleus of gold. The electron, on the other hand, is approximately 350,000 times lighter than the top quark, and the neutrinos may even have no mass at all.

Why there is such a range of masses is one of the remaining puzzles of particle physics. Indeed, how particles get masses at all is not yet properly understood. In the theories of Standard Model of electro-weak and strong interactions, all particles are massless, so something has to be introduced to explain their various weights. In the Standard Model, the particles acquire their masses through a mechanism named after theorist Peter Higgs. According to the theory, all the matter particles and force carriers interact with another particle, known as the Higgs boson. It is the strength of this interaction that gives rise to what we call mass: the stronger the interaction, the greater the mass.

## 1.4 What holds matter together?

Another fundamental concept is required to explain how matter is structured and that is, how do all those complex structures can hold together. They do this through only a few basic interactions, which we can think of as forces.

The present understand of physicists is that only four forces mediate all interactions between matter [6]. These are: electromagnetism, strong nuclear forces, weak nuclear forces and gravity.

Two of them (electromagnetism and weak nuclear force) have been unified into a more general force which describes both as different sides of the same coin. Unification of the third, strong nuclear force with these two is greatly auspicate within a “grand unified theory”. The fourth force, gravity remains resistant to theoretical unification with the other three.

Gravity, inextricably bound up with the question of mass, is one of the main reasons for excitement over the announcement of discovery of neutrino mass.

---

<sup>2</sup>  $1 \text{ ps} \rightarrow 10^{-12} \text{ s}$

The basic forces, or interactions, between the particles of matter all act through a "force carrier", which is exchanged between the interacting particles. In this way, interactions between particles can either bring the particles together (an attractive force) or push them apart (a repulsive force). There is a different type of carrier for each of the basic forces (although the existence of the carrier for gravity, called the graviton, has yet to be demonstrated experimentally and has only foreseen theoretically).

Photons, the "particles" of light, carry the electromagnetic force. The photons have no mass and no electric charge, and can be exchanged over large distances so that the electromagnetic force is infinite in range.

The carriers of the weak force are called bosons and are represented by symbols  $W$  and  $Z$ . The  $W$  is electrically charged ( $W^+$  and  $W^-$ ), while the  $Z$  is neutral ( $Z^0$ ) [7]. These carriers are massive, each weighing about 100 times as much as a proton. This makes them difficult to exchange at low energies, so the weak force appears weak.

The carriers of the strong force are called gluons. They have no electric charge and no mass, but they carry a special charge-like property, called color, that gives them their power to hold quarks together so strongly that the quarks are never seen as individual particles. The resulting hadrons, such as protons, neutrons and pions, have no color charge. Hadrons are particles made from Quarks and/or gluons, bound together by their strong interactions.

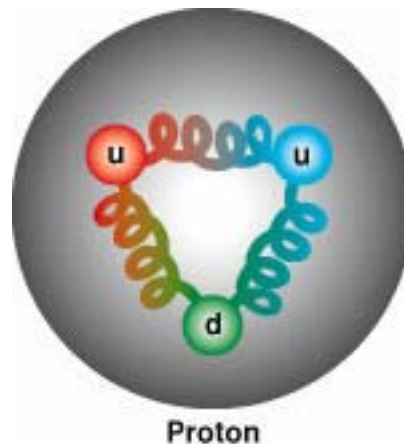


*Fig. 1.9: Structure of the proton: 3 gluons and 3 quarks*

### 1.4.1 Hadrons

The idea of the quarks was first proposed to explain the many observed hadrons. There are two classes of hadrons: baryons and mesons.

Baryons are particles made from a basic structure of three quarks. Baryons carry an odd half quantum unit of angular momentum (spin) and, hence, are fermions, which means that they obey the Pauli exclusion principle rules [8].

The proton is the only baryon that is stable in isolation. Its basic structure is two up quarks and one down quark as illustrated in figure 1.9 above. Neutrons are also baryons. Although neutrons are not stable in isolation, they can be stable inside certain nuclei. A neutron's basic structure is two down quarks and one up quark. More massive baryons may be made from any set of three quarks. Baryons containing more massive quarks are all unstable.

Mesons are color-neutral particles with a basic structure of one quark and one antiquark. There are no stable mesons. Mesons have integer (or zero) units of spin, and hence are Bosons, which means that they do not obey Pauli exclusion principle rules.

The most common mesons are: Pions, made from up and down type quarks and antiquarks only (for example, a pi-plus meson is a u and an anti-d quark).

## 1.5 Anti particles, antimatter

For each of the basic particles of matter, there also exists a specular version - or antiparticle - in which properties such as electric charge are reversed.

The common electron, for example, has negative charge, although its antiparticle, called the positron, has positive charge. In the same way the positively charged proton has a negatively charged antiparticle, the antiproton. Like the proton, the antiproton is a complex particle, but built from three antiquarks, with opposite charges to the quarks that form the proton.

Antiparticles are made in energetic process together with particles - whenever a particle is created, an antiparticle must also be made. This means that there must be sufficient initial energy to make all the mass of the particle and antiparticle, according to the equation  $E=mc^2$ . All kinds of particle-antiparticle pair can be made in this way, assuming that there is enough energy.

When a particle and antiparticle of the same kind meet they soon disappear into a burst of pure energy, in a process called annihilation. The energy released is equal to the total energy of the annihilating pair, including the mass-energy, given by the equation  $E=mc^2$ .

Normal matter in the world around us is built from two types of quark, called "up" and "down", which form neutrons and protons. It also requires two types of lepton: the electron and the electron-neutrino (which emerges for example in radioactive decays). This pattern repeats itself in two heavier "generations", each with two quarks and two leptons.

However, where did antimatter go? Experiments in particle physics show that matter and antimatter are created in equal quantities, indicating that this should also have been so during the extremely energetic conditions of the early Universe. But if that were so, why did the antimatter not completely annihilate the matter, leaving only energy (photons) in the Universe? It seems instead that there was some small but significant asymmetry between matter and antimatter.

The LHC, CERN's next machine, should readily produce particles containing the heavier "bottom" quarks of the third generation. Particles containing bottom quarks should also reveal the symmetry breaking effect of CP violation.



## Chapter 2

### The neutrino

#### 2.1 Neutrino history

The first intuition about neutrino existence was in 1896. In this date H. Becquerel [9] observed a phenomenon that is now explained assuming that neutrinos exist: the “nuclear  $\beta$  decay”.

Becquerel observed that uranium minerals emit radiation that remain impressed in photographic emulsions [10]. During this process, elementary particles are created apparently from nothing and the chemical element emitting them is spontaneously transformed into a different element. Following Becquerel's discovery, these emissions were called  $\beta$  rays, hence the name given to the decay.

Radioactivity was understood as a two-body decay in which the initial nucleus  $I$  decayed into into the final nucleus  $N$  plus the decay products, an electron  $e^-$  in the case of  $\beta$ -decay.

$$I \rightarrow F + e^-$$

In  $\beta$  decays, the available energy  $E$  comes from the mass difference  $\Delta m$  between the initial and final nuclei, according to equation  $E = (\Delta m) \cdot c^2$ . The energy of the visible particle that is emitted (an electron or a positron) varies in each event. The enigma to be solved was to understand where does the missing energy go. The problem with this interpretation was that it was not compatible with the observed energy spectrum of the electrons in the case of the  $\beta$ -decay.

When a neutron is transmuted into a proton, the conservation of the total electric charge requires that a particle with the same charge as an electron (equal and opposite to the proton's) is emitted. Indeed an electron is emitted or, in inverse transmutation, a positron, with opposite charge. Only later it became clear that they were electrons or positrons.

A two body decay cannot explain the continuous spectrum and a third particle had not be observed. As an extreme remedy to explain this enigma, W. Pauli in 1930 first postulated that there must be a third particle: the neutrino particle (indicated as  $\nu$ ) [11]. This particle, would take away the apparently missing energy. With three particles, the continuous energy spectrum can be explained.

Further steps in neutrino's history have been:

- 1934 - Enrico Fermi develops a comprehensive theory of radioactive decays, including Pauli's hypothetical particle, which Fermi coins the neutrino.
- 1959 - Discovery of a particle fitting the expected characteristics of the neutrino is announced by Clyde Cowan and Fred Reines. This neutrino is later determined to be the partner of the electron.
- 1962 - Experiments at Brookhaven National Laboratory and CERN, make a surprising discovery: neutrinos produced in association with muons do not behave the same as those produced in association with electrons. They have, in fact, discovered a second type of neutrino (the muon neutrino).
- 1968 - The first experiment to detect (electron) neutrinos produced by the Sun's burning reports that less than half the expected neutrinos are observed. This is the origin of the long-standing "solar neutrino problem." The possibility that the missing electron neutrinos may have transformed into another type is soon suggested, but unreliability of the solar model on which the expected neutrino rates are based is initially considered a more likely explanation.
- 1978 - The tau particle is discovered at SLAC, the Stanford Linear Accelerator Center. It is soon recognized to be a heavier version of the electron and muon, and its decay exhibits the same apparent imbalance of energy and momentum that led Pauli to predict the existence of the neutrino. The existence of a third neutrino associated with the tau is hence inferred, although this neutrino has yet to be directly observed.
- 1985 - A Russian team reports measurement, for the first time, of a non-zero neutrino mass, but subsequent attempts to independently reproduce the measurement do not succeed.
- 1988 - Kamiokande, another water detector looking for proton decay but better able to distinguish muon neutrino interactions from those of electron neutrino, reports that they observe only about 60% of the expected number of solar-neutrino interactions.
- 1989 - Experiments at CERN's Large Electron-Positron (LEP) accelerator determine that no additional light neutrinos beyond the three already known can exist.
- The first report of strong evidence for neutrino oscillations in atmospheric neutrino data by the Super-K collaboration in 1998 [12]. Although neutrino deficit had been observed for some time, it was this experiment that showed with high statistical significance that this deficit depends on the path length and energy of the neutrino.
- Upper limit of the  $\nu_e$  mass was found to be  $mc^2 \leq 2.5$  eV by Lobashev et al. in 1999 [13].
- Upper limit of the  $\nu_\tau$  mass was found to be  $mc^2 \leq 15.5$  MeV established by LEP [14].
- In 2000 the discovery of the  $\tau$  neutrino at the DONUT (Direct Observation of the Nu Tau) experiment at Fermilab [15].

Despite its long history, the neutrino still leaves unsolved enigmas, whose implications to astrophysics and cosmology make this particle all the more interesting.

## 2.2 What is a Neutrino?

Among elementary particles, the neutrino is the most mysterious one. It is very difficult to observe, its dimensions are difficult to detect and its mass extremely small.

As mentioned in section 1.3.3, in the Standard Model leptons are described three left-handed flavor doublets

$$\begin{pmatrix} e \\ \nu_e \end{pmatrix}_L \quad \begin{pmatrix} \mu \\ \nu_\mu \end{pmatrix}_L \quad \begin{pmatrix} \tau \\ \nu_\tau \end{pmatrix}_L.$$

All these particles have already been observed. The definition of flavor eigenstates is an experimental one. It is based on what we can “see” using a detector - this means it is based on the neutrino interaction with matter. We have no access to what the neutrino really “is”, we can only watch it interact. This means that we only identify a particle (in this case a neutrino) by the way it interacts with matter. This superficial view leads to interesting phenomena as neutrino oscillation (see section 2.4). Neutrino oscillations are manifestations of the fact that what we see is not the whole picture of the particle, but only a projection of its wave function on the flavor eigenstates. Experiments based on accelerators and others using reactors and radioactive sources have so far only yielded upper limits on neutrino masses (see Table 2.1).

**Tab. 2.1: Upper limits of the neutrino masses [22]**

Neutrino flavor	$mc^2$
$\nu_e$	$< 2.2\text{eV}$
$\nu_\mu$	$< 170\text{keV}$
$\nu_\tau$	$< 15.5\text{MeV}$

The fact that there are only three light lepton generations has been verified by measurements of the width of the  $Z^0$  boson peak at LEP [16]. Neutrinos only take part in the weak interaction.

## 2.3 Neutrino production

Neutrinos are decay products. As the neutrino participates only in the weak force, the only way to produce them is through a weak decay:

- The weak decay of  $n$  in nuclei and of free  $n$  ( $\beta$ -decay):

$$n \rightarrow p + e^{-} + \bar{\nu}_e$$

- The pion decay chain:

$$\pi^{+} \rightarrow \mu^{+} + \nu_{\mu}$$

$$\mu^{+} \rightarrow e^{+} + \bar{\nu}_{\mu} + \nu_e$$

$$\pi^{-} \rightarrow \mu^{-} + \bar{\nu}_{\mu}$$

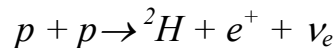
$$\mu^{-} \rightarrow e^{-} + \nu_{\mu} + \bar{\nu}_e .$$

Neutrinos are furthermore produced in kaon and tau decay.

There are several processes in which neutrinos are produced [17]. In nature they are abundantly created in the core of stars and in particular of Sun, during the nuclear reactions originating the electromagnetic radiation.

The neutrinos in the universe come from weak interactions (like beta decays in atomic nuclei). Three kinds can be distinguished: the neutrinos from space, the neutrinos from the earth, the neutrinos from mankind activity. But there are many types of neutrinos origins, which can be quite arbitrarily classified in five sources: solar neutrinos, neutrinos from mankind activity, neutrinos from the earth, neutrinos from cosmic rays and neutrinos from the Big-Bang.

Solar neutrinos come along with the process of thermonuclear fusion inside the stars (our sun or any other star in the universe). Their energy some MeV and they come from different nuclear reactions whose main reaction is:



where  $p$  is a proton,  $H$  is a deuterium nucleus,  $e^{+}$  is an anti-electron and  $\nu_e$  an electron-neutrino. The majority (85%) of neutrino is produced following this reaction.

Man produced neutrinos, are high energy neutrinos produced by particles accelerators and low energy neutrinos coming from nuclear reactors. The first ones, whose energy can reach about 100 GeV, are produced to study the structure of the nuclei and the weak interaction. The second ones although we did not ask for them, are an abundant product from the nuclear reactions inside the reactors cores (a standard nuclear plant radiates about  $5 \cdot 10^{20}$  neutrinos per second) and their energy is around 4 MeV. They have been the first to be detected and the first to be used to put some limits on the neutrino oscillation.

Our planet contains radioactive atomic materials not originating from human activity. This is what we call natural radioactivity or what we consider neutrinos coming from earth. The power coming from this natural radioactivity is estimated at about  $20 \text{ TW}^1$  and the neutrinos coming from this radioactivity are numerous: about  $6 \times 10^6$  per s /  $\text{cm}^2$ .

Other neutrinos come from cosmic rays well as muons. Under the same principle which guides the neutrinos production at CERN, called  $\pi$ -decay, some neutrinos are created: they are called "atmospheric neutrinos".

The last part of this classification includes neutrinos from the Big-Bang. The standard model of the Big-Bang predicts, like for the photons, a cosmic background of neutrinos. They are yet very numerous and their energy is theoretically about 0.0004 eV. No experiment, even very huge, has been able to detect them.

A neutrino factory produces neutrino similar to the way atmospheric neutrino are produced, but with two differences. The muons are accelerated so that the neutrino from the muon decay have on average higher energy then the neutrinos from the pion decay and the neutrino factory is sing selective, delivering only  $\mu^+$  or  $\mu^-$  and their neutrinos at given time.

## 2.4 Neutrino oscillations

Neutrino oscillations are a peculiar quantum mechanical effect, for which it is hard to find a good macroscopic analogy, as it has to do with the particle-wave duality of fundamental matter.

### 2.4.1 The solar neutrino problem

Our sun works as a thermonuclear reactor in which protons burn into helium and their heavier elements. Energy and neutrinos are produced in this process.

The standard solar model [18] describes the dependences between nuclear physics, gravitation, thermo- and fluidodynamycs of the sun. It is based on the assumption that (a) the sun is in hydrostatic and thermal equilibrium, (b) its energy is produced by fusion and that (c) the energy transport inside the sun is dominated by radiation.

This model predicts a neutrino flux of  $4 \times 10^{10} \nu_e / (s \text{ cm}^2)$  on earth. Only half of this value is measured on the earth. This difference between the measured and the predicted  $\nu_e$  flux from the sun is called "solar neutrino problem".

Now that the solar model is well established, and with evidence of neutrino oscillation from the atmospheric neutrino the most probable solution for the solar neutrino problem are neutrino oscillations. This means that the missing  $\nu_e$ 's oscillate into another neutrino flavor. Theory predicts that the oscillation probability depends on the distance. The neutrino anomaly has been confirmed in the late 90's confirmed by the Japanese experiment Super-Kamiokande. The results coming out from these experiments show evidence for a deficit of muon-type neutrino  $\nu_e$  in the atmospheric neutrino flux. This deficit varies with the zenith angle of the incident neutrinos, and hence varies with the distance between the source and the detector. The natural interpretation of this result is that the missing  $\nu_\mu$  have oscillated into another neutrino.

### 2.4.2 Neutrino oscillation parametrization

Whenever a neutrino is created or detected, this is due to weak force, so its weak (or flavor) eigenstates determines the process. Its propagation, on the other hand, is described by the Schrödinger equation, which has different eigenstates called mass eigenstates. So a neutrino is “born” in one flavor eigenstate. As soon as it starts propagating, the flavor eigenstate has to be projected on all three mass eigenstates. The superposition of the mass eigenstates is expressed using the mixing matrix  $U$ .

The matrix describing the neutrino mixing depends generically on four physical parameters: three angles ( $\theta_{12}$ ,  $\theta_{13}$  and  $\theta_{23}$ ) and a Cp-odd phase ( $\delta$ ). The challenge of future neutrino physics is to measure all these quantities.

Today we know about three neutrino flavors:  $\nu_e$ ,  $\nu_\mu$  and  $\nu_\tau$ . Within the framework of three neutrino oscillations, the flavor eigenstates are related to the mass eigenstates by a  $3 \times 3$  orthogonal matrix  $U$  [19]:

$$U = \begin{pmatrix} \nu_e \\ \nu_\mu \\ \nu_\tau \end{pmatrix} = \begin{pmatrix} u_{e1} & u_{e2} & u_{e3} \\ u_{\mu1} & u_{\mu2} & u_{\mu3} \\ u_{\tau1} & u_{\tau2} & u_{\tau3} \end{pmatrix} \begin{pmatrix} \nu_1 \\ \nu_2 \\ \nu_3 \end{pmatrix}$$

That can be parameterized in terms of three mixing angles  $\theta_{ij}$  and a complex phase  $\delta$ :

$$\begin{pmatrix} \nu_e \\ \nu_\mu \\ \nu_\tau \end{pmatrix} = \begin{pmatrix} (c_{12}c_{13}) & (s_{12}c_{13}) & (s_{13}e^{-i\delta}) \\ (-s_{12}c_{23} - c_{12}s_{23}s_{13}e^{i\delta}) & (c_{12}c_{23} - s_{12}s_{23}s_{13}e^{i\delta}) & (s_{23}c_{13}) \\ (s_{12}s_{23} - c_{12}c_{23}s_{13}e^{i\delta}) & (-c_{12}s_{23} - s_{12}c_{23}s_{13}e^{i\delta}) & (c_{23}c_{13}) \end{pmatrix} \begin{pmatrix} \nu_1 \\ \nu_2 \\ \nu_3 \end{pmatrix}$$

where  $c_{ij} = \cos \theta_{ij}$  and  $s_{ij} = \sin \theta_{ij}$ .

Oscillation probabilities, that is  $P(\nu_\alpha \rightarrow \nu_\beta)$ , for neutrino of energy  $E_\nu$  (GeV) propagating a long distance  $L$  (Km) in vacuum depend upon the time of flight (and hence the baseline  $L$ ), the  $\Delta m_{ij}^2$ , and  $U$  (and hence  $\theta_{12}$ ,  $\theta_{13}$  and  $\theta_{23}$  and  $\delta$ ). Here, the importance of the factor  $L / E_\nu$  can be seen. The oscillation modulates with  $L/E_\nu$ ; the higher is the energy, the wider is the oscillation pattern. Assuming that oscillation phenomenon driven by  $\Delta m_{12}^2$  are neglected:

$$P(\nu_e \rightarrow \nu_\mu) = \sin^2 \theta_{23} \sin^2 2\theta_{13} \sin^2 \left( 1.267 \Delta m_{32}^2 \frac{L}{E_\nu} \right)$$

$$P(\nu_e \rightarrow \nu_\tau) = \cos^2 \theta_{23} \sin^2 2\theta_{13} \sin^2 \left( 1.267 \Delta m_{32}^2 \frac{L}{E_\nu} \right)$$

$$P(\nu_\mu \rightarrow \nu_\tau) = \cos^4 \theta_{23} \sin^2 2\theta_{23} \sin^2 \left( 1.267 \Delta m_{32}^2 \frac{L}{E_\nu} \right)$$

The oscillating sinusoidal factor  $\sin^2 (1.267 \Delta m_{32}^2 L/E_\nu)$  depends however only on the magnitude of  $\Delta m_{32}^2$  parameter and not on its sign.

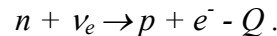
The flavors oscillations are driven by the differences in the squares of the masses  $m_j$ , that is:

$$\Delta m_{ij}^2 \equiv m_i^2 - m_j^2$$

## 2.5 Neutrino detection

Neutrinos are very difficult to detect because of their very low probability of interacting with matter because of they are subject to weak interaction only. Out of one hundred thousand solar neutrinos reaching the earth, all but one pass through the earth unnoticed. Hence, the probability that a neutrino interacts with an instrument is very low, thus its detection probability is so low. To make up for such a low probability, very massive and at the same time technically refined instruments are needed. Neutrinos can be detected through two different processes: the charged and neutral current.

The inverse  $\beta$ -decay is an example for the charged current. A neutron and a neutrino react to a proton and an electron. This reaction is endothermic so the energy  $Q$  is necessary to start it. Only neutrinos with a kinetic energy of at least  $Q$  can start this reaction and neutrinos with a lower energy cannot be detected.



The result is a beta active nucleus of a different element. With this method no information about direction or momentum is provided.

The other two detection methods, charged and neutral currents on electron, provide more information about neutrino's direction because the electron, that carries a fraction of neutrino momentum, is actually detected. From the direction and the momentum of the electron one can draw conclusions about the incident neutrino properties. Graphical representations of the reactions are shown in Figure 2.1.

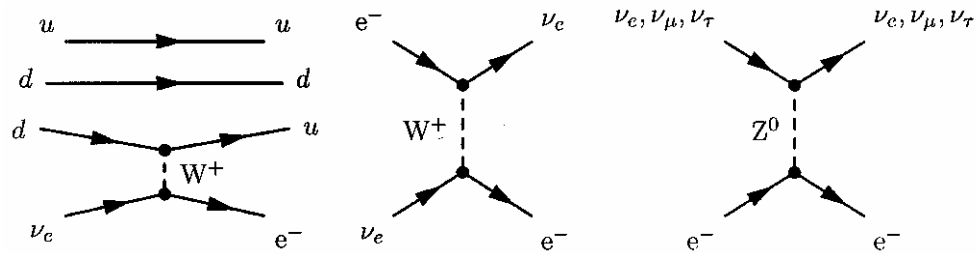


**Fig. 2.1: Feynman graphs for neutrino interaction involving detection; left: inverse  $\beta$ -decay; middle: charged currents reaction; right: neutral current reaction. In all cases a fraction of the momentum of the original neutrino is transferred to an electron.**

## 2.6 Achievement related to neutrino oscillations measurement

For a long time the three neutrino type were considered mass less, and thus immutable. Although those masses are almost negligible, of the order of a fraction of an eelectronvolt (see section 2.2), the consequence of the existence of a neutrino mass are considerable.

Neutrinos are one of the most common and numerous particle of the universe; their total mass could provide a considerable fraction of the total mass of universe.

Since they not feel electromagnetic or strong force interactions their study is retained to be significant to provide clues to the origin of mass. In quantum mechanics neutrinos are well defined in their three flavors, however having they mass they could also feel the Higgs force that generates masses, and the neutrino emerging with well defined mass need not to be the same as those with well defined flavors.

Because of their extremely high probability of penetration through layers of matters without interaction, the neutrinos produced inside the Sun reach its surface and the Earth and reveal significant astrophysics informations on the processes taking place in the core of the Sun itself. This is not the case with light or electromagnetic radiation, carrying information only on the outer layers. Neutrinos play a crucial role for understanding the mechanisms that keep the Sun switched on.

At last there is the solar neutrino problem to be solved.

## 2.7 Why do we need an additional neutrino source?

To investigate neutrino oscillations, a neutrino beam that points towards one or two detectors at a distance of about one oscillation length is needed. Available neutrino sources provide a number of particles not big enough to investigate neutrino properties. Their intensity is not high enough to plan systematic investigation on the subject. With a tool as a neutrino factory, physicist can plan a much more systematic investigation of neutrino mass differences and



mixing. Neutrino factories will guarantee a constant  $\nu_e$  and  $\bar{\nu}_e$  beam as well as  $\nu_\mu$  and  $\bar{\nu}_\mu$  beam source with a narrow  $\nu$  and  $\bar{\nu}$  energy spectra.

Since the muon decay spectrum is very well known the systematic uncertainties on the flux and spectrum of neutrinos at distant experiments are expected to be significantly less than the corresponding uncertainties for a conventional beam. This would be expected to improve the ultimate precision of neutrino measurements. The neutrino beam that accomplishes this task must have peculiar qualities. No neutrino sources with these features are available among the sources quoted in section 2.3.

One more advantage is given by the fact that neutrino beam intensities achievable are sufficiently high that oscillation baselines of the order of the Earth's diameter are utilizable [20]. Such intensities and distances allow the study of neutrino-matter interaction.

### 2.7.1 Beam prerequisites

The neutrino machine needed to produce the suitable beam must provide the following properties to the beam:

- High intensity. As the cross section for interaction with matter is low this is the only<sup>1</sup> technically possible way to produce a sufficient number of events ( $10^{20}$  neutrino/year  $\rightarrow 10^{21}$  muons in the storage ring)
- High energy. The cross section of the neutrino detection increases with E that makes higher-energy neutrino easier to detect.
- Knowledge of the beam. There are two ways to observe an oscillation  $\nu_1 \rightarrow \nu_2$ . One is to observe the appearance of  $\nu_1$  and the other is to observe the disappearance of  $\nu_2$ . Since the oscillations are in the order of percentage, it is necessary to know the flux of  $\nu_1$  better than to observe disappearance.
- Pure beam. In order to obtain precise measurements of neutrino properties the beam for the neutrino factory must be very pure. Only muons of one charge should produce neutrino at one time. In case of a background of muons of the other sign it would be not possible to distinguish oscillated neutrinos from the background.
- Divergence. Neutrino beam divergence should be as small as possible so that neutrinos that hit the target are as much as possible.

---

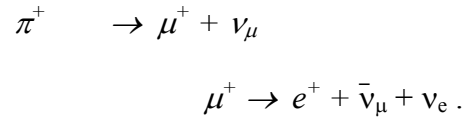
<sup>1</sup> Neutrino detection also depends on the detector's mass. High-mass detector technology is not yet available.

## 2.8 Neutrino Factory layout

To satisfy all beam requirement listed in section 2.7.1 a totally new complex of particle accelerator have to be developed: the neutrino factory [21].

The aim is to produce high-energy neutrinos in beams composed of only one neutrino flavor. As discussed in paragraph 2.3, neutrinos do not interact with matter because of they are subject to weak interaction; all features we want them to acquire must be provided before they are produced. This means that they must be the final product of a production chain and that required energy must be imparted to pre-decay particle.

The choice of the particle is determined by its production mechanism, its lifetime and the necessity of having two neutrino flavours. Moreover the mother particle must be easy to produce as the wanted number of neutrinos per year is  $10^{21}$ . The mechanism who satisfy these requirement is the pion decay:



The facility's layout reflects all needs of such decay. Neutrinos production path can be seen in Figure 2.2 where one can follow, from the decay-phases axis on the edge, the subsequent transformation from protons to neutrinos through the different components of the layout.

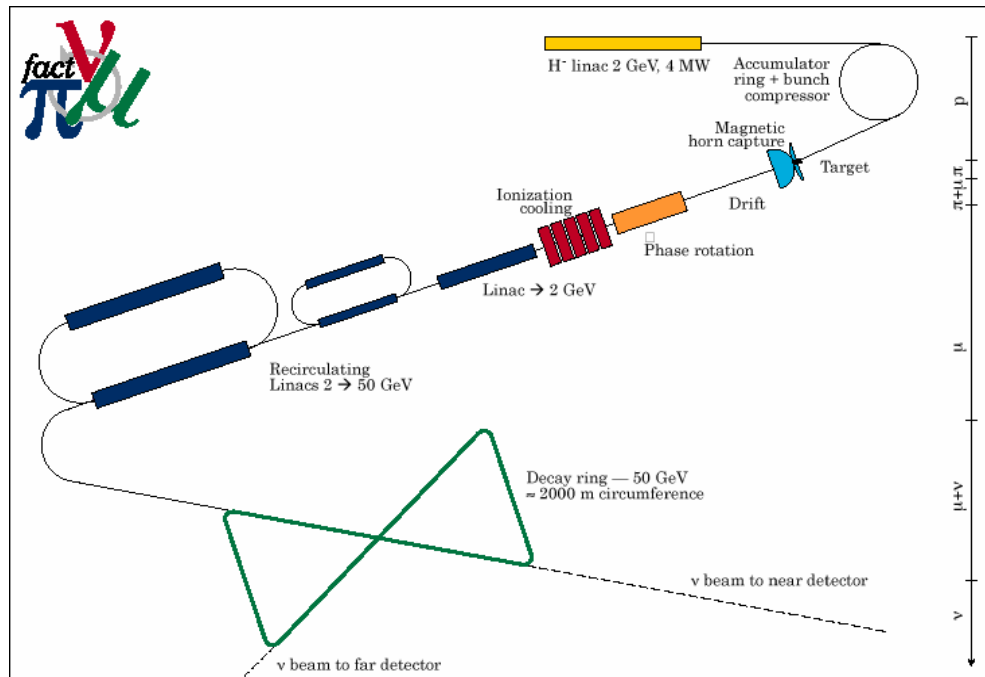


Fig. 2.2: CERN's neutrino factory possible layout [40]

### 2.8.1 Proton source

The possible layout of a neutrino factory starts with an ions source, as protons are the first ring of neutrinos' production chain. Ions needed are produced by ionization of a hydrogen atoms.

H<sup>+</sup> ions receive a first acceleration to an energy of 2.2 GeV from the linear accelerator SPL (Superconducting Proton Linac) and are successively delivered with a repetition rate of 50 Hz [22] to the second stage of the facility.

The output of the SPL cannot be directly used to produce pions. The reason is the low peak current. That is why the accelerated H<sup>+</sup> ions have to be collected over a 2.2 ms period in an accumulator ring.

The proton driver in order to provide an intensity of  $10^{21}$  neutrinos per year, should deliver a beam power of the order of 4MW. Beam power is calculated as the product:

$$P = E_p \times n_p \times f$$

In this possible layout of neutrino factory in order to achieve the desired number of neutrino per year, the machine parameters are:

- $E_p = 2.2$  [GeV]
- $n_p \cong 2.4 \times 10^{14}$  [protons/pulse]
- $f = 50$  [Hz]

which give an average beam power of 4 MW

### 2.8.2 Accumulator ring and bunch compressor

Accumulation is done by charge exchange injection [23]: the negatively charged 2.2 GeV ions are injected into the accumulator where they are deprived of protons.

At the end of the accumulation over, the structure has to be adapted to the downstream parts. This task is absolved by the 1 km circumference bunch compressor ring. In this component of the production line, which has the task of providing beam features, beam acquires the right pulse length that is given by the circumference of the ring [24]. Protons are ejected from the ring subdivided in 140 bunches of a 1 ns (r.m.s.) length in order to make the phase rotation possible. To match the 44 MHz bunch spacing must be 22.7 ns. These values provide a total pulse length of 3.3  $\mu$ s. A sketch of the complex SPL and accumulator ring and their possible location within CERN's area is illustrated in Figure 2.3.

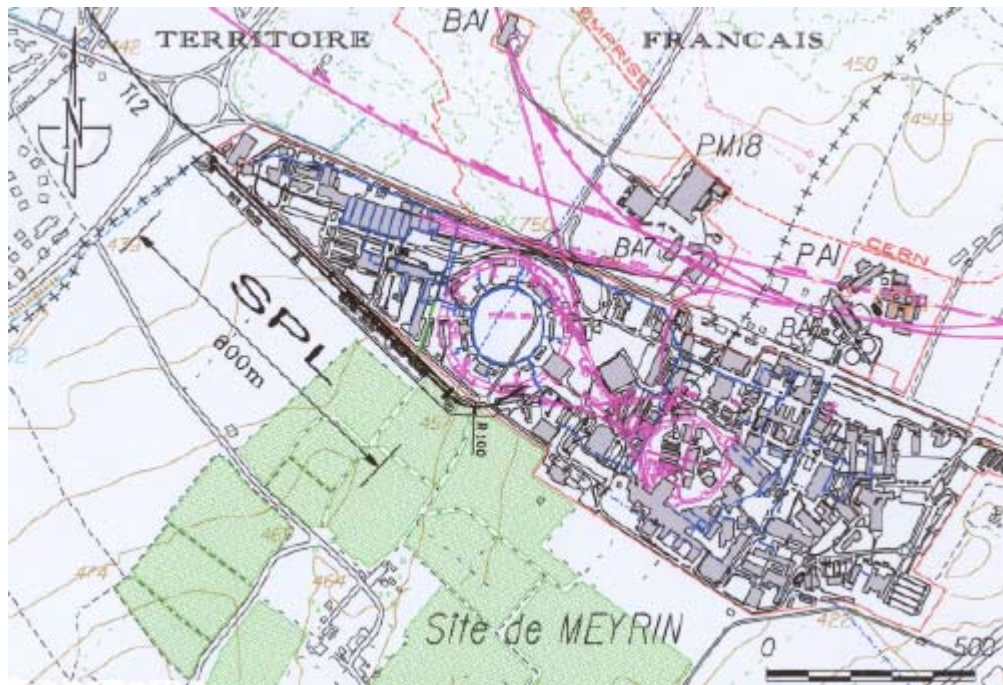


**Fig 2.3: SPL general layout, possible location. Accumulator, compressor ring and beam lines (violet)**

### 2.8.3 Target

A pion is produced when two nucleons collide. Protons produced are successively injected in the target area, where they collide with the target starting processes that lead to pions and subsequently muons production.

Considering that a high intensity proton beam is required in order to generate the required muons, the choice of the target material becomes a particularly important issue.

Proposals about target kind have been made and the favored solution at CERN of a liquid metal has been chosen. Other propositions about different kinds of target have been considered as, for example a stationary carbon target. Using a stationary target might avoid several critical issues linked to molten metal target, but this kind of target is only applicable to lower beam power with the obvious disadvantage of not achieving the expected number of neutrinos per year.

In CERN's proposed layout for a neutrino factory, a 4 MW and 2.2 GeV proton beam is proposed. Cause large pulse of energy (nearly 25% of the total beam power) deposited by this kind of beam in the target on microseconds time scale, the target is heated up by several hundred Kelvin after proton collision. The liquid metal is injected into the target area as a continuous jet. This moving jet target provides needed passive cooling. The thermal expansion due to beam/jet interaction causes disruption of the jet, which is destroyed at each beam pulse. The target has to be replaced at 50Hz, which gives a jet speed of 15 m/s considered a desired jet length of 30 cm. Such a length, which is the optimum target length, is the double of the

interaction length of mercury (see section 5.1). To allow some time to stabilize the jet, a speed of 25 m/s has been chosen.

Among different materials high- $Z$  materials are preferred cause their higher meson yield per incident proton. A justification for this is provided by plot of Figure 2.4 that depicts the pion production from a range of GeV protons on various target materials [25].

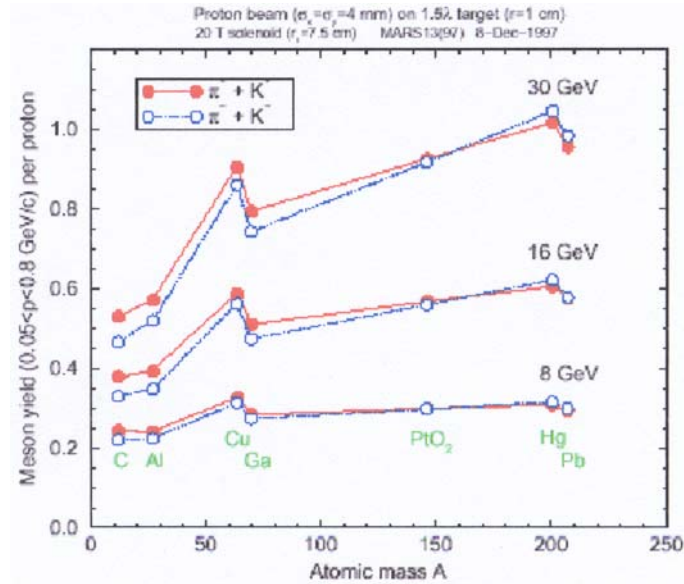


**Fig. 2.4:** Pion production from different GeV protons in high and low- $Z$  materials

The high density and the shorter nuclear interaction length of mercury make it possible to reduce the target to a small volume ( $l \approx 30$  cm). In case of lighter target lengths extend to meters as in the case of water ( $l \approx 1.8$  m). The higher  $Z$  material allows to reduce the target length, which results in a smaller time spread of the produced pions.

For incident proton beam energies greater than 10 GeV, as necessary for a neutrino factory, pion yield's curve has a maximum around an atomic mass of 200. A free mercury jet target, with its 200.59 atomic mass, appears to be the favorable candidate for the expected pion production. Currently the pion production cross section is only 25% [26]. To increase precision on the cross section and to help choose then right target material, the HARP<sup>2</sup> experiment has been started [27].

For a molten metal jet target the key parameter is radius, which is important in the pion yield that is affected by re-absorption in high- $Z$  materials. Optimum values may be extrapolated from plot of Figure 2.5 where the number of mesons per proton is plotted versus target radius.

<sup>2</sup> HARP: Hadron Production Experiment

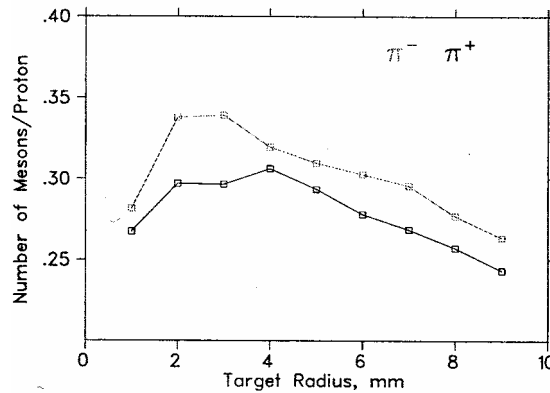


**Fig. 2.5: Influence of target radius on mesons yield [31]**

The radius of the target has to be chosen in accordance with the inner dimensions of the surrounding focusing system. The present baseline is an inner horn diameter of 2.5 cm. One more disadvantage of using solid targets are linked to transient pressure waves that are problematic for the long-term survival of solid targets.

#### 2.8.4 Transverse collection

The pions that are produced in the target have a wide angular distribution. To transport them they have to be focused. The average transverse momentum  $p_t$  of the pions has to be reduced or converted into longitudinal momentum  $p_z$ . This process is called transverse collection and is performed by applying a magnetic field to the produced pions [28]. There are two focusing devices that can perform this conversion: the magnetic horn and the tapered solenoid.

##### The magnetic horn

The favored solution at CERN is the magnetic horn. This component must provide the site for pions production. As pointed out above, a pulsed liquid metal target will be the target for an incoming proton beam. A 25 m/s and 1 cm radius mercury jet will be shoot inside the horn and hit with the proton beam delivered by the accumulator and compressor ring. Jet will be supplied by a pumped mercury line producing a continuous jet for a proton repetition rate greater than 25 Hz. Otherwise, below 25 Hz the jet could be pulsed, although the added complication of pulsing the jet and synchronizing the jet with the proton beam.

From jet-beam interaction pions will be produced. The pions decay into muons and total output is estimated to be 0.6 muons per incident proton.

As those particles will not follow a precise path, but will fly in all directions with approximately a  $90^\circ$  angle amplitude, they have to be collected to enhance the production of a high-quality muon beam. A 20 Tesla solenoidal field surrounding the beam can be exploited for this purpose and to focalize produced particles in a well-defined shape the beam that will be subsequently delivered to phase rotation stage. A 20 Tesla value is the field calculated to be the optimal for pions yields. According to Lorentz' law the produced pions are bended in the

direction of the horn axis. The field lines surround the beam so that on beam axis the magnetic field is equal to zero. In the magnetic horn solution no magnetohydrodynamic effects will affect the jet.

The horn (Figure 2.5) is an extremely critical item as it has to survive to a 4MW power beam even if a considerably fraction of this power is dissipated into the target. The field will be generated by a pulsed electric current of 300 kA to 400 kA intensity with a repetition rate of 50 Hz provided by the discharge of a capacitor bank into the horn. This current will produce a heat load in the horn's body. The horn will be so stressed by the superposition of differential thermal expansion and magnetic force.

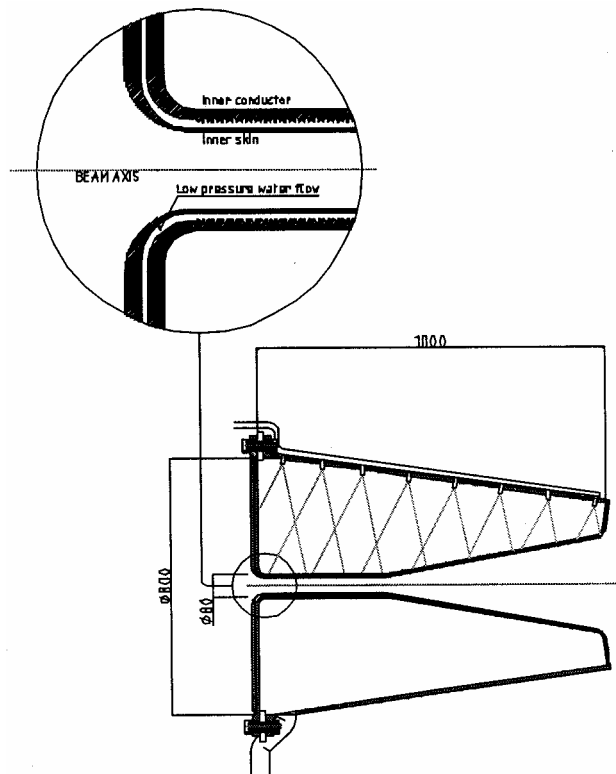


**Fig 2.5: Magnetic horn: main dimensions [mm], beam axis zoom and sketch of water spray cooling system [29]**

The thermal expansion has a steady state component and in addition an incremental temperature rise for each pulse. This incremental temperature rise is a result of Joule losses and energy deposited by the beam in the conductor. Fatigue is also involved in design problems as the resulting maximum Von Mises stress in the structure should not exceed the fatigue of Al alloy used and corresponding to the required life time of the horn [29].

Final design specifications are complicated by presence of an extremely high radioactive environment inside the horn that will produce a quick deterioration of internal surface.

### The tapered solenoid

The second solution of tapered solenoid is favored in the US scheme for a neutrino factory. The tapered solenoid exploit kinetic energy and total momentum conservation in a magnetic field.  $p_t$  is reduced by the action of a decreasing  $B_z$  and  $p_z$  is increased to keep  $p_{Tot}$  constant. Solenoidal field influence on produced beam behavior is shown in figure 2.4 below.

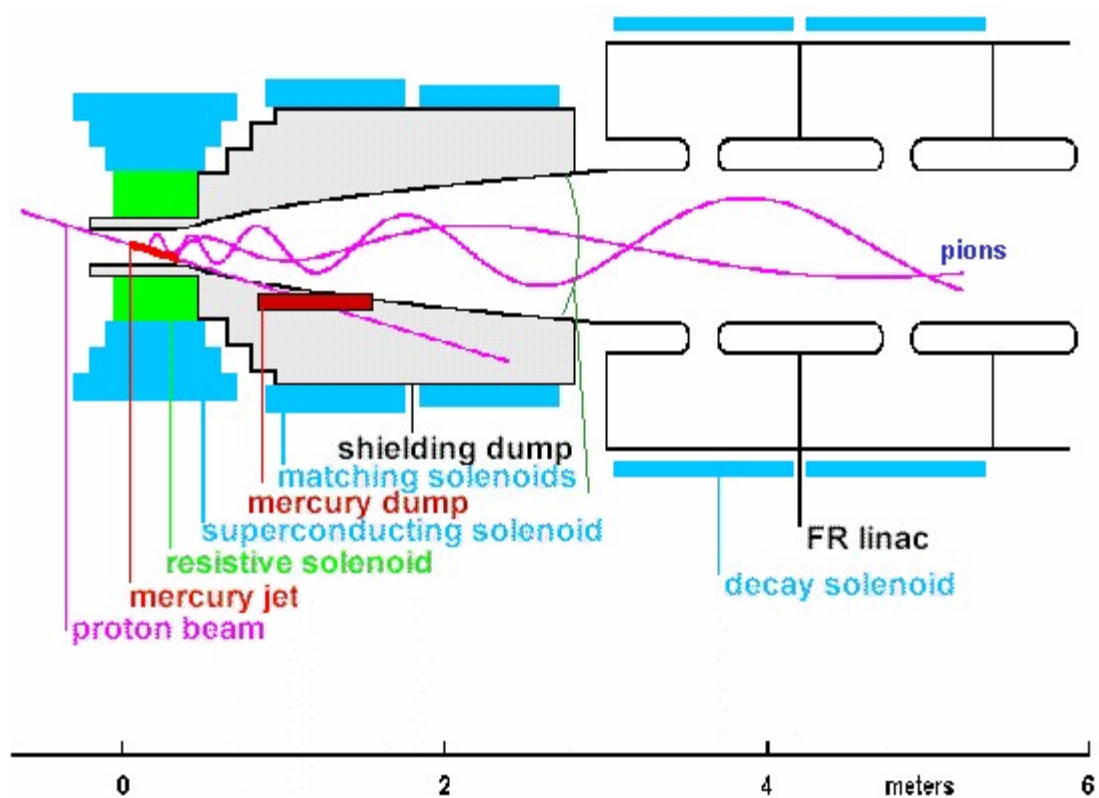


*Fig. 2.4: Tapered solenoid cross section: proton beam, liquid target and particle focalization*

The target should be placed at a small angle both with respect to the proton beam and the surrounding solenoid, in order to reduce pions re-absorption (Figure 2.4 above).

Contrarily to the magnetic horn, in the solenoid field lines will occupy the target region. This causes MHD effects that have to be studied (see chapter 4).

#### 2.8.5 Pion decay and phase rotation

The result of a transverse collection is a pion beam. The pion half-life  $\lambda$  is 26 ns which corresponds to a decay length of 7.8 m after 30 m, more than 95% of the pions are decayed into muons while more then the 95% of these muons ( $\lambda = 2.2 \mu s$ ), are still alive.



The decay of pions will take place in a solenoidal channel where muon beam characteristics will be imparted i.e. there is a correlation between position and energy of the resulting muons. Because of high energy repetition rate and the large number of bunches, an RF system working at 40-80 MHz is necessary to manipulate muons after pion decay and to reduce their energy spread. Moreover, the beam particles travels with different speeds and the beam would get longer and longer. To reduce this energy spread phase rotation has to be applied. Since particles with different energies travels with different speeds an energy-space correlation establishes. In a phase rotation section, rf cavities are set in a way that early arriving particles (which are faster) are braked and slower particles are accelerated. The result is a global reduction in energy spread. This means a reduction of the total momentum of the muons and re-establishing of the longitudinal momentum component with RF cavities.

### 2.8.6 Transverse cooling

The muon beam coming out of the phase rotation stage is nearly mono-energetic, so transporting it will not increase its length. This beam has a transverse emittance  $10^8$  times higher than the emittance of LEP beam [30] that makes it unconvinient to transport. Moreover this beam would not match the required low divergence of the final  $\nu$ -beam. A 188 m cooling channel is foreseen to reduce the transverse emittance.

### 2.8.7 Muon acceleration and decay

Further acceleration of the muons to 50 GeV is performed. Acceleration takes place in two recirculating linacs up to an energy of 50 GeV. Acceleration has to be fast because of the limited life time of muons, which is 2.2  $\mu$ s at rest.

To allow muons to decay in the right direction and so to produce neutrino beams in the desired direction, a muon storage ring with a bow-tie shape and long straight sections has been designed. This storage ring operates at 50 GeV and is extended also in vertical dimension to allow to point beam towards the detectors. One third of the produced muons will decay in the straight section [23]. From this component a total of  $\approx 3 \times 10^{20}$  neutrinos will be sent each year to two different distant detectors at approximately 1000 and 3000 km distance from CERN.

## **Part II**

### **The experiments**

## **Thesis overview and aims**

### **Towards a High Power Proton Target**

The high neutrino output demanded for a neutrino factory requests a high power proton beam interacting with a static target. The additional circumstances of limited space and long term stability ask for development of novel concepts for such types of targets.

In our working group, part of the Neutrino Factory Working Group (NFWG) of CERN, we are investigating on the proton interaction with the mercury target. This is called the study of proton induced shocks in molten metal. In the US scheme for a neutrino factory the interaction between proton beam and the mercury jet target takes place inside a 20 Tesla solenoidal magnetic field, which serves as a focusing device for the produced particles. This field of study is referred to as Magneto Hydrodynamics (MHD). The aim is to establish experiments to study this phenomenon and to quantify the impact on the overall design of the target area.

In the CERN scenario for a Neutrino Factory, the collision between the proton beam and the molten metal target should take place inside the 2 cm diameter internal duct of the pion production device (called magnetic horn).

The high power proton beam deposits a large amount of energy in the small volume of the target, which results in disruption. Considering the small dimensions of the duct, it could be obstructed by the splashing mercury preventing the subsequent jet to enter the target area. The first part of the study consists in measuring the splashing velocities of the mercury when hit by the proton beam and to derive, by scaling laws, the effects of the phenomenon under investigation for the foreseen final parameters. The study will give detailed information on the beam parameter influence on the splashing velocities. The investigation is carried out shooting a high intensity proton beam into a steady mercury target and subsequently observing the effects of the thermal shock induced by the energy deposition in the material.

This experiment is part of a global study over high power proton target, which includes also the experiment performed at BNL [9] in spring 2001 to achieve more detailed results and to use the different proton energy of 2.2 GeV. Experiments are requested in order to deliver bench marks for numerical simulations [34].

The second part of the work aimed to investigate magneto-hydro-dynamic effects occurring in the target area. Injecting the liquid metal target at a speed of more than 10 m/s into a 20 Tesla solenoidal magnetic field causes forces on the liquid. The repulsion and pinching of the liquid jet will be studied experimentally. Numerical simulations will be compared with these results [35].

By the superposition of results achieved from these two experiments the feasibility of using a liquid metal target for a neutrino factory will be derived.

The third part of the thesis work concerns the development of a technique for radioactive mercury handling and disposal. A final design of a neutrino factory will produce a certain amount of radioactive mercury, which might be destined for disposal/storage. After separation of radioactive mercury by distillation the radioactive

part could be stored. Storage could only be handled after solidification of it. The procedure chosen for solidification is to produce amalgam from the radioactive mercury. Small quantities for justification of the method are available from the experiment performed at ISOLDE. During the performed test a certain amount of mercury was activated and subsequently solidified following the developed technique. As the quantity of used mercury will be relevant, the procedure developed will become the starting point of a production of industrial scale.

## Chapter 3

### Proton Induced Thermal Shocks in Molten Metal

#### 3.1 The ISOLDE facility

The experiment on proton induced shocks requires a proton beam to be shot to the mercury target. A proper facility for this purpose is ISOLDE at CERN.

ISOLDE is an acronym indicating Isotope Separator On Line DEvice. The facility is dedicated to the production of a large variety of radioactive ion beams for a great number of different experiments, for example in the field of nuclear and atomic physics, solid-state physics, life sciences and material science.

At ISOLDE, radioactive nuclides are produced in thick high-temperature targets via spallation, fission or fragmentation reactions. The targets are placed in the external proton beam of the PS booster, which has an energy of 1 or 1.4 GeV and an average beam current of about 2  $\mu\text{A}$ . An electric field accelerates the ions, which are mass separated and steered to the experiments.

The proton injector for ISOLDE, the PS Booster (PSB), is a stack of four small synchrotrons pre-accelerating protons, delivered by a Linac, to 1 GeV before injection into the CERN Proton Synchrotron (PS). PS in turn supplies particles to all CERN's high-energy machines. The PSB gives one pulse of  $3.2 \times 10^{13}$  protons every 1.2 seconds. Up to half of the pulses in the 12 pulses long super cycle to the PS is brought to bombard the ISOLDE target. The protons from the PSB are delivered to the ISOLDE target zones via an underground transfer line, which serves two different isotope separators, one with its target position situated in a straight extension of the beam line and a second one after a bend of 400 mrad.

ISOLDE area is composed of two different sections, one including targets and the second including experimental area and control room. The main experimental area is completely separated from the radioactive handling area, to which access is through a special entrance. Two industrial robots, similar to those used in the automobile industry do the handling of the targets. The whole region around the target is shielded with steel and concrete blocks and has been buried under 8 m of earth.

ISOLDE uses two different separators, first is called the General Purpose Separator (GPS). It is designed to allow three different beams within a certain mass range to be selected and delivered simultaneously into the experimental hall via three different beam lines (central mass, low mass and high mass beam line). This is the separator, or rather its component called front end, have been used during our experiments. The second separator is specially constructed as a High Resolution Separator (HRS) and can only deliver one mass at a time to

the experimental hall. The two separators' positions within ISOLDE layout is shown in fig. 3.1.

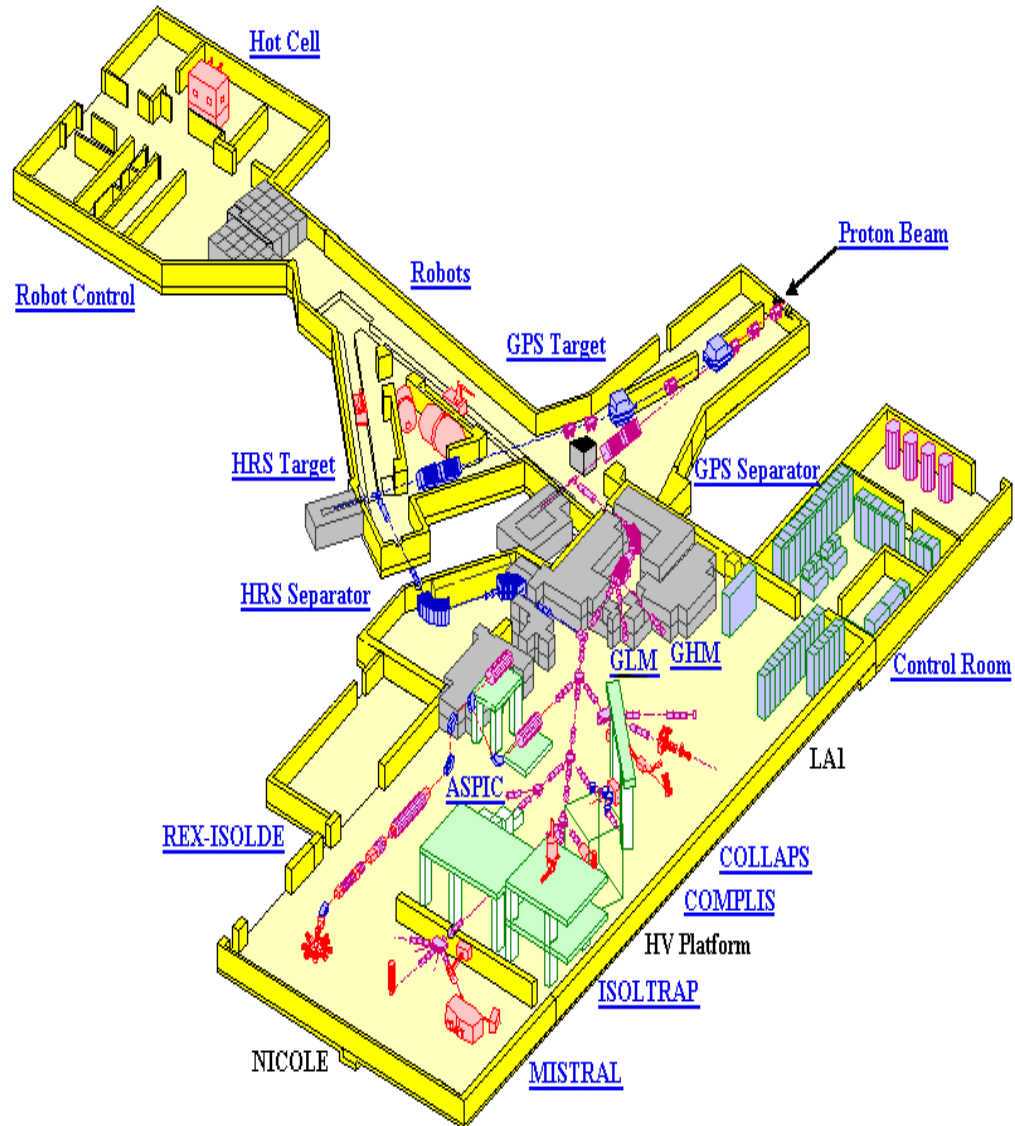


*Fig. 3.1: ISOLDE facility layout*

This facility constitutes the ideal tool for the experiment that had to be carried out using a proton beam even if the remarkable mass separators of the installation had not been exploited. Our target in fact, was laying on the front end rest (see fig. 3.2) and was installed in a different way from conventional ISOLDE's targets that are under vacuum and electrically connected with the front end since they need to be heated up to high temperatures during experiments.



*Fig. 3.2: GPS front end with conventional target installed*

## 3.2 Experimental Set Up

The purpose of the experiment is to shoot a proton beam into a small quantity of mercury in steady conditions. Mercury is contained in a “thimble” or in a through drilled into a stainless steel frame. The observation of the experiment was done by optical read-out. A sketch of the basic concept of the experiment is shown in the Figure 3.3 below:

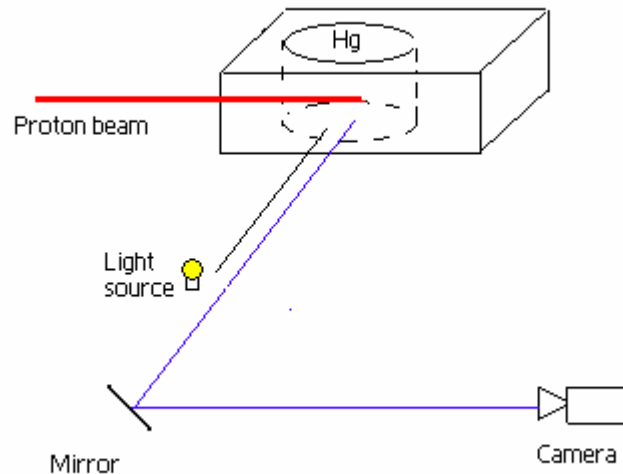


***Fig. 3.3: Sketch of thimble test principle. The incoming proton beam hits mercury and the event is recorded by a high-speed camera. Image lightening is guaranteed by a light source put in front of the target.***

The experimental set up comprehends ISOLDE facility and its front end, the target, a high-speed camera, a triggering system, a recording system and an illumination system. All these components, forming the measurement chain, must be connected together in order to make event analysis possible.

### 3.2.1 The target

The target has been studied to resist a 1.4 GeV proton beam impact and to be made of materials fully compatible with mercury. It is fundamentally a container in which mercury is hermetically closed in order to avoid environment contamination. Since we are interested in filming what happens to mercury while hit by the proton beam, it is included the possibility of looking at what happens inside the target. Target is mainly composed of three parts assembled together: the steel frame and a viewing window on either side of it.

A stainless steel plate with a squared window opening constitutes the target body (see fig. 3.4). The bottom part of the frame is declined, to facilitate mercury's recover after its splash, and of a flat part. In the flat zone a hole constituted of a half sphere of 6mm radius surmounted by a cylinder of the same diameter and of 6 mm height has been drilled. Considered the thimble shape of this the whole experiment has been called "thimble test" in order to distinguish it from the second target with a through-shape hole that was designed for further tests.

The central frame includes connections for proton beam windows, a pumping line for the mercury vapor filter and a short pipe connected to a tap valve used for introducing mercury and to fill the experimental chamber with argon.



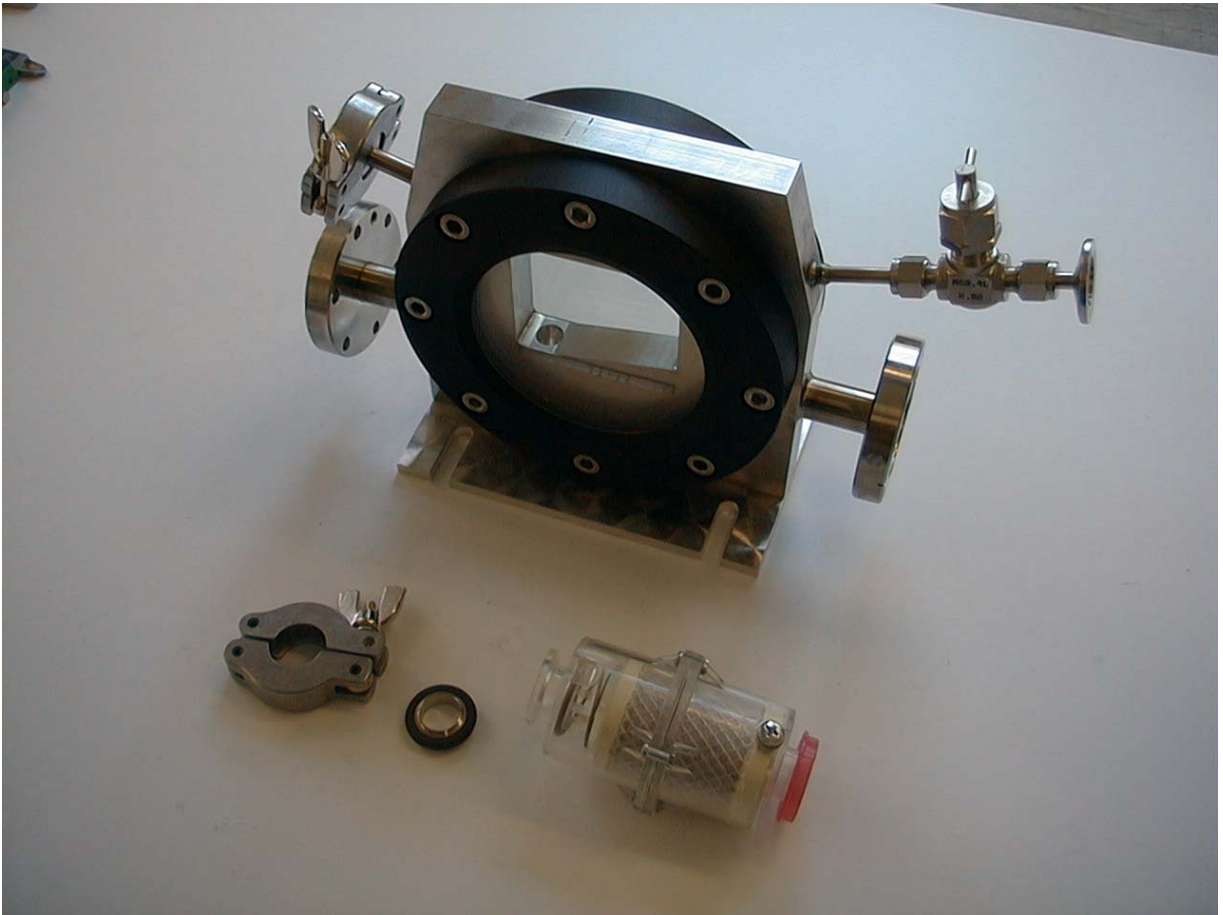


*Fig. 3.4: Target lateral view (up), vapor filter (low right)*

On both sides of the stainless steel frame two port-hole shape windows have been screwed. The windows are equipped with o-rings (rubber) that guarantees seal among windows and frame. For verifying this feature a test has been performed. It consisted in creating vacuum inside the experimental chamber by connecting to the tap valve a vacuum pump. On filter connection, a manometer was mounted to continuously monitor pressure values. Under-pressure value achieved of  $-700$  mmHg was maintained almost constant for two days and demonstrated a sufficient seal level.

On either side of the steel frame viewing windows with a two layer system are mounted to allow optical observation. The internal layer, in contact with mercury, is Quartz made while the second and the external is LEXAN as a second confinement. LEXAN has very good properties under mechanical stress caused by thermal dilatation induced by the incoming proton beam.



*Fig. 3.5: Window's components: port-hole with screws, quartz, Plexiglas and o-rings*

Components, superposed starting with the o-ring passing through the Quartz glass, the flat rubber o-ring and the LEXAN layer are covered with the stainless steel port-hole which is screwed to the central frame. All components are show in Figure 3.5 and assembled in Figure 3.6.

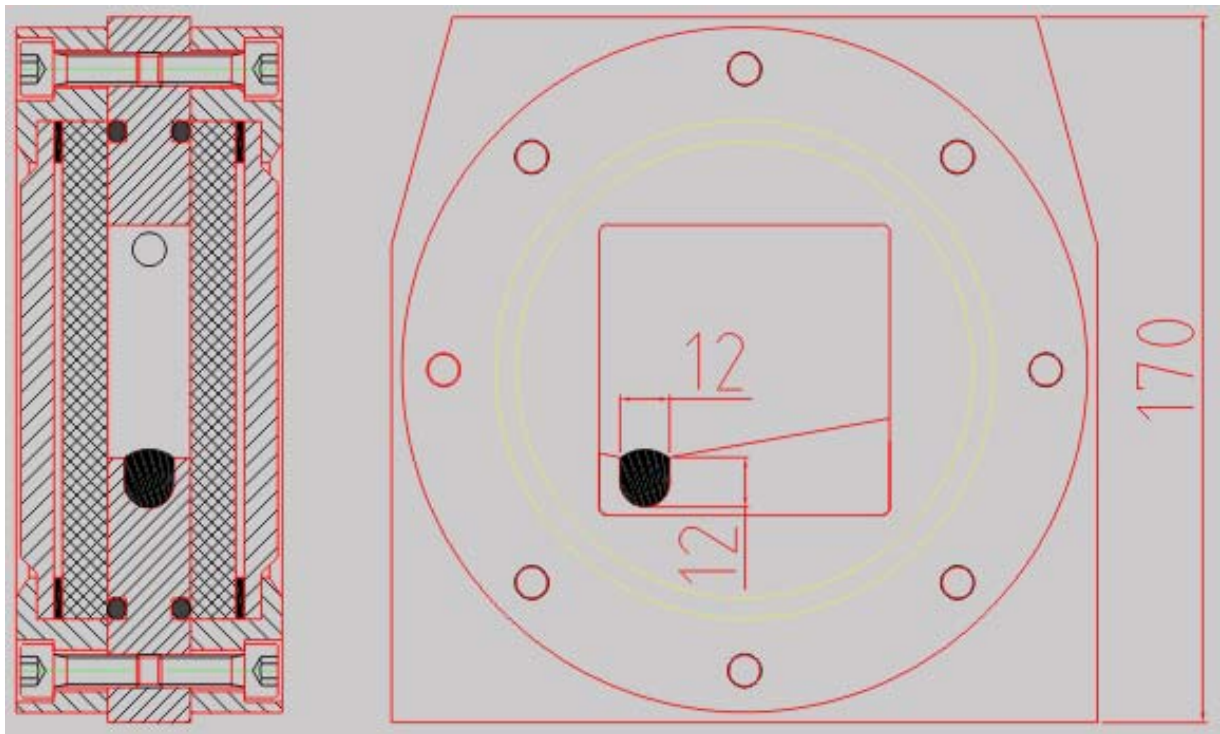


*Fig. 3.6: Target side view/cut with mounted windows*

### 3.2.2 High-speed camera system.

Since events' time length is in the order of magnitude of milliseconds, a special high-speed motion analysis system is required. The camera system used is an industrial product, OLYMPUS Encore PCI High Speed Video System 8000S.

This system consists of a CCD camera head and a PC providing special software required for recording and image manipulation. The camera head accepts any c-mount lenses. The PC runs the OLYMPUS MAC PCI version 2.21.1 program that allows image analysis of distances and speeds.

The digital imaging system records an event at a frame rate of 50 to 8000 frames per second (fps). The system stores these images in an image memory on the controller unit. These images can be viewed forward or reverse at selected frames rates from 1 to 8000 fps, frame-by-frame or freeze frame, to analyze motion and time during the event. All events had to be stored on disk in order to successively analyze them offline.

The exposure of each frame, also named as shutter time, is reduced at higher frame rates. So more illumination is required as the frame rate increases. For this purpose an electronic shutter control is included in the program and sets exposure time in order to eliminate image blurring due to motion. The shutter time can be remotely set from  $1/\text{frame rate}$  (seconds) to a minimum time of one  $20^{\text{th}}$  of it.

The camera head imager must receive enough light to see details of the image, and record the subject at the optimum size so that the significant part of the motion can be seen clearly. The camera has an infrared filter to give subjects the correct gray scale appearance.

The camera head has a CCD imager sensor with an image area of 680 x 500 pixels, each pixel being  $7.4 \mu\text{m}^2$ . The maximum number of pixels is only used at record rates up to 250 fps, where at 4000 fps the image size is reduced to 100 x 98 pixel. Figure 3.7 gives the responsivity and sensitivity of the monochrome CCD imager across the range of visible light.

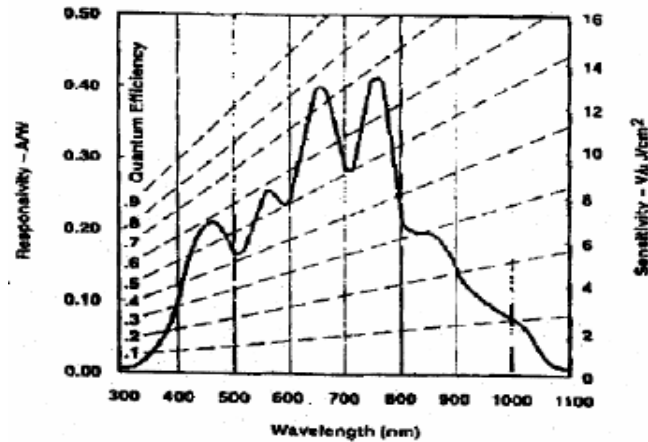


*Fig. 3.7: Spectral characteristic of CCD sensor*

For recording events of proton beam test a record rate of 4000 fps has been chosen. This value gave the possibility of recording up to 8000 images in 2 sec time with a time spacing of 0.25 ms between each image.

Expected mercury's vertical splash velocities are in the order of up to 20 m/s. With the given record rate a droplet with this speed moves over a distance of 5 mm between two frames, which is a value that permits a precise analysis of motion, as the viewed area of mercury splashes is about ten times bigger.

Image resolution at record rate of 4000 fps is 100 x 98 pixels. From this value strictly depends the precision of the measurement. From calibration of the images one calculates a spatial resolution of 0.89 mm/pixel, which is the dominating error in the analysis.

For further details see appendix 1.1: camera's performance specifications.

### 3.2.3 Trigger

A trig-in lead is necessary to synchronize incoming proton beam and image recording. The control board of ISOLDE control room provides trigger signal. The PC detects the incoming signal and allows measurement to begin. The total record time is fixed at high-speed recording (> 500 fps) to approximately two seconds.

Considered the high speed of events to be recorded, particular attention had to be paid to delay between trigger signal, that starts image recording, and image acquisition. This precaution permitted to avoid risk of losing information related to first images.

The aim to achieve with the calibration was to find out the delay between the trigger signal and the first frame impressed with an image. Two attempts (see Table 3.1 and 3.2) have been done changing the record rate and the shutter time. Each attempt consists of ten measurements to provide a sufficient precision at the calibration.

The experiment set up includes an oscilloscope, a pulse generator to provide trigger signal, the high-speed camera and its PC and three LED.

The three LED have been welded together on a coaxial cable and connected to the pulse generator outlet for light them. The so assembled cable was put directly in front of the camera CCD sensor without objective. Once the trigger signal started the camera the illuminated LED were filmed. Since trigger signal had a fixed length of 135.9 ms and was visualized on taken frames, it has been possible to count images from mentioned signal and the first image recorded by the camera's CCD.

### 1<sup>st</sup> attempt

Record rate: 4000 frames/sec  
Shutter : 1/40000 sec

*Tab. 3.1: First measurement values*

Attempts	Trigger length [ms]	Frame lost	Delay [ms]	Last useful frame
1	135.9	5	0.5	921
2	135.9	5	0.5	918
3	135.9	5	0.5	917
4	135.9	5	0.5	916
5	135.9	5	0.5	918
6	135.9	5	0.5	918
7	135.9	6	0.63	918
8	135.9	3	0.38	915
9	135.9	5	0.5	917
10	135.9	5	0.5	917

### 2<sup>nd</sup> attempt

Record rate: 8000 frames/sec  
Shutter: 1/24000 sec

*Tab. 3.2: Second measurement values*

attempts	trigger length [ms]	frame lost	delay [ms]	last useful frame
1	136.3	5	0.5	932
2	136.3	5	0.5	933
3	137	5	0.5	933
4	137.1	5	0.5	932
5	137.2	6	0.63	933
6	137.3	5	0.5	934
7	137.3	6	0.63	935
8	137.4	5	0.5	933
9	137.4	5	0.5	933
10	137.4	6	0.63	934

Warnings:

- Number 0 frame is considered the first frame
- Delay time corresponds to the last frame lost (1<sup>st</sup> frame considered good when a change in brightness is seen)
- Frame lost = frames without images including frame # 0
- Last useful frame = number read from PC's display

For a trigger signal corresponding the record rate of 125  $\mu\text{s}$ , only one frame is illuminated. When the trigger signal correspond to the sum of record rate time and shutter time two frames are illuminated ( $125 \mu\text{s} + 1/24000 \mu\text{s} = 1.6 \mu\text{s}$ ).

This showed, that the camera internal frame zero is shifted towards the external trigger by a constant number of frames. This offset is at least as constant as the maximum shutter time. This trigger specifications are sufficient for the used time scale.

### 3.2.4 Light source

High intensity light sources are basically used in every high-speed applications, where high recording rates up to 8000 fps are needed.

The Olympus ILK-6 light source used for illuminating the target is equipped with a 150 watt quartz halogen lamp. Light output is controlled mechanically by opening or closing a shutter. The light is transported via a liquid light guide to an optical system, which produced a parallel light beam. In order to avoid interference between the equipment composing the light source and the camera's field of view, light was reflected by a mirror a system mounted on the target rest as shown by fig.3.8. The camera recorded at a distance of approx. 15 m distance from the target to save it from radiation damage.

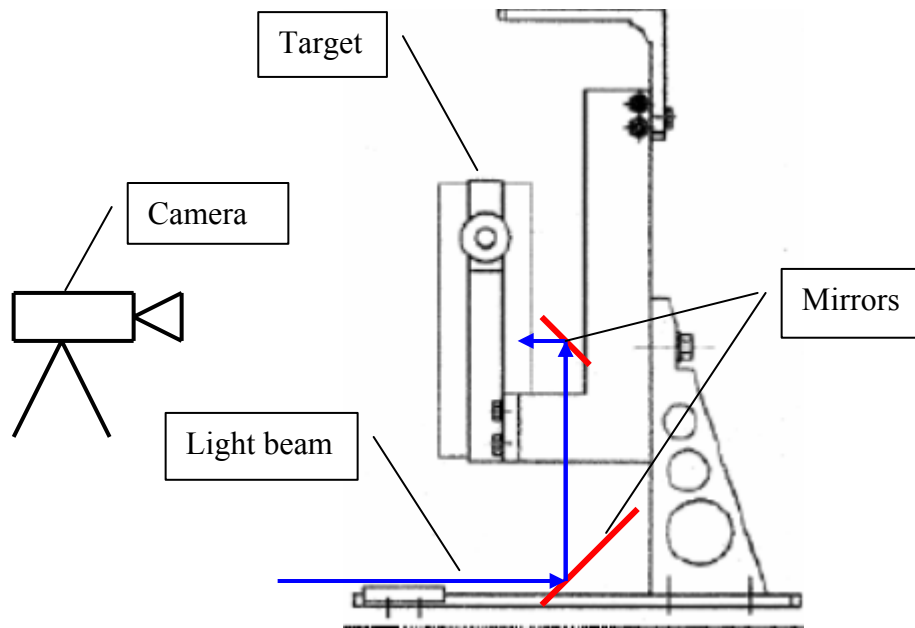


*Fig. 3.8: Mirrors' positioning scheme*

### 3.3 Set up in ISOLDE target area

In ISOLDE target area. Target has been substituted to the front end conventional target. The camera and its computer were hidden behind the partition-wall between GPS and HRS for avoiding their exposure to radiation. Since from this position target was not visible, a mirror put in front of the target at a distance of approximately 13 m, reflected the target image as shown in fig.3.9. It was so possible to capture images avoiding equipment's contamination.

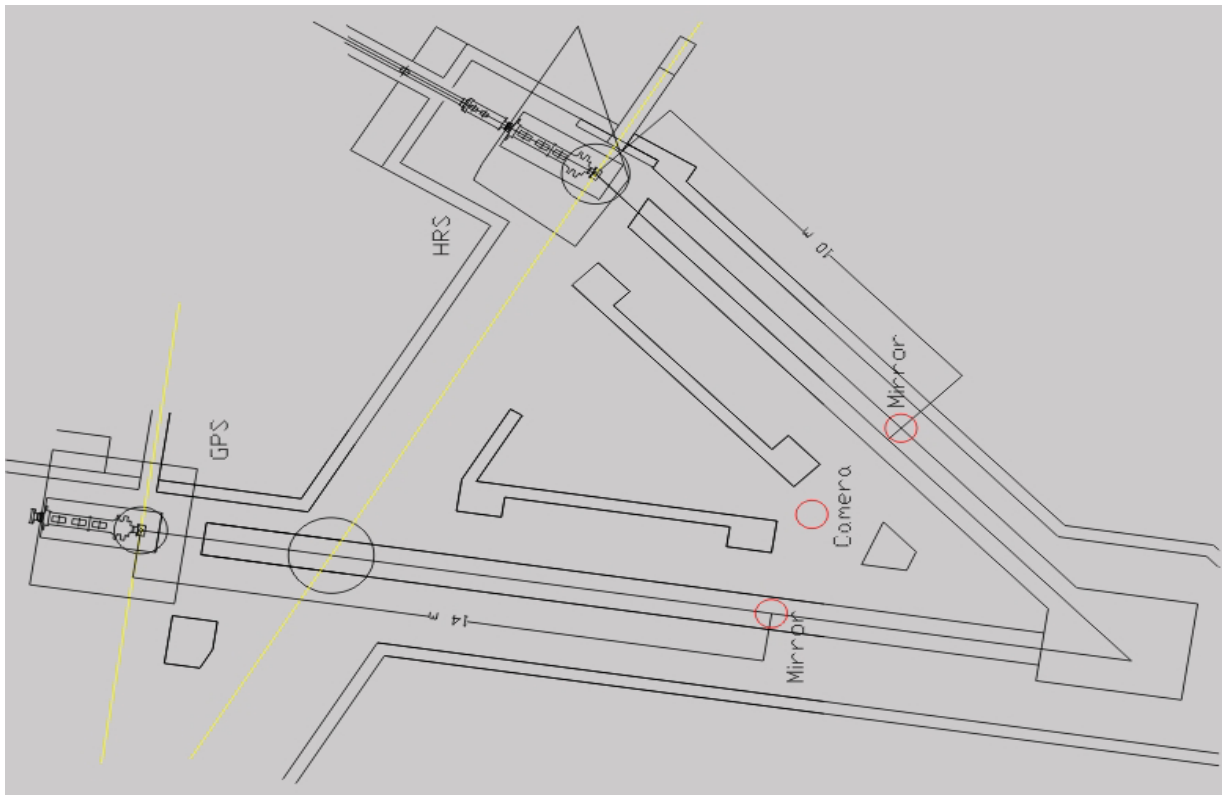


*Fig. 3.9: Camera's and mirror's positioning during the experiment. The figure also indicates the mirror position in the use of the HRS (never performed).*

### 3.4 Beam parameters

Test aims to show different behaviors of mercury when hit by proton beams with different features. During the experiment, kinetic proton energy was fixed at 1.4 GeV for all events. A proton beam is composed by a number of protons of the order of  $10^{12}/10^{13}$ . Protons may not be shot all contemporarily but may be divided in groups. The allotment of proton gives beam features.

The groups, called bunch, are composed of some Tera protons<sup>1</sup> [Tp] each. This number constitutes the bunch intensity measured in proton per bunch [ppb]. Bunch intensities multiplied by the number of bunches (1-4) gives the total pulse intensity measured in proton per pulse [ppp]. One more pulse feature is time distance between bunches called bunch spacing. This value is usually in the order of nanoseconds as well as the bunch length (230 ns, not variable). Since a pulse is composed of bunches its duration is given by number of bunch multiplied by bunch spacing and number of bunch multiplied bunch length summed together. The total pulse length is in the order of  $\mu\text{s}$ .

<sup>1</sup> 1Tp  $\rightarrow$   $10^{12}$  protons



The spot size of the bunch can be varied, this means changing the cross section area of the bunch and so the density distribution in the target. As the transverse distribution is always Gaussian, talking about spot size means in fact  $1\sigma$  radius.

The last feature that was previewed variable is the vertical position of the beam in relation to mercury center position.

The experiment comprehended 39 shots carried out with a time distance of approximately 20 minutes in between to allow target's cooling by natural convection since no active cooling system was installed.

The experiment was carried out dividing it in 8 different sets of parameters as shown by tab.3.3 below.

**Tab. 3.3: Pulse set composition**

<b>Set</b>	<b>Variation</b>		<b>Fixed</b>
1	ppp	2,6,8,10	Spot (2.2), bunch (1)
2	ppp	2,6,8,10	Spot (2.8), bunch (1)
3	ppp	2,6,10	Spot (3.5), bunch (1)
4	bpp	1,2,3,4	Spot (2), ppp (8), spacing (min)
5	bpp	1,2,3,4	Spot (2), ppp (8), spacing (1000)
6	spacing	350,1000,2000	Spot (2), bunch (3)
7	maximum		Spot (2), bunch (4)
8	ppp	1,2,4,6,8	Spot (3.5), bunch (4)

To each set corresponds a variation in some of the parameters as shown in test's logbook in appendix 1.2.

First set of four pulses consists of four shots of one 2.2 mm spot size bunch containing an increasing number of protons. Series comprehends shot containing 2-6-8 and 10 Tp each. The second set of shots maintained the same number of pulses and of protons per pulse (ppp), but spot size was increased up to 2.8 mm. The third set shot one bunch pulses of 2-6-10 Tp with an increased spot size up to the maximum value of 3.5 mm.

Concerning the fourth set protons per pulse value was maintained constant at 8 Tp while number of bunches was varied. Bunch spacing was set to minimum value of 286 ns and proton divided in 1-2-3 and 4 bunches of 2.2 mm spot size. In the fifth set the parameter set up was maintained identical but time spacing that was increased to 858 ns.

The sixth set of shot with beam features of 3 bunches of 10.5 Tp each with 2.2 mm spot size. Bunch spacing values are  $j \times (5, 7, 13, 19, 27)$  ns. The seventh set of values aimed to observe the influence of a vertical beam scan in rapport to mercury's position. Beam was displaced up to 6 mm above the standard zero position and up to 11 mm under the same position. Beam feature are the same of precedent set with a bunch spacing of 1430 ns.

The eighth and last set performed shots with high spot size and high beam intensity up to 27 Tp allotted in four bunches.

### 3.5 Extracting Initial Explosion Velocities

Once the proton beam hits the mercury pool, the liquid exits the pool in vertical direction. The phenomenon is due to beam energy deposition, which causes heating of the target and thermal expansion leads to an explosion. The aim of measurements is to determine the splash behavior as a function of proton beam characteristics.

The fundamental quantity of the splashes is the initial velocity of the mercury splash. This value will be determined as function of different beam parameters. With this one can extrapolate to the full-scale target for the designed neutrino factory.

From the recorded movies the mercury position was extracted. Image analysis has been carried out using the OLYMPUS software supplied with the camera. The software includes an image analysis system based on a Cartesian coordinate system. By calibrating the image with a known distance it is possible to successively take distances and speed measurements. For this purpose a thin plastic foil with a grid drawn on it has been inserted in between the stainless steel frame and the quartz glass. This grid has a net width of 1 cm in both horizontal and vertical direction (see fig.3.10).

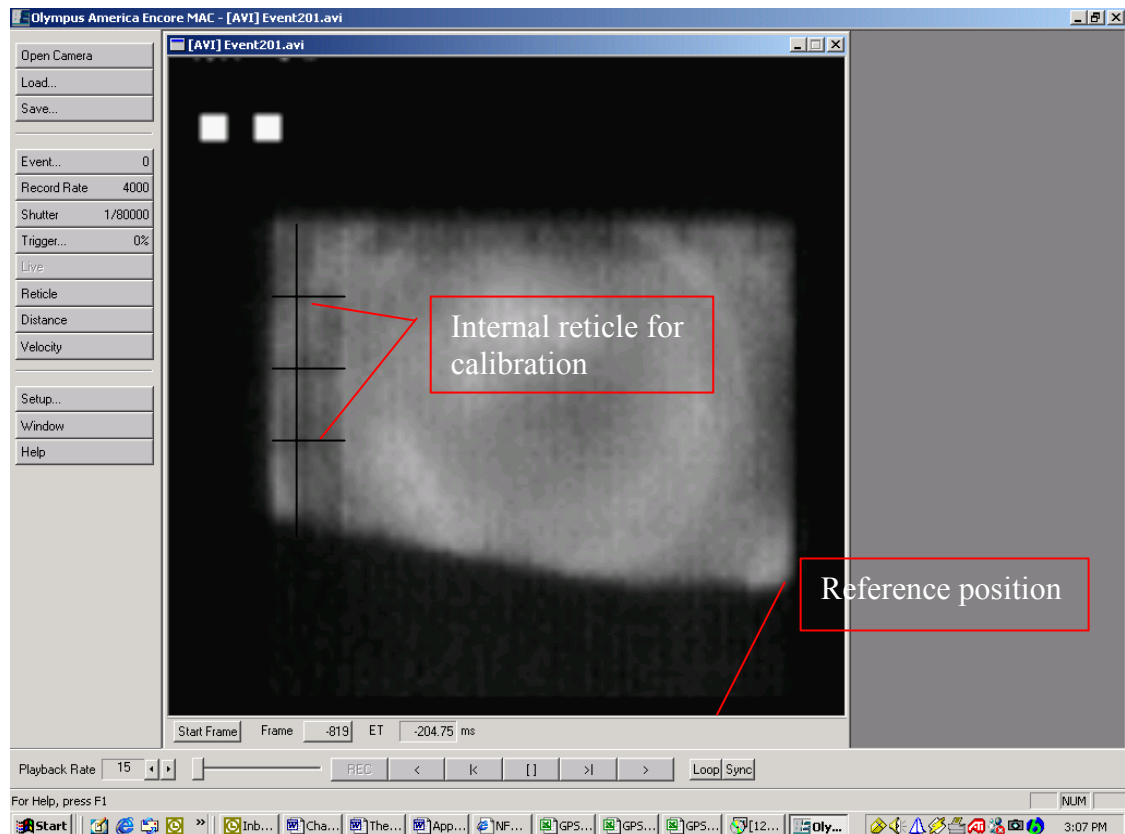


*Fig. 3.10: References points*

Image bottom part has been chosen as vertical reference position for the mercury movement and thimble vertical axis as horizontal reference; all distances successively measured are referred to this position (see Fig. 3.10).

The time  $t = 0$  was recognizable cause white dots appearing when the beam hit the target. These dots are due to formation of nuclear sub-products of steel/proton interaction. Generally in the third following frame ( $t = 375 \mu\text{s}$ ), the first movement of mercury was visible.

Extracted information from the movies values are: white dots first appearance, mercury's meniscus starting position before its movement, first frame with visible mercury's movement, and successively jet positions at frame number 1, 2, 3, 4, 6, 8, 12, 16, 20, 24, 28, 32 and 36. In particular case since jet speed was too high, last two measurements were not taken having the jet already reached the top part of the chamber.

For complete measurement values see appendix 1.3.

From pictures below (Figure 3.11), drew out of films taken of set one, one can see the influence of number of protons contained in one bunch on jet's reached height and velocity.

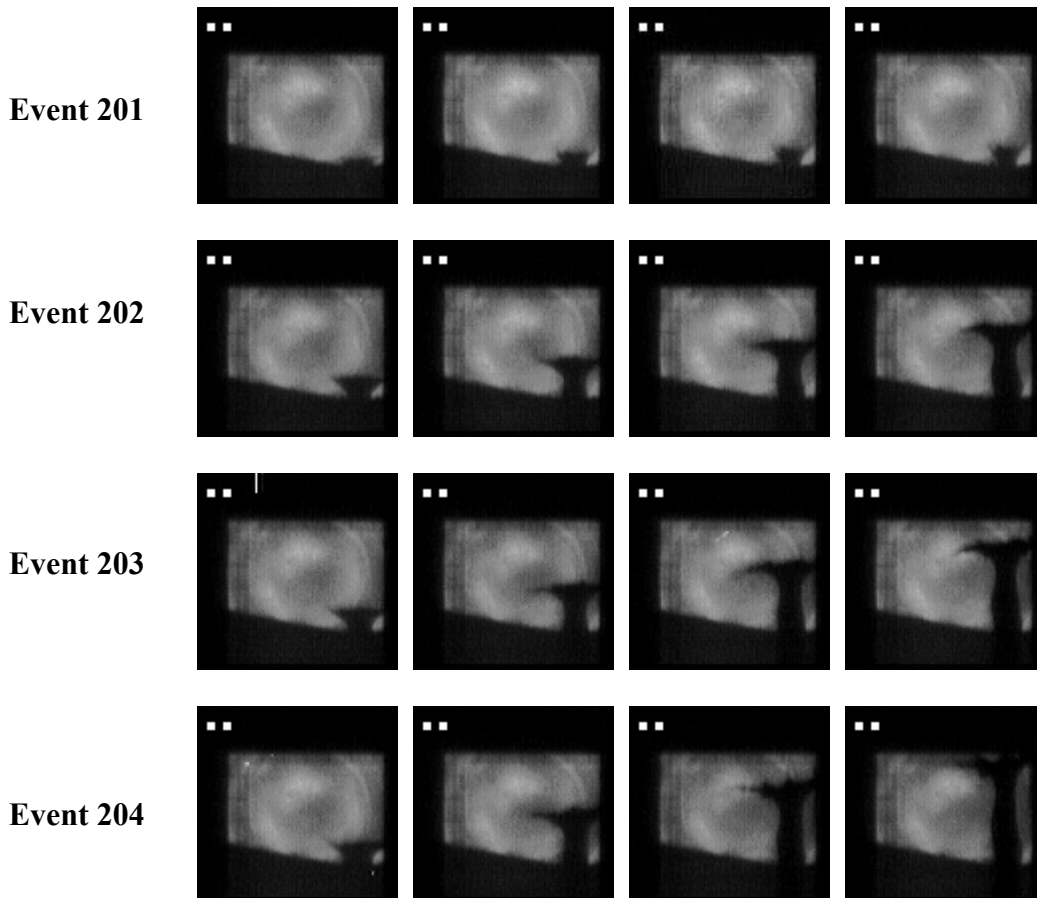


**Fig 3.11: Events of set 1: splashes' height rise with number of ppb.  
Event 201: low intensity, Event 204: high intensity.**

Increasing intensity of the bunch, mercury bulk achieves a higher velocity. This is demonstrated by the fact that mercury position recorded at same time in different events, increases by increasing ppb.

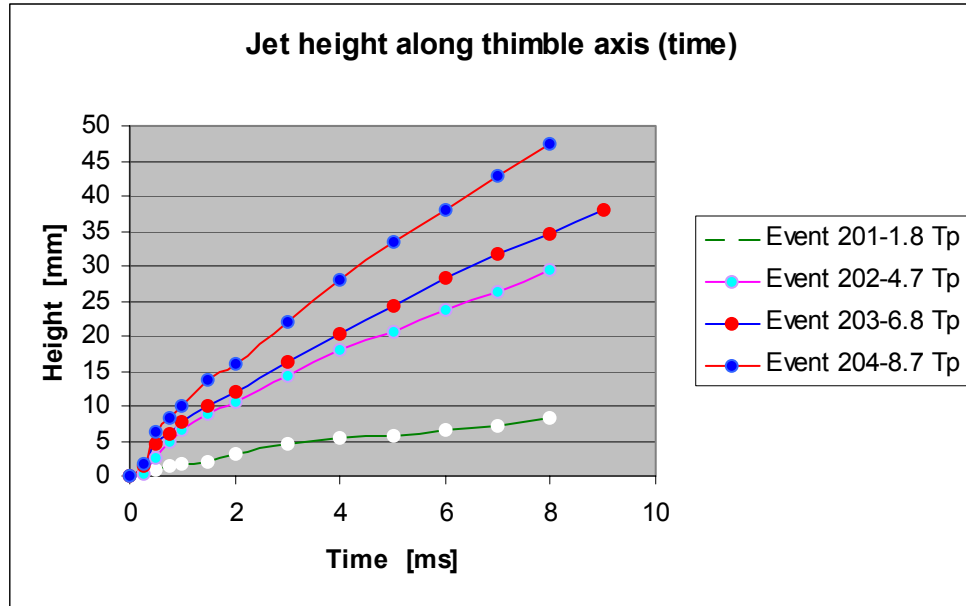


*Fig. 3.12: Jet height along its vertical axis as function of ppb. ppb values of 2-6-8-10 Tp*

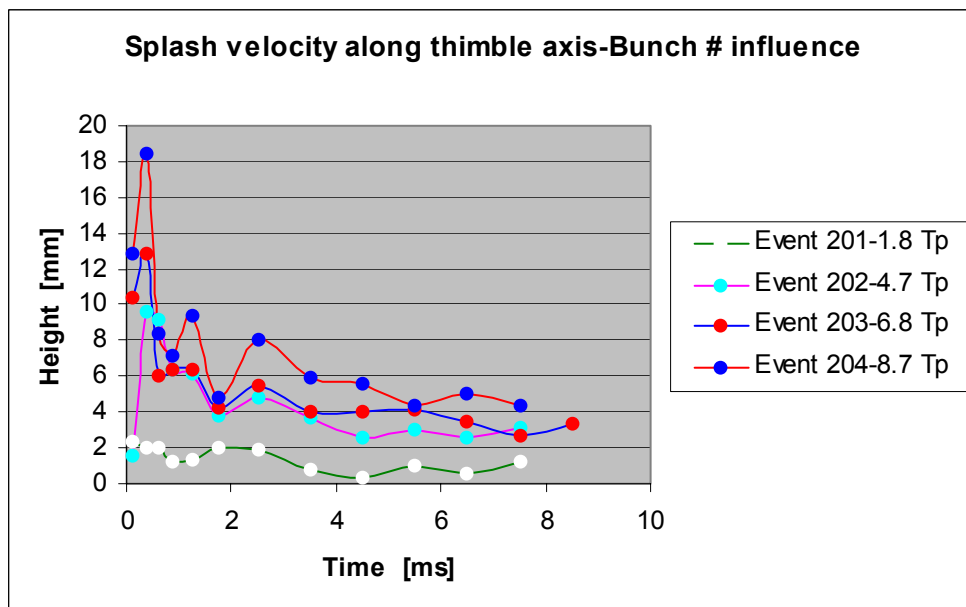


*Fig. 3.13: Jet velocity along its vertical axis as function of ppb. Ppb values of 2-6-8-10 Tp*

The comparison between events of set number one is plotted in Figures 3.12 and 3.13 where speed and heights achieved by mercury bulk are compared.

Main difference in jet behavior is between event 201 and 204. In event 201, mercury seems not to react to beam impact and achieved height is in the order of 10 mm over starting point while in event 204 jet reach the top of the experimental chamber which is at 50 mm over mercury's meniscus starting position. Concerning jet's starting velocities, they range from 2.4 m/s in event 201 to 12.8 m/s in event 204.

Spot size influence on jet behavior may be pointed out from comparison (see fig. 3.14) of events of first, second and third set. Each pulse contained the same amount of protons i.e.  $10^{13}$ . The corresponding spot sizes are 2.2 mm (Event 204), 2.8 mm (Event 208) and 3.5 mm (Event 211).

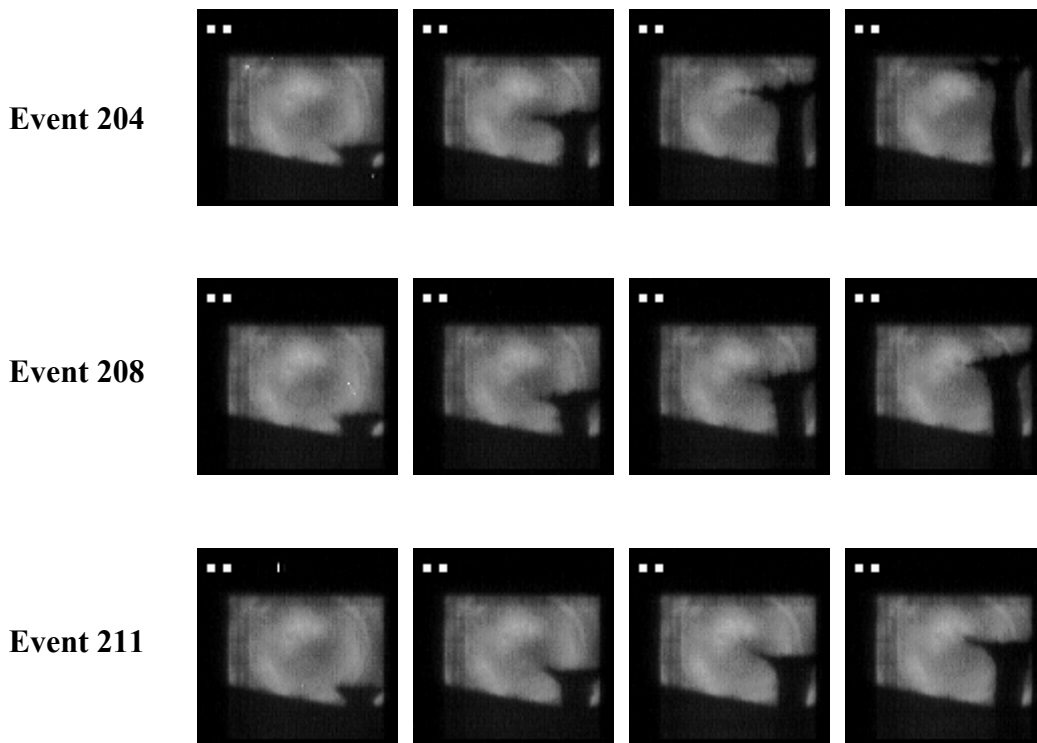


*Fig. 3.14: Events 204, 208 and 211: influence of spot size on jet's height*

One observes that the height reached by the jet bulk is decreasing passing from event 204 to 208 and 211 as a function of spot size, so inverse to the spot size. The height as a function of time reached by the jet is shown in fig. 3.15 where heights reached by the three jets are compared. Values range from 25.9 mm height reached by jet number 211, which is the minimum value up to 47.3 mm of jet number 204, which is the maximum value. Jet 211 reaches 54.7% of the height of event 204.

The bulk starting velocities (recorded at  $t = 0.35$  ms) have been normalized to the number of protons value i.e.  $10^{13}$ . One may observe that the relationship between spot size and velocity follows a polynomial law (Figure 3.16).

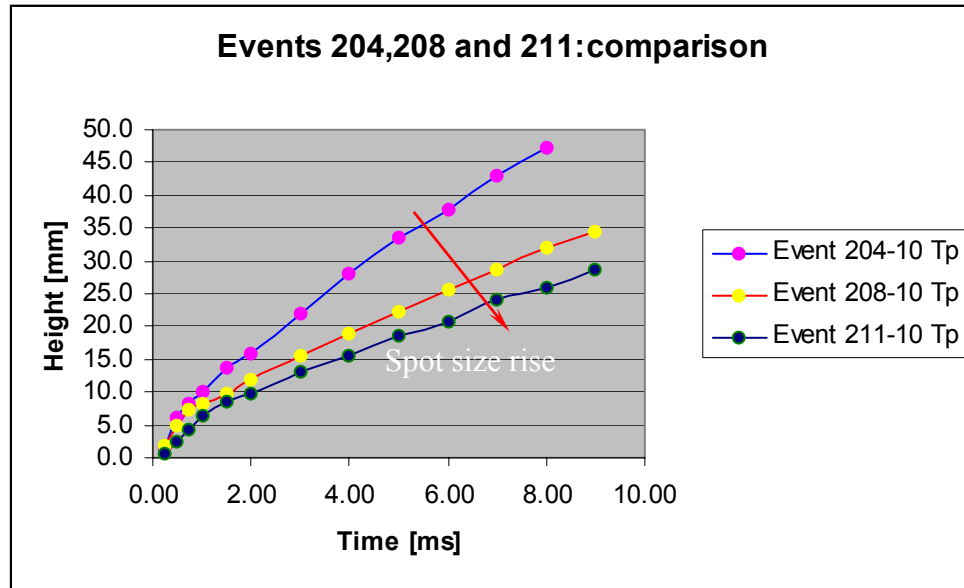


Fig.3.15: Spot size variation influence on height reached by mercury.

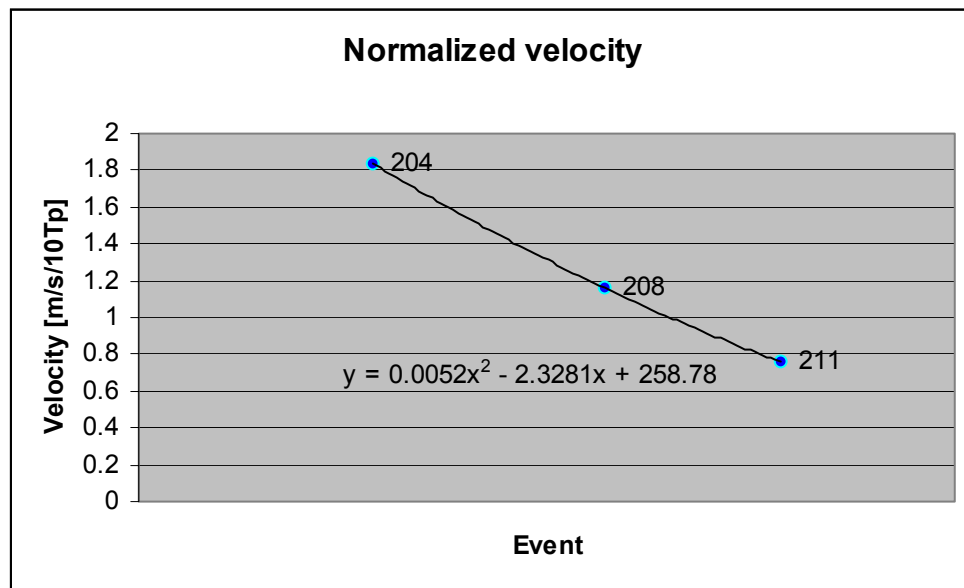
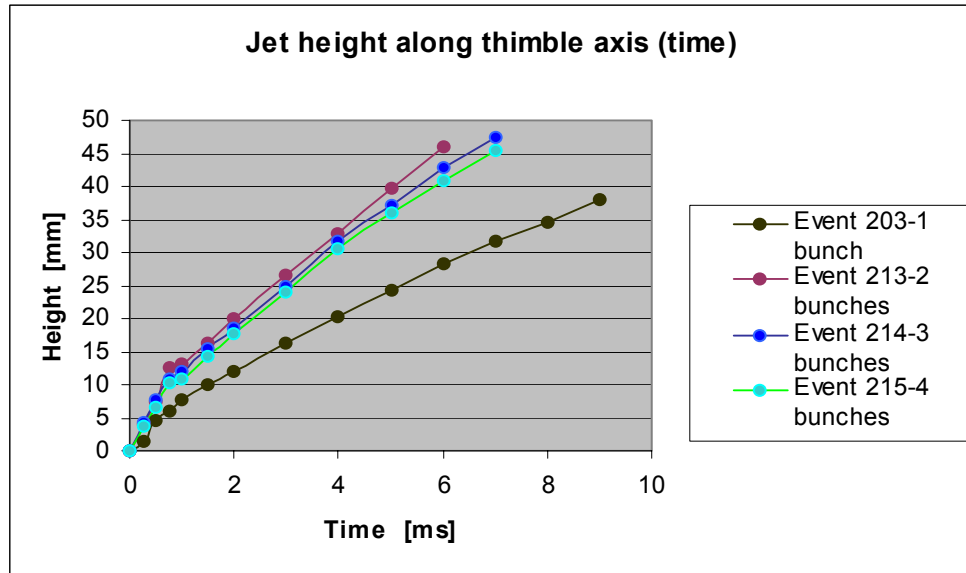
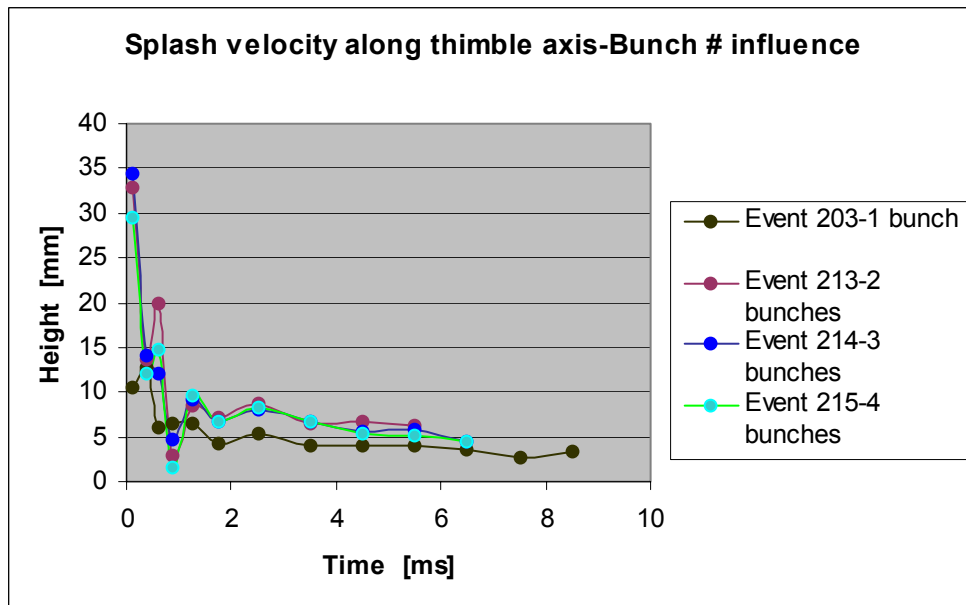


Fig.3.16: Normalized splashes' starting velocities ( $t=0.38$  ms) decrease inversely proportionally to beam spot size

From set number four it is possible to observe the influence of protons' allotment in different bunches. The total number of protons is the same between different shots (8 Tp), but divided in 1, 2, 3, or 4 bunches.



*Fig. 3.17: Number of bunches rise from 1 up to 4*



*Fig.3.18: Repercussion of bunch number on splash velocity*

Bunch spacing is constant an equal to 286 ns. Pulse length is so increased form 230 up to 1048 ns. Figure 3.17 shows the height difference between these shots while fig 3.18 shows velocities comparison.

The main difference is recognizable between event 203 and the remaining events. The influence in allotting protons in more than two bunches is not as evident as allotting protons in one or two bunches (fig. 3.19). After 6 ms height reached by jet corresponding to protons allotted in one bunch is 28.3 mm while height of jet corresponding to two bunches is 45 mm. Such a difference has repercussion also on jet's velocity as illustrated in fig. 3.17 where the main difference is visible between events 203 and 213.

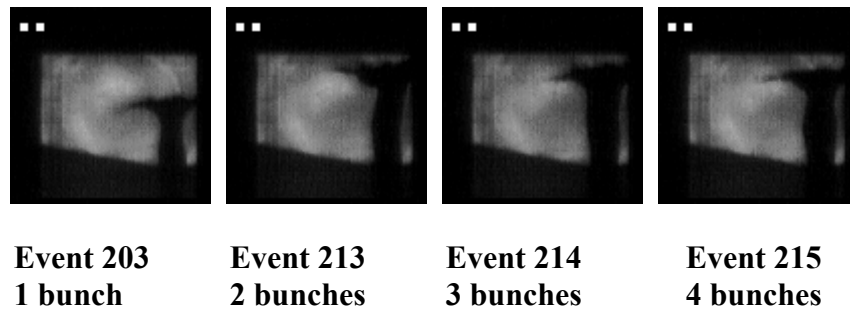


**Fig. 3.19: Influence of bunch number on jet behavior**

The same argument carried out for positions' analysis, may be done concerning velocities. In event 203 velocities are always lower than in other events, but what is more evident is speed value difference measured immediately after proton impact (see fig.3.20). In the one bunch case, splash's starting velocity is 12.8 m/s almost the half of 32 m/s average of remaining events.

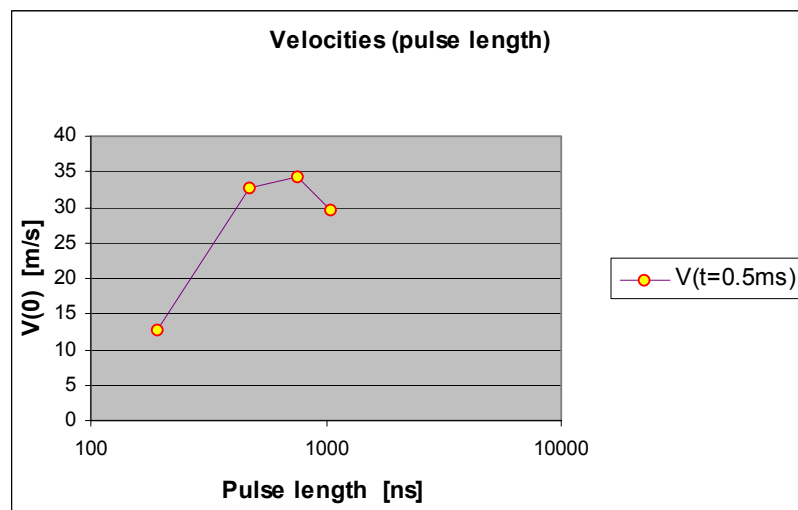


**Fig. 3.20: Splash velocities measured 0.5 ms after proton impact**



Set number five, where this parameter is increased by a factor 3 and led to 858 ns, points out the influence of increased bunch spacing. Beam features are the same of previous set 4. Global pulse length varies from 190 ns in the one bunch case up to 2764 ns in the four bunches case. Figure 3.21 analyzes heights reached by splashes in set 5. Event 203, included in previous set as well, may be taken in consideration to compare sets 4 and 5.

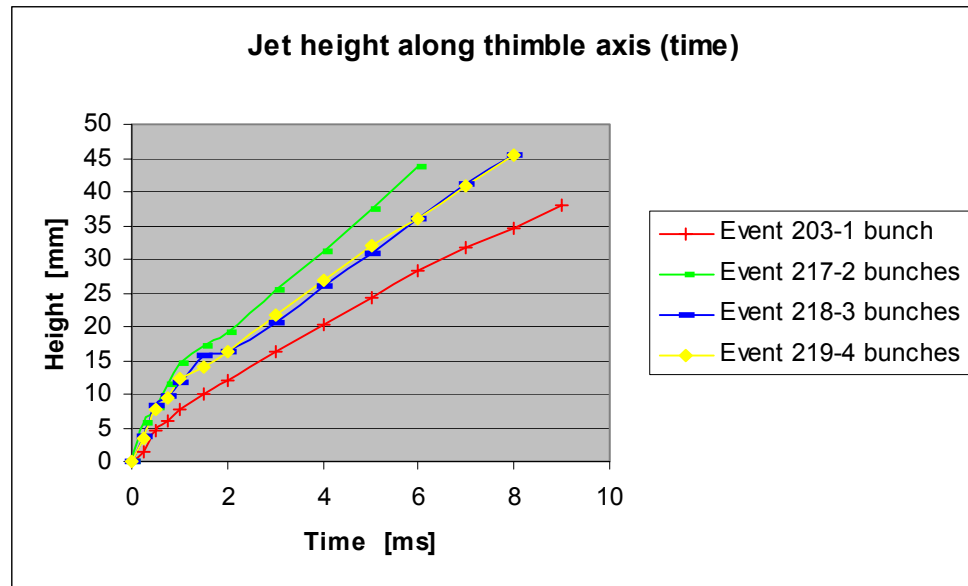


**Fig. 3.21: Splashes heights with 858 ns bunch spacing**

The same observations of previous set of pulses are confirmed even once the bunch spacing has been increased. This means that the main difference is visible between the one or two bunches case. Comparing with set 4 after 6ms height of jet in event 217 is lower of 15.5 mm than splash of event 203 while this difference was fairly higher (16.7 mm) between event 203 and 213.

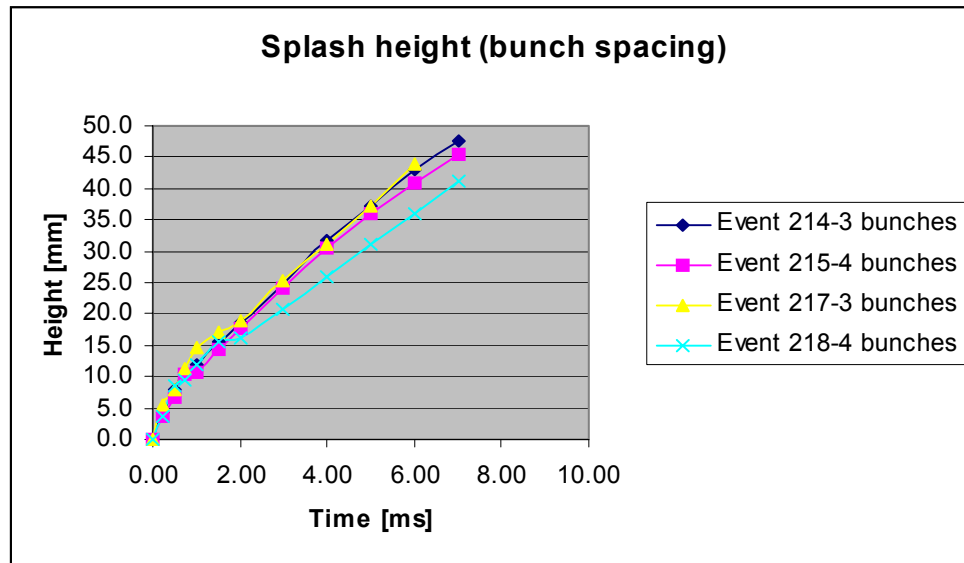


*Fig.3.22: Bunch length influence over events hit by a proton beam with the same features*

Set six shows in which way mercury reacts to a beam composed of two bunches characterized by a bunch spacing rise. The splash height of the events of set six are shown in fig. 3.23. Pictures extracted from the events at 6 ms time show the differences in height (fig. 3.24). In fig. 3.25 the initial velocity is plotted as function of bunch spacing of two bunches. One can see that for a pulse length greater than  $1 \mu\text{s}$  the velocity of explosion decreases.

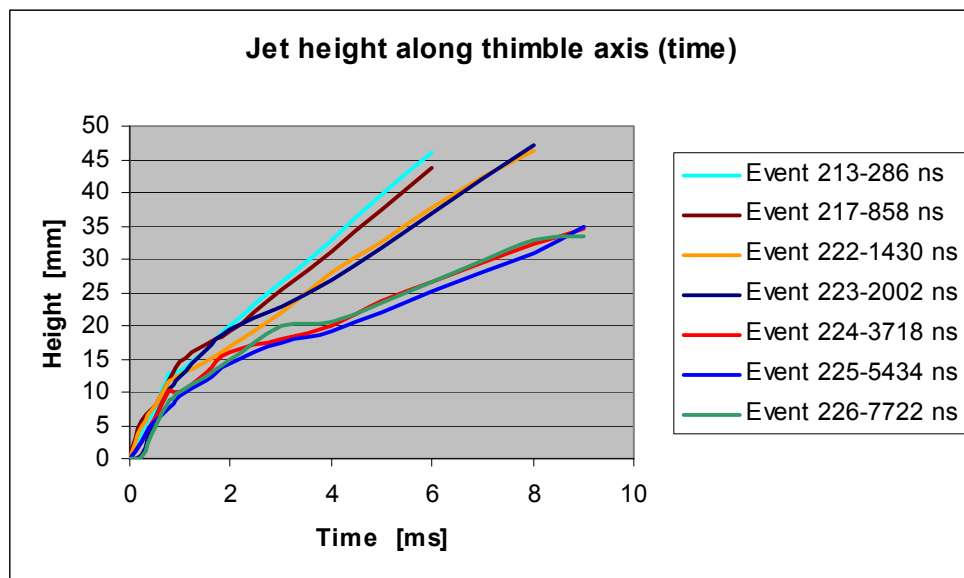


*Fig.3.23: Splash height as a function of time and bunch spacing for  $4 \cdot 10^{12} \text{ppb}$*

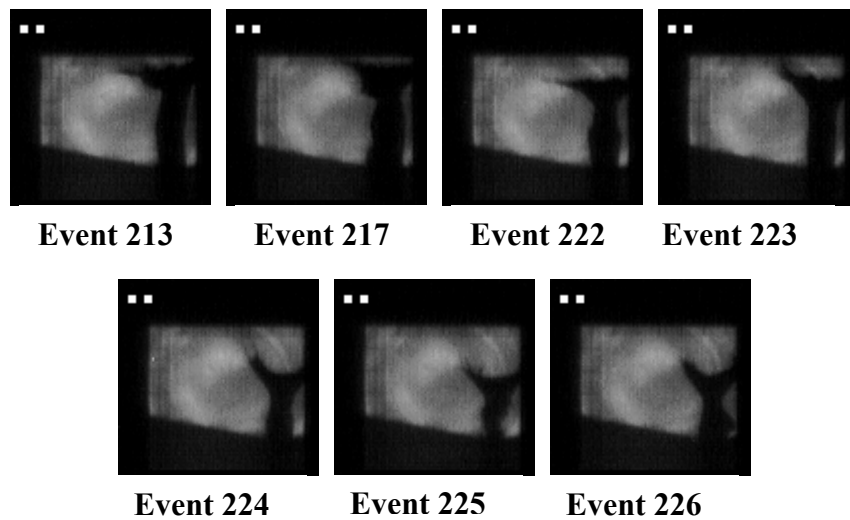


*Fig. 3.24: Pictures set 6: height rises up to 1000 ns and then lessen*

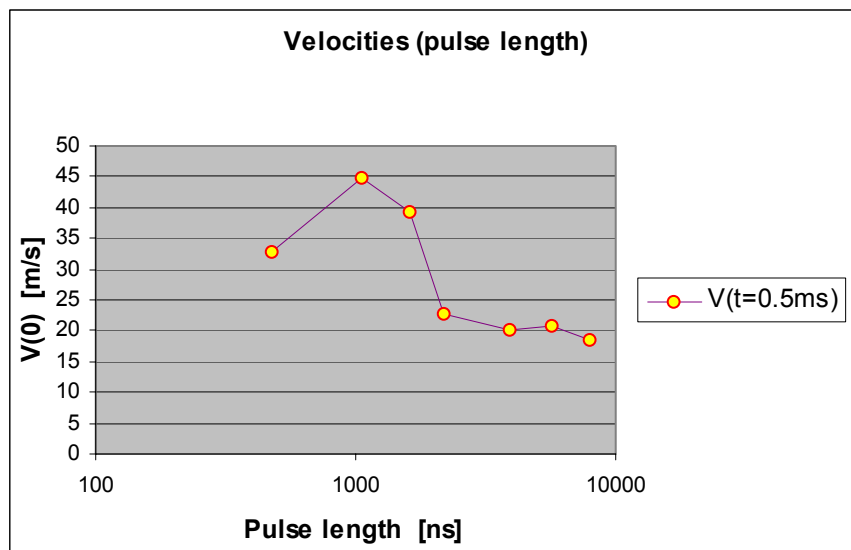


*Fig. 3.25: Pulse length influences jet's starting speed: it rises till 1000 ns and then lessen*

Pulse length influence is similar to effect of protons allotment (see set 4) in more than one bunch, a decrease of the velocity for increasing bunch spacing and consecutively pulse length over 1000 ns.

A vertical scan of the beam in relation to mercury has effects on splashes. This aspect is investigated in set number seven. The vertical position of the beam height is varied from  $-11$  mm to  $+6$  mm referred to the vertical center of the mercury thimble. Horizontal position stays centered. This exercise has been performed to assure the beam position relatively to the target

for all measurements and to determine the influence of a slight beam offset on the results achieved.

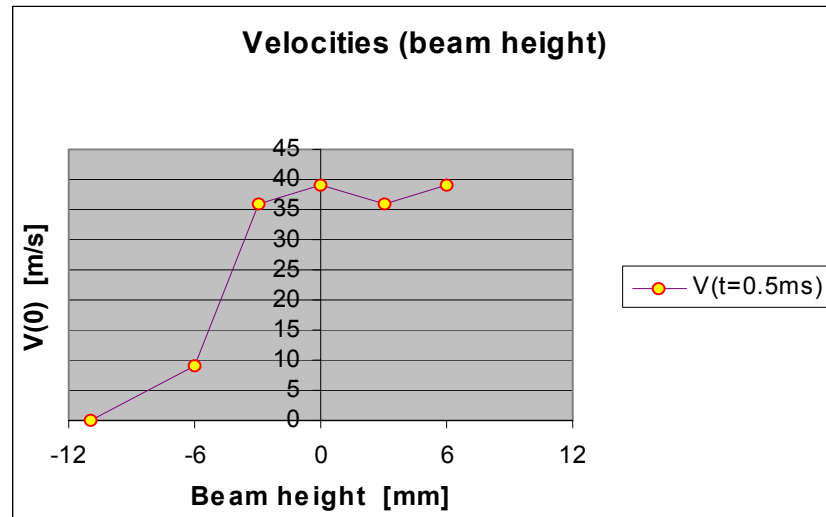


**Fig. 3.26: Effect of beam height on jet starting speed**

While differences in speed and height are negligible for events 222, 227, 228 and 229, they are not in events 230 and 231 as shown from Figure 3.26 above.

Hitting mercury 3 mm above or 3 mm below zero position difference in splash starting speed is negligible. Zero position is considered situated 6 mm from the bottom of the thimble and 6 mm from the opening of the thimble in the stainless steel frame.

Event 231 shows no movement of the mercury surface, as the target is voluntarily missed by the proton beam. Beam position  $-11$  mm is under the thimble bottom part into the stainless steel frame.

The last set of pulses aimed to verify the response of mercury contained in the thimble to an increased ppp number and to observe the order of magnitude of speeds. As it is visible from plot in Figure 3.27, velocities rises linear with intensity. Recorded velocities reach 65.6 m/s at maximum intensity available at PSB-to-ISOLDE.

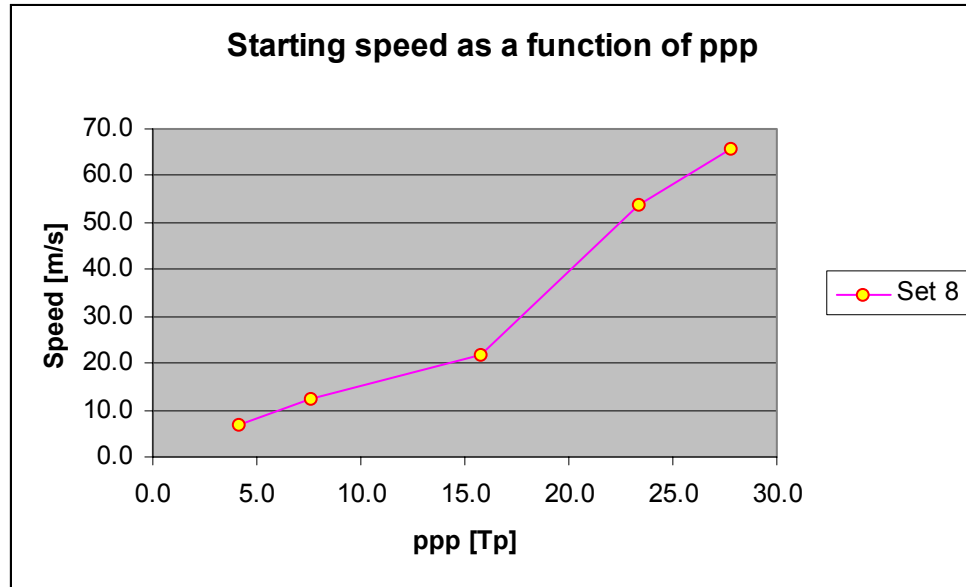


*Fig. 3.27: Starting velocities as a function of ppp*

### 3.6 Results' explanation

#### Energy deposition

As demonstrated by pictures, a mercury pool in steady state hit by an incoming proton beam reacts splashing. This phenomenon is due to beam's particle energy deposition in the mercury target. Moderately relativistic particles other than electrons lose energy in matter primarily by ionization. The mean rate of energy loss  $dE$  (or stopping power) is given by the Bethe-Bloch equation [36],

$$-\frac{dE}{dX} = kz^2 \frac{Z}{A} \frac{1}{\beta^2} \left[ \frac{1}{2} \ln \frac{2m_e c^2 \beta^2 \gamma^2 T_{\max}}{I^2} - \beta^2 - \frac{\delta}{2} \right].$$

The units are chosen so that  $dX$  is measured in mass per unit area, e.g.  $\text{g}/\text{cm}^2$ . Remaining parameters are listed in tab.3.4 below:

**Tab 3.4: Summary of variables and constants used in energy deposition equation.**

Symbol	Definition	Units or Value
$\beta$	Fraction of light speed	Adimensional
$\gamma$		$1/\sqrt{1-\beta^2}$
M	Mass of incident particle	MeV/c <sup>2</sup>
E		MeV
T	Kinetic energy	MeV
$m_e c^2$	Electron mass $\times c^2$	0.51099906 MeV
$r_e$	Classical electron radius	2.81794092 fm
$N_a$	Avogadro's number	$6.022 \times 10^{23} \text{ mol}^{-1}$
z	Charge of incident particle	
Z	Atomic number of medium	
A	Atomic mass of medium	G/mol <sup>-1</sup>
K/A	$4\pi N_a r_e^2 m_e c^2 / A$	0.307075 MeV g <sup>-1</sup> cm <sup>2</sup>
I	Mean excitation energy	eV
$\delta$	Density effect correction to ionization loss	
$h_{op}$	Plasma energy	$28.816 \sqrt{\rho Z/A} \text{ eV}$

### Thermodynamic interaction

When an incident proton beam hits a target, around the 25% of its power is deposited on the target. Two processes are initiated: thermodynamic response and pressure wave initiation and propagation [25]. This power is deposited within a few nanoseconds and lead to rapid temperature raise and stresses in the material [37]. Since the rise time of temperature is of the same order of magnitude as the deposition of beam energy, which is  $10^{-9}$ s, thermal expansion is initially prevented by the mass inertia of the material. The resulting instantaneous peak of pressure ( $\Delta p$ ) at time  $t = 0$  can be estimated using the approximate formula:

$$\Delta p = \frac{\alpha_v \Delta T}{k}$$

where:

- $\alpha_v = (\partial V / \partial T)_p = 18.1 \times 10^{-5} \text{ [K}^{-1}\text{]}$  is the volume thermal expansion coefficient of mercury
- $k = 0.45 \times 10^{-10} \text{ [m}^2\text{/N]}$  is the compressibility of mercury [38]

considering an average  $\Delta T$  for all analyzed events of 87 K lead to an average  $\Delta P$  of 349.9 MPa.

For liquid metal targets it is relevant to assess the internal energy  $E_c$  stored in the material due to the initially prevented thermal expansion of the target as this might be converted into kinetic energy ripping the liquid apart.

Mercury's movement is due to expansion and to pressure wave generated by beam impact that tears mercury apart. The energy density  $dE_c/dV$  is given by:

$$\frac{dE_c}{dV} = \frac{(\alpha_v \Delta T)^2}{2k}$$

by integrating over the volume, the total energy  $E_c$  convertible to velocity for the assumed Hg-target of  $1.18 \text{ cm}^3$  volume is about:

$$E_c = 3.25 \text{ J/pulse}$$

Considering all this energy converted in kinetic energy of the whole mercury contained in the thimble, in first approximation the resulting speed expected from the splashes is given by:

$$K.E. = 1/2 \rho dV \Delta v_m^2 = \Delta P \delta(dV)$$

where:

- $\rho = 13.546 \text{ g/cm}^3$  is mercury density
- $dV$  is the infinitesimal volume of mercury experiencing a change of temperature  $\Delta T$  and pressure  $\Delta P$
- $\Delta v_m$  mercury's resulting velocity
- $\Delta P$  as calculated above
- $\delta(dV) = \alpha_v dV \Delta T$

results a velocity:

$$\Rightarrow \Delta v_m \approx 28 \text{ m/s}$$

which is not far from what has been experimentally measured.

By inspecting the kinetic energy density  $dE_c / dV$  and its integral over the target volume it can be shown that the total kinetic energy  $E_c$  deposited in the target is proportional to the temperature rise  $\Delta T$  on the target. From this it results that  $E_c$  depends on the radius of the beam as  $1/R^2$ , i.e.  $E_c$  rises sharply with narrow beams.

### 3.6.1 Number of protons

As illustrated in events' analysis, the number of protons per pulse shot strongly influences mercury's behavior. This is a consequence of Bethe-Bloch equation since the energy deposited in the target is directly proportional to number of particles interacting with matter.

Consequences on height reached by mercury and on its velocity has been discussed in section 3.2.7 and illustrated in Figures 3.11 and 3.12. In Figure 3.28 starting velocities recorded after 0.5 ms related to set 1 are represented.

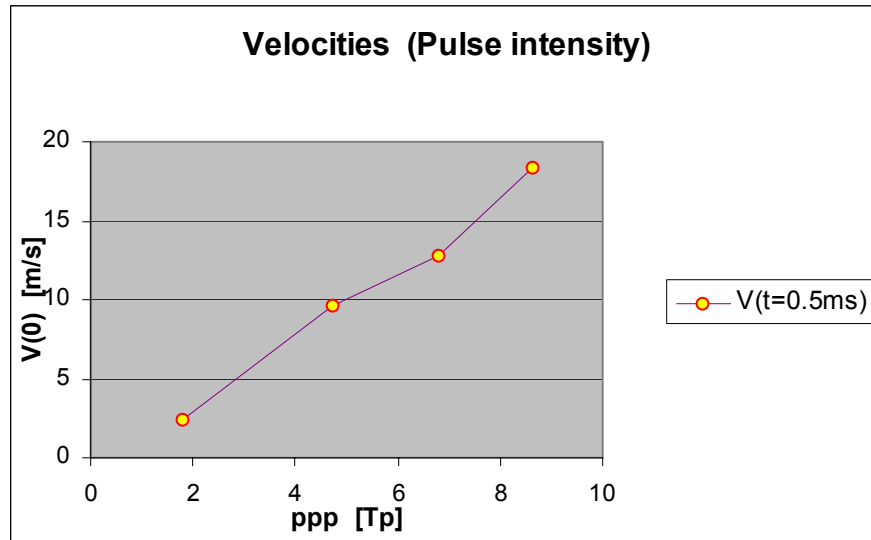


*Fig. 3.28: ppp influence on  $v$  ( $t=0.5ms$ )*

Set one pointed out that the higher is the energy deposition in the target, the higher is the speed resulting on the jet whether starting or during all motion.

### 3.6.2 Spot size influence

This feature may be pointed out observing influence of beam spot size on splashes' velocity as precedently illustrated in Figure 3.14. As may be verified from the plot, as a consequence of a rise of spot size, i.e. a reduced surface density of protons, a much lower height as a function of time is measured. After 8 ms height reached by mercury splash caused by impact of a 3.5 mm spot size beam is 25.9 mm while height corresponding to splash caused by 2.2 mm spot size beam is 47.3 mm; almost double. One can estimate a inverse behavior of first order between spot size and explosion velocity. This conclusion is vague as the statistics on this dependency are rather low (4 events).

### 3.6.3 Pulse length influence

Pulse length influence over mercury bulk's initial velocity is represented in Figure 3.25. One may observe that velocity drops for a pulse length longer than  $3 \mu s$ . This could be due to traveling of the pressure wave induced by the proton beam.



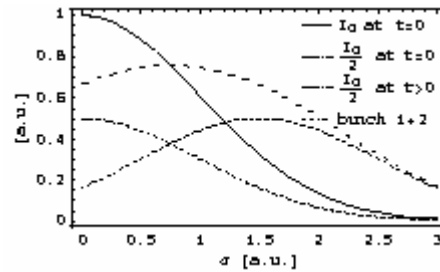


**Fig.3.29: Plot of traveling pressure wave**

In Figure 3.29 one can see that the pressure wave caused by a pulse composed of one bunch has an amplitude  $I_0$  at  $t=0$ . This wave has, at the same time, an amplitude double of the pressure wave caused by the two-bunch beam impact. This is due to half bunch intensity.

When the first of the two bunches hits the target it generates a pressure wave that has amplitude of  $I_0 / 2$ . When the second incoming bunch hits the mercury pool generates a pressure wave equal to the first one. The time distance that separates the two bunches allows the first pressure wave to propagate. The superposition of the two waves results in a wave equal to the sum of the two waves. This wave has an amplitude lower than the sum of the two amplitudes corresponding to each wave and it is shifted aside the beam axis. For  $t > 0$  the first pressure wave has traveled and a mass is displaced together with it according to equation:

$$\frac{dV}{dt} = - \frac{dP}{dr}.$$

Where  $P$  is the pressure propagating,  $r$  is the radius of cylinder around the incoming beam and  $dV/dt$  is the displaced mass' acceleration.

For bunch spacing shorter than  $3 \mu s$  the pressure wave has not yet completely propagated. For a bunch length higher than  $3 \mu s$  the pressure wave caused by the first bunch has already propagated more than the width of the beam spot size.

The extended pulse length causes a lower interaction beam/target with a consequent lower energy deposition and lower bulk velocities.

### 3.6.4 Vertical scan effect

All other pulses than from set number seven have been shot centered vertically and horizontally on the thimble. Horizontal alignment was maintained while vertical position was displaced. As in each pulse shot the proton beam interacted with the stainless steel frame before colliding with the mercury pool, this test aimed to verify that mercury's movement was not due to heat transfer or shock wave propagation between the heated frame and the mercury pool. The second goal to achieve consisted in verifying what happens hitting the target in positions different from the central one.

From plot of Figure 3.25 (section 3.2.7) one may observe that, since the mercury bulk does not move when the beam is displaced 11 mm towards the bottom part of the frame, mercury's movement is strictly related to collision.

When the beam is displaced 6 mm below zero position, measured velocity is lower of a factor four if compared to other events (9.2 m/s instead of 36 m/s). This is due to higher mass that has to be displaced applying the same energy of the other events.

Concerning vertical scan of  $\pm 3$  mm, speeds remain in the same order of magnitude (36 m/s) of the zero position one (39.2 m/s). A slight difference may be pointed out concerning + 6 mm position. Resulting speed is higher cause the lower mass to be displaced applying the same energy resulting from beam impact.

### **3.7 Jet's behavior analysis**

All recorded events demonstrated to have common features. All measured velocities as a function of time had a quite similar trend. As a consequence of beam impact, velocities show a peak within the first 1 ms and after begin to decrease. Event 204 has been chosen as representative of all the events to explain phenomenon that take place after beam impact.

In order to have a higher accuracy, measurements have been recorded with a higher frequency. All jet's positions, starting from the first frame of movement up to the last frame in which the jet had reached the experimental chamber top part, have been recorded. In Table 3. 5 below, all measurements are illustrated.

Tab. 3.5: Event 204 logbook

Frame	Time	height	dh/dt	V(t)	$x(t)=Vot-1/2gt^2$	V(t)	x(t)	g_t
	[ms]	[mm]		[m/s]	[mm]	[m/s]		
1	0.25	1		2.5	1.750	6.90	1.71	-385
2	0.50	2	8.00	7.4	3.499	6.80	3.40	-374
3	0.75	5	12.00	14.9	5.247	6.70	5.07	-363
4	1.00	8	8.00	9.9	6.995	6.60	6.71	-353
5	1.25	9	6.00	6.2	8.742	6.50	8.32	-342
6	1.50	11	6.00	6.2	10.489	6.41	9.91	-332
7	1.75	12	6.00	5.1	12.235	6.31	11.48	-322
8	2.00	14	6.00	6.2	13.980	6.21	13.02	-312
9	2.25	15	4.00	5.1	15.725	6.11	14.54	-302
10	2.50	16	6.00	8.6	17.469	6.01	16.03	-292
11	2.75	18	4.00	8.7	19.213	5.91	17.50	-283
12	3.00	18	4.00	4.9	20.956	5.81	18.94	-273
13	3.25	20	8.00	4.9	22.698	5.71	20.36	-264
14	3.50	22	6.00	3.9	24.440	5.61	21.76	-255
15	3.75	23	4.00	3.9	26.181	5.51	23.13	-246
16	4.00	24	4.00	4.9	27.922	5.41	24.48	-237
17	4.25	25	6.00	8.6	29.661	5.32	25.80	-229
18	4.50	27	6.00	3.7	31.401	5.22	27.10	-220
19	4.75	28	4.00	9.9	33.139	5.12	28.37	-212
20	5.00	29	4.00	4.9	34.877	5.02	29.62	-204
21	5.25	30	4.00	4.5	36.615	4.92	30.84	-196
22	5.50	31	4.00	3.7	38.352	4.82	32.04	-188
23	5.75	32	6.00	3.7	40.088	4.72	33.21	-180
24	6.00	34	6.00	3.7	41.823	4.62	34.36	-173
25	6.25	35	4.00	3.7	43.558	4.52	35.49	-165
26	6.50	36	4.00	3.9	45.293	4.42	36.59	-158
27	6.75	37	4.00	4.9	47.027	4.32	37.67	-151
28	7.00	38	4.00	6.2	48.760	4.23	38.72	-144
29	7.25	39	6.00	4.9	50.492	4.13	39.75	-138
30	7.50	41	6.00	3.8	52.224	4.03	40.75	-131
31	7.75	42	4.00	3.7	53.955	3.93	41.73	-125
32	8.00	43	4.00	4.9	55.686	3.83	42.68	-119
33	8.25	44	4.00	3.7	57.416	3.73	43.61	-113
34	8.50	45	5.33	3.9	59.146	3.63	44.51	-107

Calculations may be referred to a mercury droplet as first approximation in order to apply basic fluid dynamical concepts to phenomenon under investigation.

The mercury droplet may be assumed as a spherical particle moving free inside a fluid. In this case the fluid is argon. The general equation of a particle inside a fluid is [39]:

$$\frac{\pi d^3}{6} \rho_p \frac{D\vec{v}_p}{Dt} = 3\pi\mu d (\vec{v}_f - \vec{v}_p) - \frac{\pi d^3}{6} \rho \frac{Dv_f}{Dt} + \frac{\pi d^3}{12} \rho \left( \frac{Dv_f}{Dt} - \frac{d_p \vec{v}_p}{dt} \right) + \frac{3}{2} d^2 \sqrt{\pi\mu\rho} \int_0^t \frac{d\tau}{\sqrt{t-\tau}} \left( \frac{Dv_f}{Dt} - \frac{d_p \vec{v}_p}{dt} \right) + F_{ext}$$

with:

- $d$  is particle's (droplet) diameter
- $v_p$  is particle's velocity
- $v_f$  is the velocity of the fluid
- $\rho_p$  is density of the particle
- $3\pi\mu d$  is the friction coefficient for a sphere
- $\frac{D\vec{v}}{Dt} = \frac{\partial\vec{v}}{\partial t} + \vec{v} \cdot \nabla \vec{v}$

The left member is the product of the particle mass by the acceleration; on the right part are five factors that represent the various forces acting on the particle:

- The first one is the viscous drag expressed by Stokes' law
- The second one represent the influence of the pressure gradient
- The third one represents the inertia effects due to the fluid mass carried by the particle
- The fourth one, called Basset force, takes in consideration the history of the particle accelerations, the most recent being the most important
- The last one includes external forces as gravity surface tension electrostatic ones.

When estimating the order of magnitudes of these five factors, it appears that in first approximation, in order to estimate mercury's behavior, is sufficient to consider only the viscous drag and gravity forces. Assuming spherical droplets, lift force is equal to zero cause the symmetry of the solid considered.

The differential equation of motion becomes:

$$m_p \frac{\partial\vec{v}_p}{\partial t} = \frac{1}{2} \rho_f (v_f - v_p)^2 C_D \frac{\pi d^2}{4} + m_p g$$

with:

$C_D$  drag coefficient for a sphere immerse in a fluid. For  $Re < 100$ ,  $C_D$  depends on Reynolds number according to[41]:

$$C_D = \frac{24}{Re} \left( 1 + \frac{3}{16} Re \right)^{\frac{1}{2}}$$

considering:

- $4 \times 10^{-5}$  m as droplet diameter
- 7 m/s average speed after the starting velocity peak
- $0.02217 \text{ Cp} \rightarrow 2.217 \times 10^{-5} \text{ m}^2/\text{s}$  Ar cinematic viscosity [42]
- $1.7837 \times 10^{-3} \text{ g/cm}^3$  Ar density

Reynolds' number results  $Re = 12.63$ , which lead to  $C_D = 3.48$ . Normalizing the differential equation of motion over the droplet's mass value and assuming  $v_f = 0$  is:

$$a_d = \frac{d\vec{v}_{pv}}{dt} = \frac{3}{4} \frac{\rho_f}{\rho_p} (-v_p)^2 C_D \frac{1}{d} - g$$

where  $v_{pv}$  is droplet vertical speed. The resulting acceleration  $a_d$  on the droplet is  $a_d = -411.2 \text{ m/s}^2$ .

### 3.7.1 Positions

The viscous drag is a force that is not constant in time, but decreases with  $v^2$  as a function of droplet's height. The global acceleration on the droplet is so lower when it is in higher positions. By estimating this value, it is possible to plot the difference between the real phenomenon, the ideal (no friction with gas medium) and the experimentally measured values. Floating acceleration value  $g(t)$ , called  $g_t$  in tab 3.VI, is inserted in equation:

$$x(t) = x_0 + v_0 \cdot t + \frac{1}{2} g(t) \cdot t^2$$

where:

$v(t)$  is the velocity calculated by the formula of uniformly accelerated motion (see next paragraph 3.7.2 for calculation)

$dt = 0.25 \text{ ms}$  is the time between two consecutive images.

Assuming a starting speed  $v_0 = 7 \text{ m/s}$  the ideal case of uniformly accelerated motion is represented by equation of cinematic:

$$x(t) = v_0 \cdot t + \frac{1}{2} g \cdot t^2$$

It is so possible to compare in a plot: measurements, calculated positions and ideal case as illustrated in Figure 3.30.

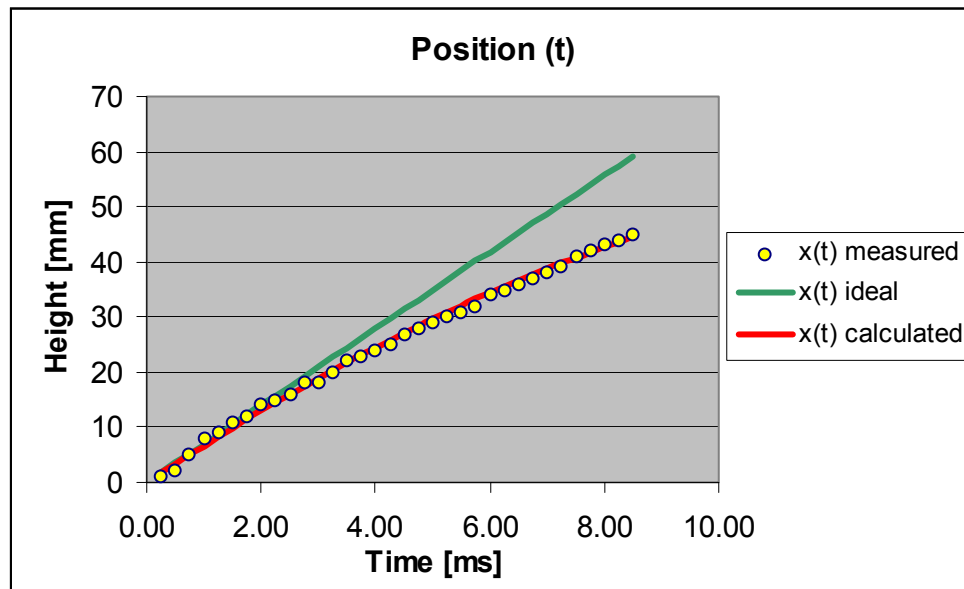


*Fig. 3.30: Heights' comparison: measured values, calculated and ideal case*

During the first 2 ms the trends of measured positions and the calculated ones is quite similar to ideal case, then the influence of drag force and gravity force becomes more relevant and the plots begin to diverge cause fluid deceleration.

The good quality of considered approximation is demonstrated by the coincidence of experimentally measured values and the calculated ones.

### 3.7.2 Velocities

Contribute to droplet deceleration caused by gravity is constant with time and mercury's speed as well. Its value during the first 8 ms of motion, considering gravity acceleration  $g = -9.81 \text{ m/s}^2$  may be estimated as  $7.8 \times 10^{-2} \text{ m/s}$ .

The remaining part of deceleration due to friction of argon over the droplet is not constant as mentioned above. In plot of Figure 3.31, it is first plotted the equation of uniformly decelerated motion considering the acceleration  $a_d$  calculated in par. 3.7:

$$V(t) = v_0 - \frac{1}{2} a_d \cdot t.$$

This equation may be compared to what happens to mercury during the deceleration stage according the other plots illustrated.

The equation is reported together with velocity's value experimentally measured and with  $dh/dt$  values. The  $dh/dt$  values are average of speeds calculated considering positions of mercury at two images distances and divided by time (0.5 ms).

The plot shows that inside the fluid, velocity fluctuations are present. Turbulent motion conditions are so visible. Deceleration stage seems to fit with the trend of what happens in the ideal case.

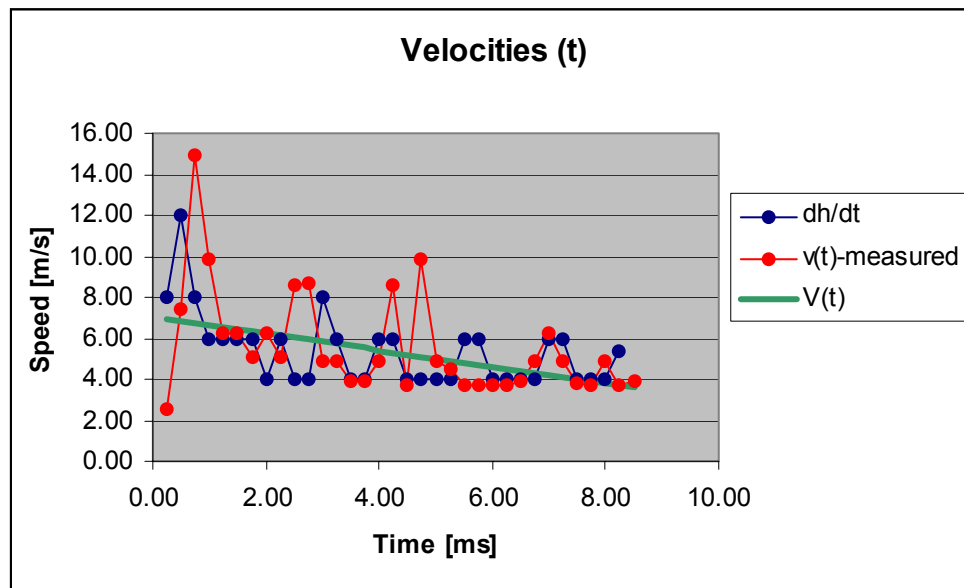


*Fig.3.31: Velocity's trend compared with uniformly decelerated motion*

### 3.7.3 Jet shape analysis

All jets that reached a sufficient height to be analyzed showed almost the same shape. Jets are fundamentally rising cylinders. Their first reaction to proton impact is a slight cloud of mercury droplets traveling much faster than mercury's bulk that separates from meniscus surface. This cloud is due to the propagation of the first pressure wave towards the free surface. Nevertheless with the available camera's resolution it is not possible to measure these droplets' velocities, as the spatial resolution of the camera is limited to approx. 1 mm. This very fast cloud could only be observed by American colleagues having a resolution about twice as good.

Jets could fly for a 50mm path before hitting the top part of the experimental chamber. Considering a cylindrical shape of the jet, a height of 50mm and a homogenous distribution of the liquid within the jet, its diameter results of 5.5 mm. This value is lower than what is expected to be as thimble diameter is 12mm. Moreover mercury is expanding outside the thimble while it leaves it and measured values on the images justify this assertion. An example is given in Figure 3.32.

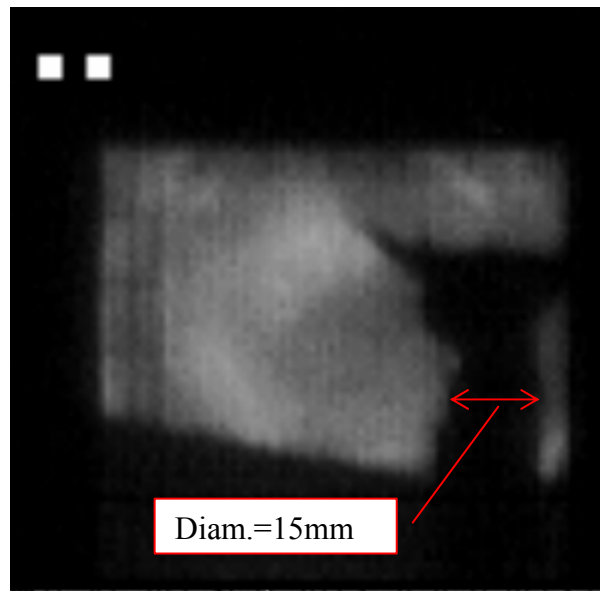


***Fig. 3.32: Jet diameter (15mm) is higher than estimated value (5.5 mm)***

It is rightful to think about the possibility of having a cavity inside the jet, but this thesis is not demonstrable by observing taken images.

All jets showed a common feature. They all have two “arms” extending on both sides of the jet. This phenomenon has still to be investigated and understood.



### 3.8 Conclusions

Scaling laws have been derived for the explosion velocity as a function of different beam parameters. This allows estimating the effect of proton induced shocks for a full scale  $\nu$ -factory.

At the thimble test measured velocity were up to 45 m/s for maximum beam intensity. The proton beam parameters of ISOLDE are different from the CERN scenario for  $\nu$ -factory by:

- Proton intensity will be eight times higher.
- Spot size is increased by four times ( $r=7.5$  mm)
- From BNL events one concludes, that the in the case of the thimble the explosion velocities are two times higher than in the case of the jet, which free surfaces is larger. [49]
- The jet will be under vacuum. This leads to elimination of drag force and consecutively to higher speeds.
- The pulse length is of the same order ( $3.2 \mu\text{s}$ ). Within this time sound waves travel about 5mm.
- Proton energy rises from 1.4 GeV to 2.2 GeV. According to Bethe-Bloch formula the energy deposition  $dE/dx$  will be 30 % less.

This results in explosion velocities about two times the initial jet velocity of 25 m/s. The so caused explosion causes the mercury jet to stop and fill the target area. Part of the mercury target is even directed in backwards direction of the initial jet speed. By this the target area is filled and the successive jet is blocked from entering it. The possibility of changing some parameters of the present design for  $\nu$ -factory are pointed out in the following statements.

- The spot size is fixed by the horn dimension
- Beam energy of 2.2 GeV is already the value for a minimum  $dE/dx$ .
- The presence of an atmosphere could slow the velocities due to induced drag force of splashing jet. A stream of gas around the target would also support the removal of spilled mercury from the target area.
- A pulse length in the order of  $100\mu\text{s}$  would solve the problem of explosion. This option is of course not available. The downstream accelerators for a neutrino factory do not accept a major change to the pulse structure as given.

# Chapter 4

## Interaction between a Mercury Jet and Magnetic Field

### 4.1 Introduction

In the US scheme for a neutrino factory the interaction between proton beam and the mercury jet target takes place inside a high magnetic field, which serves as a focusing device for the produced particles. We aimed to investigate magneto-hydro-dynamic effects occurring in the target area. Injecting the liquid metal target at a speed of more than 10 m/s into a 20 Tesla solenoidal magnetic field causes forces on the liquid. The repulsion and pinching of the liquid jet will be studied experimentally. This field of study is referred to as Magneto Hydrodynamics (MHD).

#### 4.1.1 Magneto Hydrodynamics

MHD or magneto hydrodynamics is a physical phenomenon acting on fluids displacing into a magnetic field. Whenever a conductor moves inside a magnetic field, a force opposing to its motion born inside the conductor itself. Equations characterizing MHD constitute a system of differential equations comprehending Lorentz' law, differential equations of motion and of electrodynamics. According this law a particle having a mass  $m$  and charge  $q$  is subject to the Lorentz force [32]:

$$F_{Lorentz} = m \cdot \frac{d\vec{v}}{dt} = q(\vec{E} + \vec{v}_0 \times \mu \vec{H})$$

where:

- $E$  is the electric field [kg·m/s<sup>2</sup>/C], which is zero in this case
- $\mu \cdot H$  is the magnetic flux density [kg/C·s]
- $v$  is the velocity of the particle moving into the magnetic field [m/s]

Graphic representation of the law is (fig. 4.1):

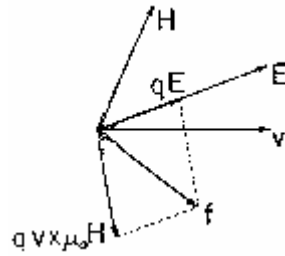


*Fig. 4.1: Lorentz' law: composition of vectors*

Inside the conductor Eddy currents are produced. The current generates a magnetic field, which interacts with the main one according to Lenz' law. In our target case the conductor is a liquid metal. For the experiments performed the advantage of availability and due to its good properties in means of pion production the high-Z material mercury was chosen.

#### 4.1.2 Previous experiments

Preliminary tests have been carried out at the Grenoble High Magnetic Field Laboratory (GHMFL-M5). A collinear injection in a field gradient  $dB/dz$  of  $-60$  to  $60$  T/m have been performed [33].

The jet studied was a 5-15 m/s and 3 mm diameter mercury jet. Measurements of velocity and shape of such a jet entering on axis into a 13 T vertical bore 130mm solenoid have been taken closed to the maximum field gradient. At velocities of  $\approx 5$  m/s a modification of the tip of the jet was observed for the highest field gradient. No other visible effects were observed at higher velocities. Concerning the jet shape, the turbulence of the jet was likely to hide effects leading to deformation below 0.5 mm.

#### 4.2 The experimental set up

The construction of the set up was carried out in CERN's workshops while the experiment itself was performed at Grenoble High Magnetic Field Laboratory (GHMFL) since no magnets able to generate a 20T magnetic field are available at CERN. The laboratory is located inside the CNRS campus of the Poligone Scientifique Luis Neel and is a French-German laboratory. The experiment set up comprehends parts of the set up used in previous experiment carried out with the GHMFL M5-13T magnetic field magnet. The set up has been updated according to new needs dictated by the higher magnetic field used and the geometry of the magnet bore.

### 4.2.1 The magnet

The GHMFL is provided of several magnets. The available resistive magnets provide DC fields up to 30 T in a 50 mm bore diameter. For the experiment described here, the 20T resistive magnet, named M9, was used.

The magnet is made with copper-based windings, of the Bitter type and polyhelix insert. The power supply is a voltage of about 400V at full power. The maximal current flowing in the 20MW M9 magnet is about 13 kA and provides a 20T steady magnetic field. The rate of variation of the current (and therefore of the magnetic field) is manually programmed by the control panel dB/dt value. The cooling of magnet is provided by a circulation of deionized and deoxygenized water with a flow reaching up to 1000 m<sup>3</sup>/h.

The magnet experimental area is constituted by a vertical bore. The field values are measured inside the bore. Our set up had to be inserted into the magnet bore that has a diameter of 130mm (see Fig.4.2 for top view of the magnet).



*Fig. 4.2: M9-20T magnet/top view: the bore*

The magnetic field value is not constant in the whole experimental section as there is a gradient along the bore axis. The maximum magnetic field value is situated at the half height of the magnet. The on-axis field is indicated in Figure 4.3, where the M9 bore, the experimental set up and the magnetic field values across the axis are represented. The

experimental set up is inserted and extracted from the magnet bore by an elevator fixed next to the magnet.

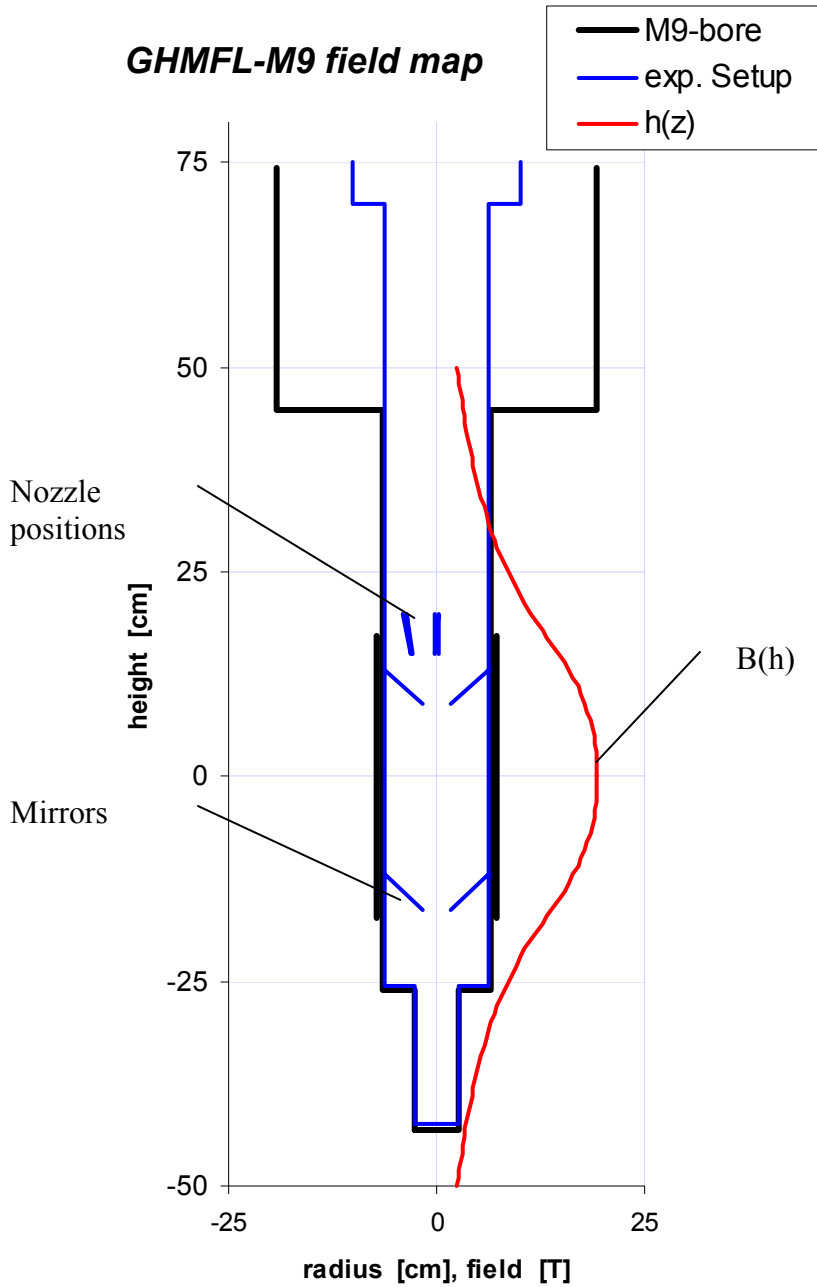


**Fig. 4.3: Placement of set up relative to magnet bore M9, schematization of M9-20T magnetic field distribution. Upper and lower positions of mirrors and two nozzle positions are indicated**

### 4.2.2 Concepts of the experimental set up

This study aimed to investigate the behavior of a 10 m/s mercury jet injected into a 20T solenoidal magnetic field. On such a jet pronounced magnetohydrodynamics effect are expected to be seen. The maximum magnetic field of 20T at M9 is the nominal magnetic field foreseen in CERN's neutrino factory scenario.

The goal of the experiment was to record by photographic methods the MHD effect on a pulsed mercury jet entering a solenoidal field under an injection angle of  $0^\circ$  and  $6^\circ$ . The full set up has been designed in order to perform the injection of the jet inside the vertical bore of the high magnet.

The experiment set up required an injection system able to shot mercury inside the magnetic field. An air driven piston pump sucks mercury from a main reservoir and injects it into the 'heart' of the system, the jet chamber. A ball tip valve triggers the injection of the mercury stream. The produced stream is forwarded through a nozzle into an experimental chamber designed to fit into the magnet vertical bore. The jet can be observed via an optical mirror system.

Spilled mercury is collected into a tight recipient located below the experimental chamber and pumped back to the main reservoir by means of a hydraulic circuit. Sucked mercury is then pumped again into the pressurized circuit. The whole system is provided with a double confinement in order to avoid mercury spills in case of break-down of the system.

Materials of all components had been chosen according needs of full compatibility with mercury (see Table 2 appendix 2). Moreover, the whole set up was supposed to be working in a high magnetic field area. Thus in addition to compatibility with mercury non-ferromagnetic materials had to be chosen for building the experimental set up.

The acquisition consists of the "Encore MAC" high-speed camera system used in the "thimble" test experiment.

### 4.2.3 Flowchart

In Figure 4.4 the flow chart of the experiment set up is given. The drawing represents how all the components of the equipment are interconnected. The whole equipment has been subdivided in groups characterized by different colors. Each color correspond a group of devices absolving different functions. In Figure 4.4 four groups are visible:

- Blue colored items represent mercury suction and ejecting components
- Azure colored items represent the experimental chamber
- Green colored parts are referred to mercury recovery system
- Red colored components comprehend the triggering system, the electro pneumatic valve

The full list of installed parts is reported below Figure 4.4.

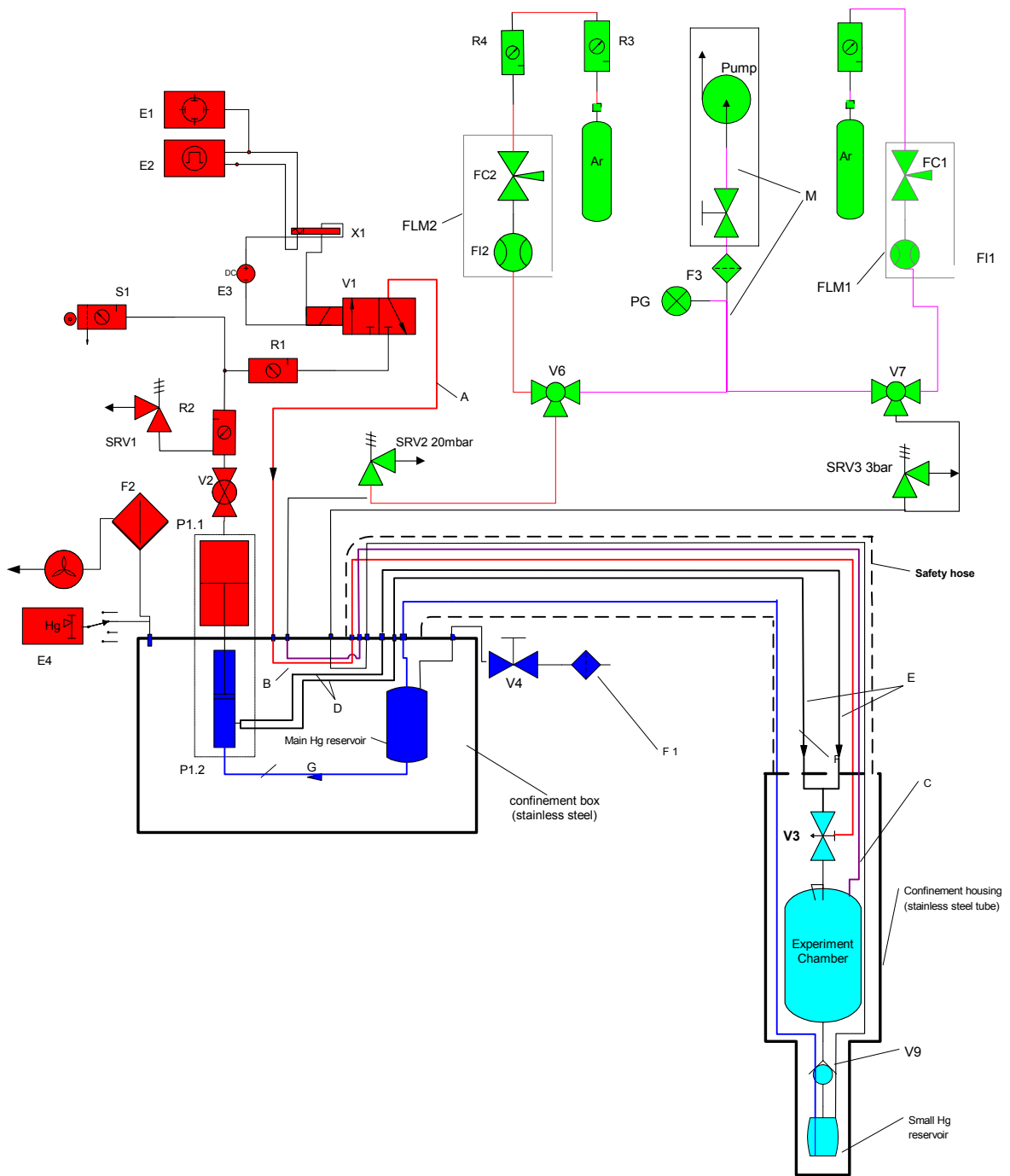


**Fig. 4.4: Flow chart of experimental set up used to investigate MHD effects on mercury jets stressed by a 20T magnetic field**

**List of parts:**

E1 Oscilloscope Tektronix TDS3032 300Mhz, 2.5Gs/s  
 E2 Pulse Generator Philips/Fluke PM5786B 1Hz-125MHz  
 E3 Power Supply 24V DC  
 E4 Mercury Vapor Detector Mercury Instruments VM-3000  
 F1, F2 Charcoal Filter  
 FLM1,FLM2 Flow meter Vögtlin Q80EE S1 M12G A2.0E luft 1.6-16; 4-40;6-60

FC1 Flow Control for Noble Gas  
 FC2 Flow Control for Noble Gas/Air  
 FI1,FI2 Flow Indicator (Flow meter) 0-10 l/min  
 PG Pressure gauge for under-pressure  
 P1.1 NORDSON 25B Piston Pump, Air Motor  
 P1.2 NORDSON 25B Piston Pump, Hydraulic Section  
 P3 Rotary pump

R1 Air Pressure Regulator  
 R2 Air Pressure Regulator  
 R3 Pressure Regulator for Argon LHC15 200bar → 15bar  
 R4 Pressure Regulator for Argon BS300/01 15bar → 10-100 mbar  
 R5 Pressure Regulator for Argon and Air  
 S1 Air Service Station (Filter, Pressure Regulator)

V1 3/2 Pneumatic Valve  
 V2 Shut Off Valve for Air Motor of Piston Pump  
 V3, NORDSON A7A Ball Tip Valve (air actuated)  
 V4 Screw down valve  
 V5 Pneumatic valve / non return  
 V6 Screw down valve  
 V7 Mixing valve  
 V8 Three way valve  
 V9 One way valve  
 SRV1 Safety Relief Valve 4.1 bar  
 SRV2,SRV3 Safety Relief Valve “Nupro” 0,2-3bar (calibrated to 0,2bar)  
 X1 Reed Relais 5V

*Tube and hose types / Medium*

A... 4x6mm Rilsan (Polyamide) flexible hose; medium: compressed air  
 B... 5x6mm stainless steel tube; medium: compressed air  
 C... 4x6mm Rilsan (Polyamide) flexible hose; medium: compressed air  
 D... 6x8mm stainless steel tube; medium: mercury (high pressure)  
 E... 2x NORDSON high-pressure hoses, Teflon ¼”, stainless steel nipples and swivel nuts; medium: mercury (high pressure)  
 F... 6x8mm stainless steel tube; medium: compressed air  
 G... ½” plumbing (316 stainless steel); medium: mercury  
 I... 6x8mm stainless steel tube; medium: air  
 L... ½” plumbing (316 stainless steel); medium: mercury  
 M... 4x6mm Rilsan (Polyamide) flexible hose; medium: compressed air

Feedthrough fittings: Gyrolok, stainless steel.



#### 4.2.4 Pumping System

The housing system used for the set up is constituted of a stainless steel box. The main reservoir of mercury and the pump are contained inside. The Hg reservoir is connected to the piston pump by a  $\frac{1}{2}$ " plumbing (316 stainless steel). The pump is fixed on the top of the stainless steel box and sucks mercury directly from the reservoir. The housing includes calibrated safety valves and pressure regulators.

The complex is installed on a trolley in order to facilitate set up movements. The inner part of the housing is illustrated by picture of Figure 4.5 where the reservoir, the piston pump, the pressure regulators and 3/2 pneumatic valve are visible.



*Fig. 4.5: Inner part of the housing*

The pump used during the experiment is a NORDSON 25B (16:1 stainless steel) piston pump (see Fig 4.6). This pump is a single piston double-acting pump powered by compressed air. The pump consists of an air valve, air motor, and hydraulic section. The maximum input pressure to the pump was limited to 4.5 bar. The 16:1 fluid-to-air pressure ratio pump has a capacity of 0.05 l per cycle (one cycle = 2 strokes). The maximum output pressure is 72 bar. The present pump is a stainless steel pump. The pump in this version is suitable for corrosive materials as mercury.

### Theory of operation:

#### *Suction Stroke*

Supply air enters the pump through the air valve. The air valve directs air through the connecting tube to the underside of the air motor piston, causing the piston to rise. Air above the piston is exhausted through the air valve and muffler. The piston pulls the hydraulic plunger up with it. The pressure ball check closes and the siphon ball check opens, allowing material to flow into the hydraulic section. The material above the pressure ball check is forced out of the pump. As the piston reaches the top of its stroke, the shifting mechanism is activated, shifting the spool inside the air valve, so that supply air is directed to the top of the piston and air below the piston is exhausted.

#### *Pressure Stroke*

Air above the air motor piston pushes the piston and hydraulic plunger down. The siphon ball check closes and the pressure ball check opens. Material below the pressure ball check is forced up through the plunger and out the pressure housing outlet fitting. Figure 4.5 illustrate function scheme of the Nordson 25B pump.

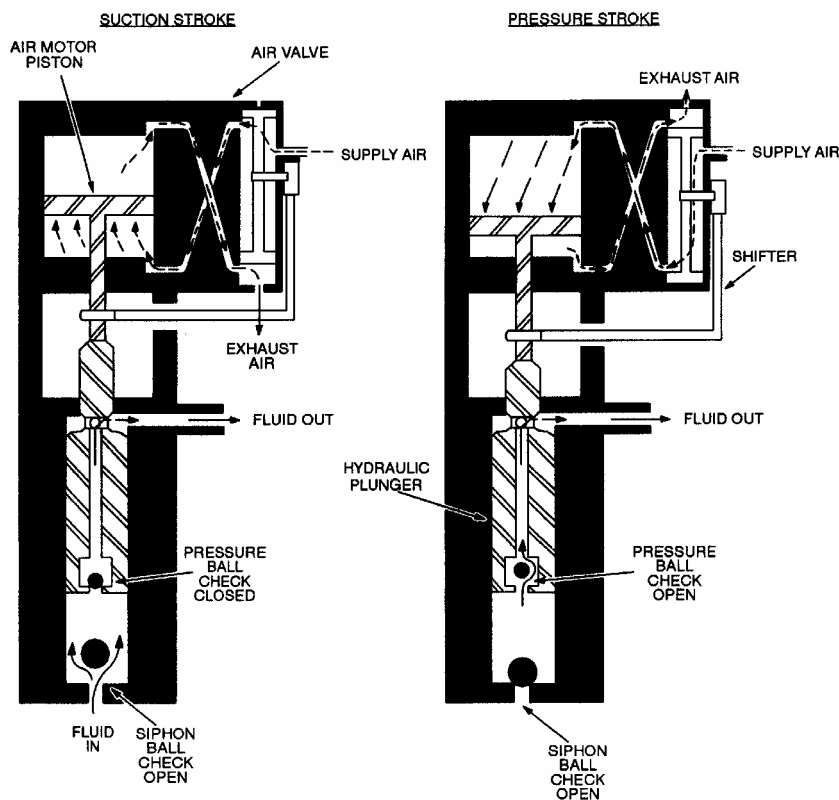


*Fig. 4.6: Nordson 25B pump operation schematic*

The inlet of the pump is connected to the compressed air supply that provides the flux necessary to action the pump. The air supply is connected to the electro-pneumatic valve V1 that triggers the pump and the ball tip valve V3, explained in Section 4.2.5. The electro-pneumatic valve is triggered by the pulse generator that sets the opening signal of both devices. The outlet of the pump is connected to two 6x8mm stainless steel flexible tubes for high- pressure purposes. Through these hoses mercury is directed towards the ball tip valve.

#### 4.2.5 Jet Chamber

The Nordson A7A ball tip valve (see Fig.4.7) is made for airless painting applications. This valve is an air-actuated valve (2.75-8.27 bar) and provides a response time of under 10 ms. The maximum fluid pressure applicable is 117 bar for the standard model. Dimension of the valve are reported in Table 4.1

**Tab 4.1: Nordson A7A valve dimensions**

<i>Specifications</i>	<i>Value</i>
Height	89 mm
Length	89 mm
Width	89 mm
Weight	0.45 kg

When the valve is to be triggered, air enters at the air inlet. This air lifts the piston assembly and allows the packing cartridge and the needle to rise. The fluid to be sprayed, entering at the fluid inlet, may then pass through the opening in the seat to the nozzle. When the air pressure is removed, the needle returns to the seat and stops the flow of the liquid.



**Fig. 4.7: Nordson A7A ball tip valve. High-pressure pipes connections (sides) and nozzle connection (bottom part)**

The ball tip valve is connected to the nozzle and screwed to the experimental chamber. The nozzle used in this study consists of a stainless steel 4.4 mm diameter tube. The shape of the nozzle is important in order to produce stable non-turbulent jets. Two positions of the nozzle are foreseen: a vertical injection position and a 6° tilted position in order to simulate the injection of the jet inside the neutrino factory solenoid. The tube has been designed with two bends. These bends permit to keep the valve position vertical and parallel to the field lines. The ball tip valve and the nozzle are fixed on the experimental chamber. The mercury jet is injected by the nozzle inside this component of the set up. It consists of a stainless steel frame with two Plexiglas plates mounted on each side. Seal is guaranteed by two o-rings inserted in between the frame and the Plexiglas plate. The so build experimental chamber system is perfectly tight. Three threaded holes are present in the chamber; two of them are used to install the nozzle and the valve and the third to evacuate mercury from the chamber when it is filled. The axis of the first of the two threaded holes is coaxial with the chamber axis while the second is 6° tilted. The third hole is situated in the bottom part of the chamber and is used to connect the one-way valve for mercury recovery system. On both sides of the frame, two rails have been machined. On the two rails two mirror holders have been fixed making the mirrors form an angle of 90° among themselves. The chamber is illustrated in Figure 4.8 with all its components.

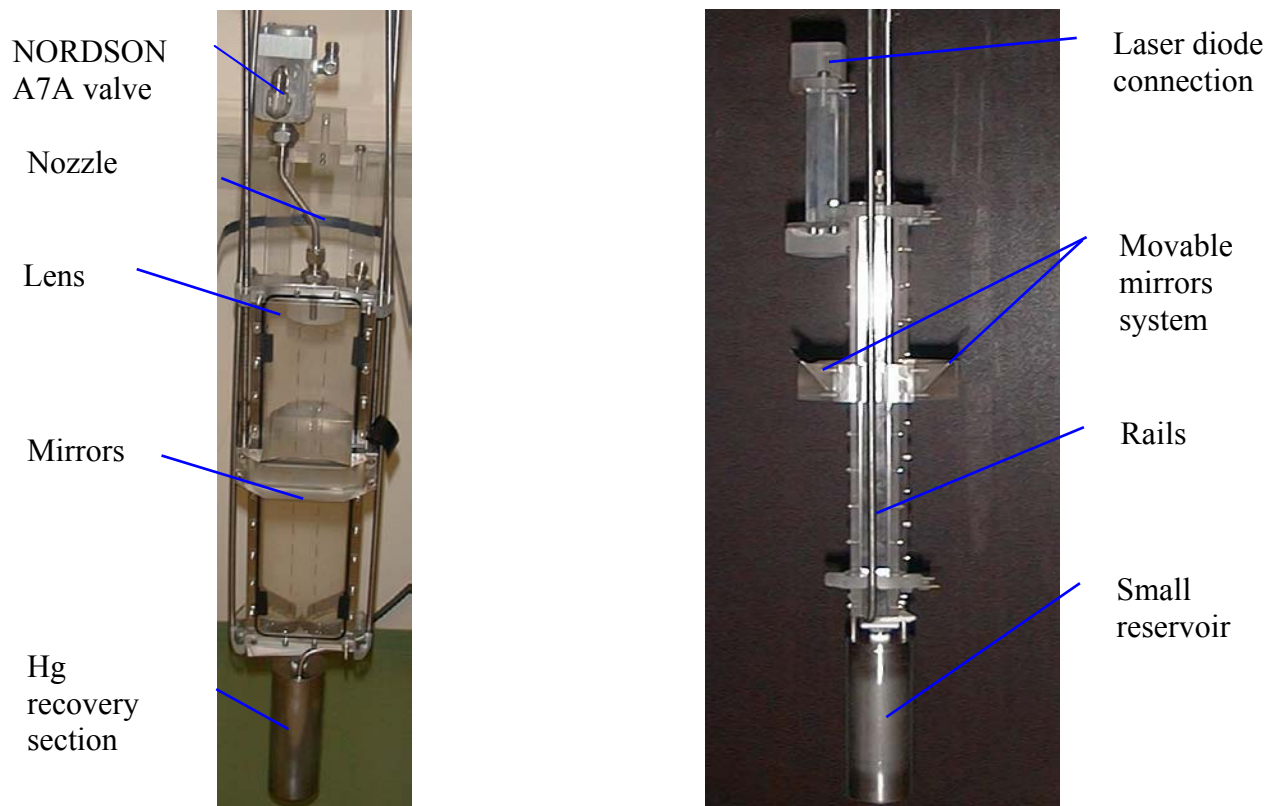


**Fig. 4.8: Jet chamber frontal view (left) and side view (right): the components**

A transparent plastic foil has been applied on the Plexiglas. On the foil a dashed line path was drawn. The path is composed of two series of 10mm vertical lines spaced of 10mm. The distance among the lines is 20mm. The path permits to have references on the recorded images. Moreover, the path is centered respect to the nozzle exit and specifies the ideal path to be followed by the jet in absence of magnetic interaction. Such information is necessary to calibrate the recticle of the camera analysis program as well.

The chamber could be filled with argon at atmospheric pressure or put under vacuum. The choice of a noble gas as argon avoids mercury oxidation. The experimental chamber was inserted inside a stainless steel cylinder as a double confinement for safety reasons.

#### 4.2.6 Acquisition system and optics

The acquisition system comprehends a high-speed camera Olympus Encore MAC connected to dedicated PC. The critical issue concerning the recording system consisted in the placement of the phenomenon to be filmed.

As mentioned the injection of the mercury jet was performed inside the magnet bore where the experimental chamber was inserted. For capturing images inside the 130 mm magnet bore, a chain of mirrors reflected the images outside the bore towards the camera. A laser source, as will be discussed later, provided the necessary light for filming the events inside the bore. In Figure 4.9 is schematically represented the concept mirror chain and laser light path towards the camera.

The jet may be filmed on its whole path thanks to moving mirrors mounted on the experimental chamber. By changing their height, different parts of the chamber, and consecutively of the jet, may be filmed.

As represented in Figure 4.5 below, the light source projects parallel to the magnet axis a light beam towards the first of the mirrors of the mirrors chain. The light is reflected by  $90^\circ$ , traverses the experimental chamber and hits the second mirror. The image is then reflected towards the third mirror out of the bore, sent to the camera lenses and recorded.

As mentioned above, a laser light source was installed on the experimental chamber. The laser beam was directed towards the first mirror of the chain through a lens system. The optic system is composed of two lenses and a support for the fiber optics. The aim of the first lens of the suite is to de-focus the laser light towards the second lens and to produce a parallel light beam and of a diameter sufficient for observing a region of the events as much extended as possible. Passing through the lens suite a cylindrical light beam of 35 mm diameter is directed towards the first mirror of the mirror chain.

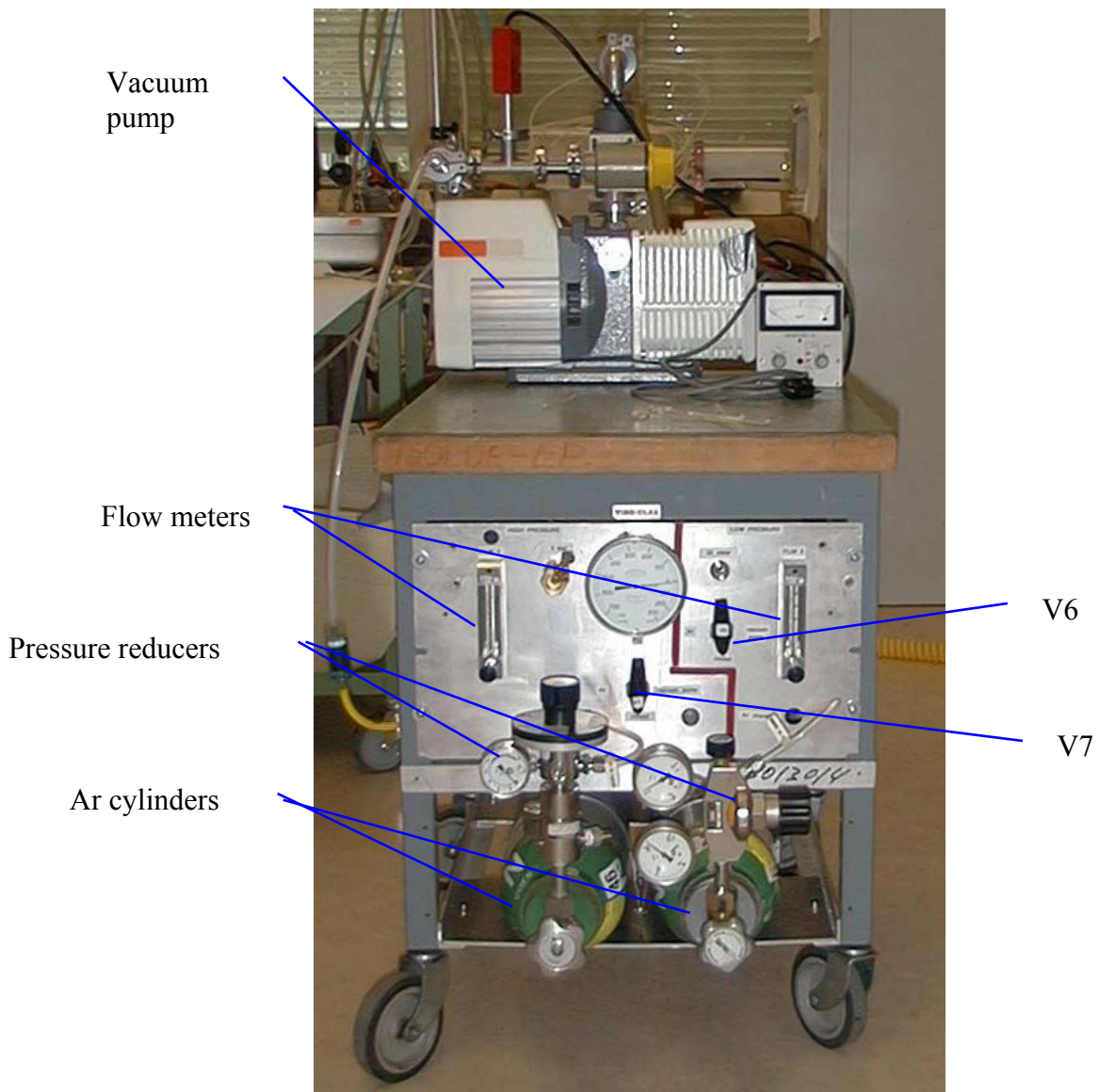


**Fig. 4.11: Hg recovery system; front side view, components**

Acting on valve V6 the experimental chamber may be filled with argon or put under vacuum conditions. The flux is regulated and controlled with the second of the two flow meters. The safety measures taken for the recovery system consisted in testing the small reservoir and its pipe system with an overpressure of 5bar.

### 4.3 Performance at GHMFL

The test consisted of 34 events over 3 days. Jet pulses have been carried out in vacuum conditions. The optics permitted to observe an area of 4 cm diameter surface movable along 20 cm on the field axis.

Early test have been carried out with magnetic field values from 0 T up to 19.3 T and the last shots with inversed polarity from  $-4.9\text{T}$  up to  $-12\text{T}$ . A first set of shots has been performed with no field in order to test the whole system and to take reference positions.

The jet behavior was monitored with the high-speed camera at 8000 fps record rate. Shadows of the jet intercepting the parallel beam have been recorded.

The test consisted in 34 recorded events. Three kinds of events have been recorded: 7 jets with no magnetic field, and 27 jets with both polarity of the magnetic field. The compiled logbook (reported in appendix 3 Tab 2) includes, for each event, the field value, the mirrors' position, the pressure applied to the pump, average speed values and angle of jet displacement.

### 4.4 Analysis

Events' images have been analyzed exploiting the technique used for the previous experiment of "thimble" test. In order to estimate jet displacement along its flight, the left side of the dashed path has been taken as a reference. For a first approximation, maximum and minimum distances ( $D_{\max}$  and  $D_{\min}$  values on the logbook) have been recorded. From the so obtained value the distance  $d = 10$  mm has been subtracted. The resulting value is the position of the jet referred to the horizontal center of the nozzle. The average value  $P_0$ :

$$P_0 = \frac{D_{\max} + D_{\min}}{2}$$

provides the average jet position referred to the height of mirrors, where these measurements have been taken. Mercury jet displacement is plotted in Figure 4.12 as a function of the B field.

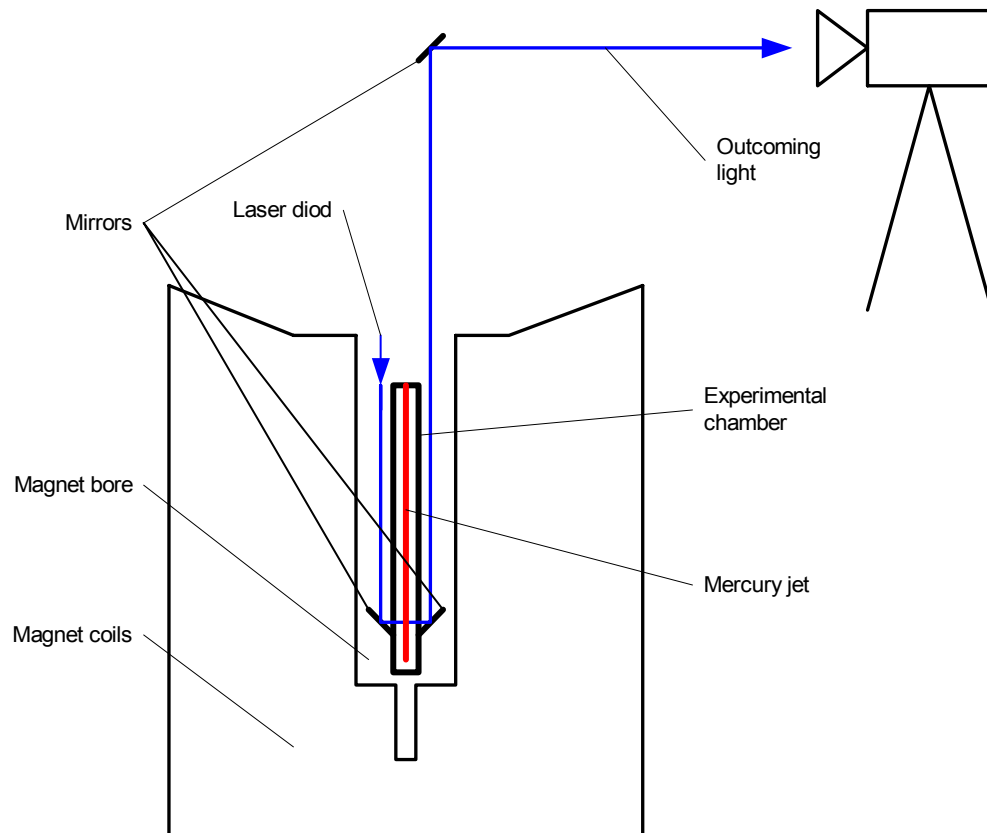


*Fig. 4.9: Image capturing scheme, total path length of light  $\sim 10\text{m}$ . Camera's CCD size  $1\text{cm}^2$*

#### 4.2.7 Mercury recovery system

The one-way valve, which is situated in the bottom part of the experimental chamber, is connected to a small cylindrical reservoir for collecting mercury after the shots. The volume of the recipient is  $250\text{ cm}^3$ . In order to empty the experimental chamber after the shots, a hydraulic circuit has been added to the set up. As illustrated in figure 4.10 the small reservoir is connected to the mercury recovery system through the pipe P.



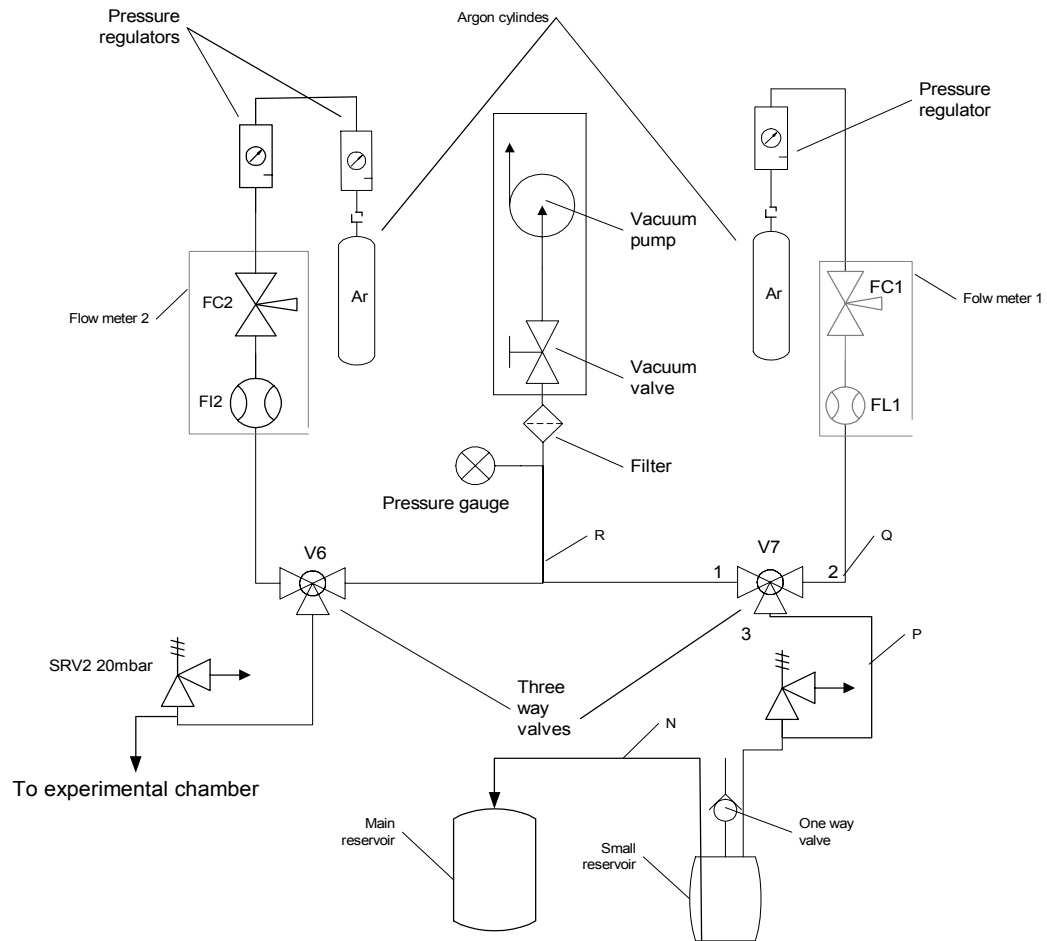


**Fig. 4.10: Flow chart of mercury recovery system**

The recovery system is split in two parts. It consists of a trolley on which the set up is installed. The same apparatus is used for flowing argon and to put vacuum, both in the experimental chamber and in the small reservoir. These two operating modes may be selected by acting on valve V6 (for the chamber) and V7 (for the reservoir).

Once the bottom part of the experimental chamber is full of mercury an under-pressure of 1 bar is applied connecting the vacuum pump to pipe P by selecting position 1 of valve V7. This step facilitates the opening of the one-way valve and makes mercury flow out of the chamber. When the small reservoir is filled with mercury, valve V7 is switched over position 2 and an over-pressure is applied in the small reservoir by flushing argon. Flow is controlled by a stainless steel flow meter, which absolves both the functions of regulating and measuring the flux. Mercury may so stream through the pipes into the main reservoir and be re-circulated. Pictures of the hydraulic circuit and of the trolley are shown in Figures 4.11.

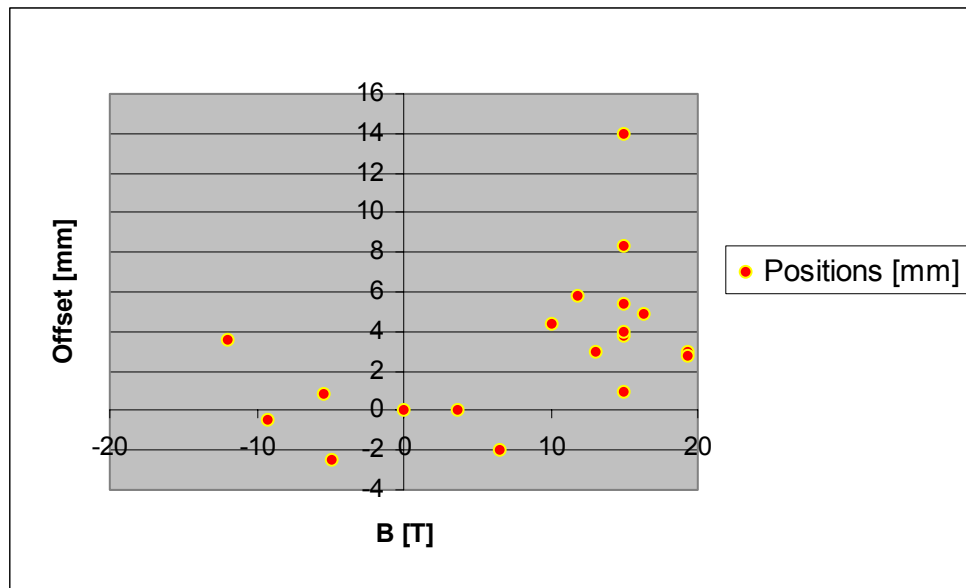


*Fig. 4.12: Mercury jet offset as a function of B field*

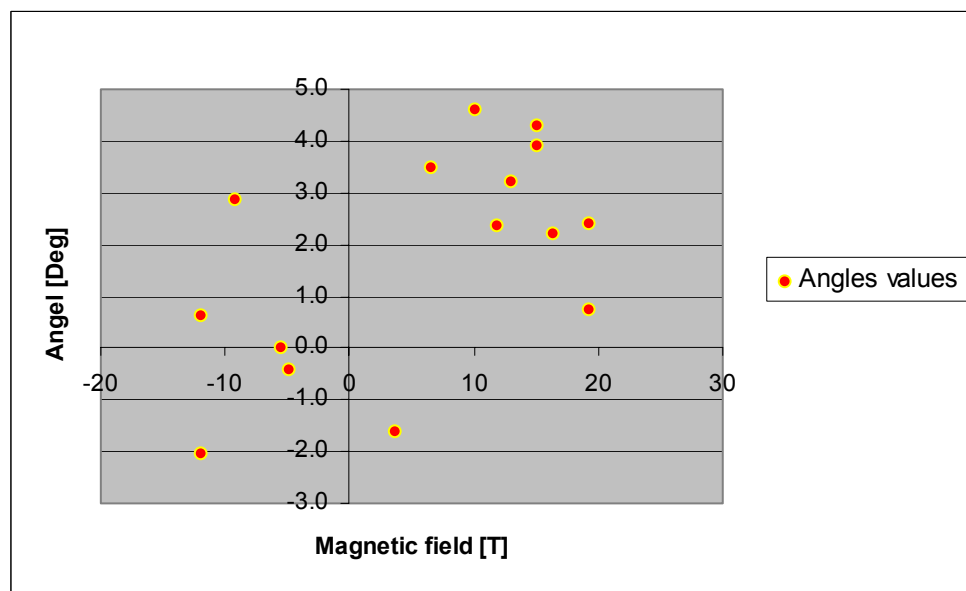


*Fig. 4.13: Angles of jet deviation as a function of applied field*

The height  $h$  written in the logbook indicates the position of the mirrors referring to their lowest position. The lowest position of the mirrors is at a distance of 23.1 cm from the nozzle. The flight path  $l$  of the jet from the distance then calculates as the difference of the lowest

position and the height  $h$ . The deflection angle  $\alpha$  (Degree) of the jet caused by the magnetic field is defined as:

$$\alpha = a \tan\left(\frac{P_0}{l}\right)$$

Resulting values for events with the same configuration plotted as a function of the applied magnetic field are represented in Figure 4.13.

The movable mirrors system permitted to follow the jet along its path. The offset of the jet recorded by means of a vertical scan of the mirrors is represented by the sequence of pictures of Figure 4.14.

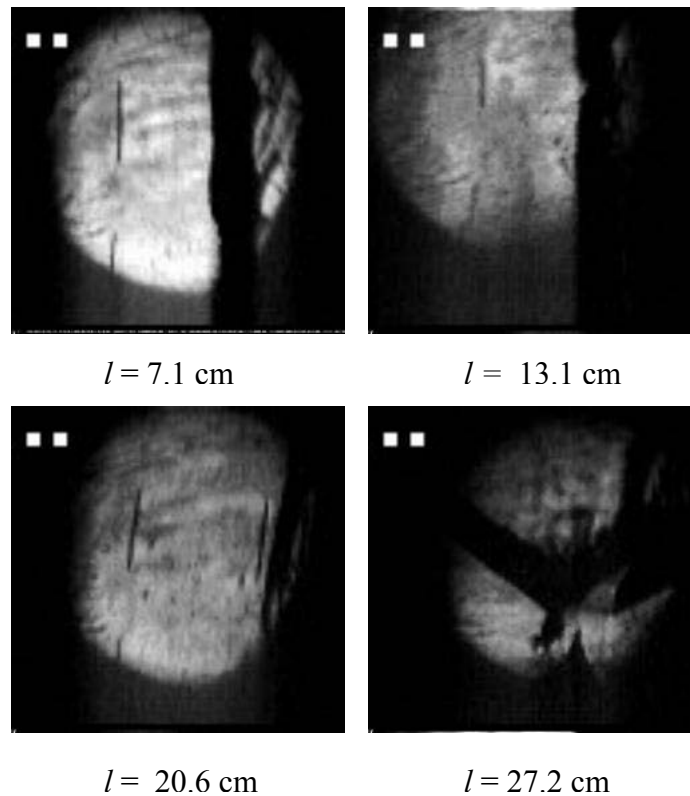


**Fig. 4.14: Jet path with 15T field: distances  $l$  are reported from nozzle exit. For  $l=27.2\text{cm}$  (bottom part of the chamber) the stainless steel collectors and the recuperation chamber are visible**

Applying a magnetic field, jet position tends to move on one side of the image following an inclined path. The trend of jet to move on one side of the chamber is a function of the field value as well. Images of figure 4.15 represent this dependence.

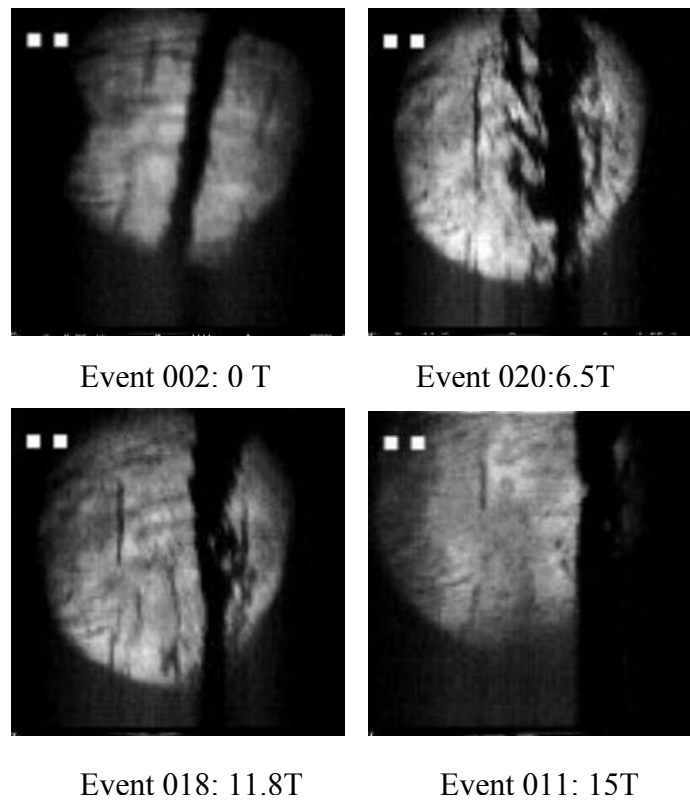


***Fig. 4.15: Jet displacement as a function of increasing field value: 0T, 6.5T, 11.8T, 15T. Jet is visibly displaced***

Jet speed analysis was a parameter under investigation as well. This parameter has been measured with the software run by the high-speed camera program. Measurements of jets with and without magnetic field are available. Figure 4.16 shows the dependence of velocities on the magnetic field. The trend line point out the decreasing speed of the jets when stressed by the magnetic field.

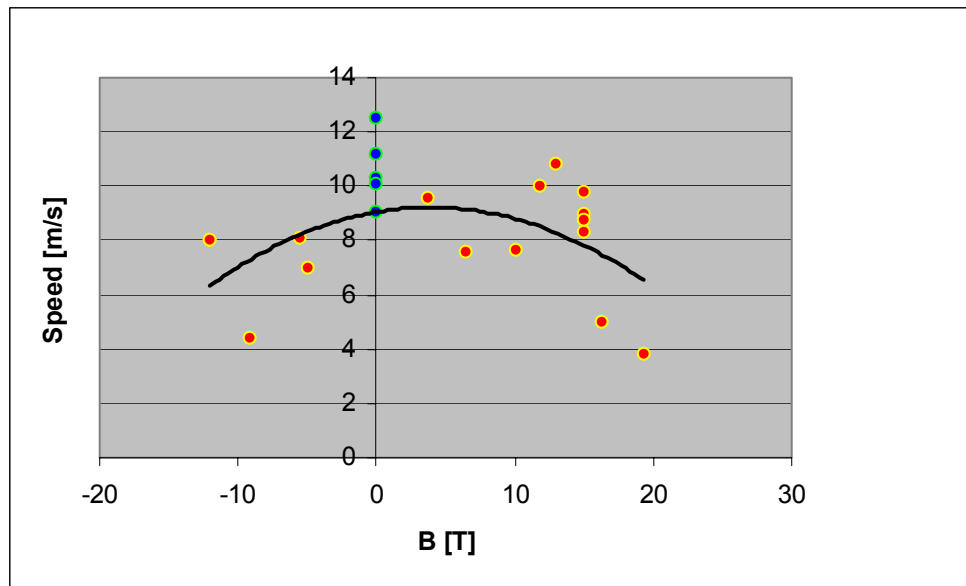


*Fig. 4.16: The dependence of velocities values from the applied field (both polarities) is compared to velocities with 0T field. Constant pressure value  $p=4$  bar*

Numbers of first and last frames in which mercury jet shadow was visible have been inserted in the logbook and plotted as illustrated in Figure 4.17 below.

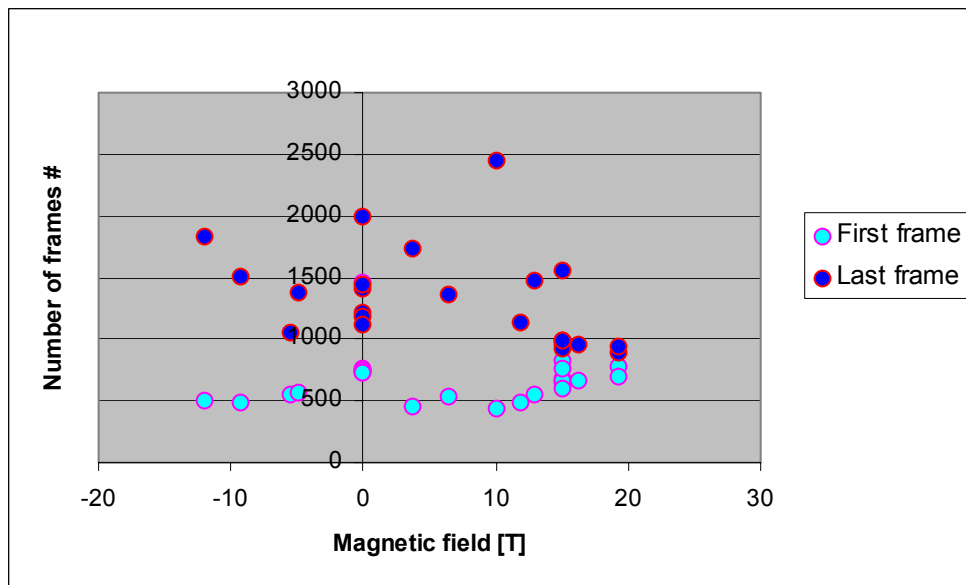


*Fig. 4.17: Scanning the diagram with vertical lines duration of the events is visible*

Jet duration is calculated in milliseconds by subtracting the last frame and first frame values and multiplying the so obtained value for the time length between two pictures (0.125 ms). Results are illustrated in Figure 4.18.

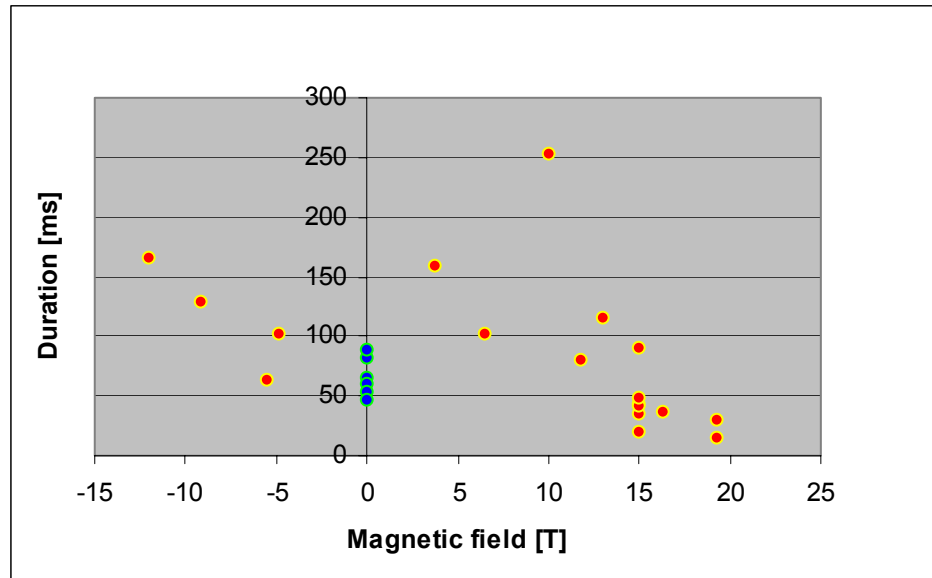


*Fig. 4.18: Blue dots are related to no field jet length while red dots represent jet duration as a function of applied field*

## 4.5 Conclusions and next tests

The data sets recorded during the experiment in September 2002 contains qualitative information to characterize the case of collinear injection, where the nozzle is out of the homogeneous field section and underlies challenging task of injecting a molten metal target through a high magnetic field gradient.

Recorded events of jet injection in the field gradient clearly demonstrated deflection and disruption of the Hg-jet pulsed through the cylindrical nozzle (see Figure 4.19). The mercury jet experienced a deflection from the axis of the magnet bore increasing with the field strength. A major reduction of the jet speed was measured, however analysis is underway to determine its cause. Possible causes under investigation are friction of droplets on the Plexiglas windows, MHD effects in the injection system (pipes [43], valve and nozzle) and during the free flight of the jet.

It is not possible to determine whether jet offset is two-dimensional or not and consequently if mercury slips on the windows or not. In case of a contact with the windows jet shape could look like a global jet disruption similar to those caused by MHD effect. MHD effect might modify flow conditions in the nozzle section as flowing mercury crosses almost

perpendicular field's lines. MHD effect on the valve's needle could compromise the right opening time of the valve. This could influence results related to global jet duration. The issue has to be investigated since the valve is positioned parallel to the magnetic field lines and no MHD effect should act on mercury inside the valve. For given parameters each shot corresponded to an ejected mercury volume of  $\sim 65 \text{ cm}^3$ . The global tendency of inverse proportionality between jet duration and magnetic field could be influenced by a shorter opening time of the ball tip valve. One possible implementation of the set up could consist in moving the valve outside the magnetic field.

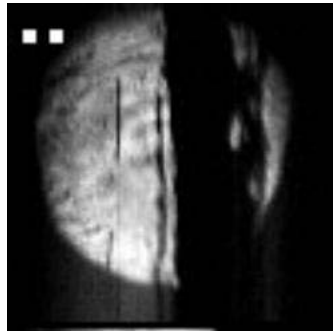


*Fig. 4.19: High intensity magnetic field disrupt pulsed jet: effect of a 19.3T field over a mercury jet.*

During the test two technical difficulties were encountered. The movement induced by the reacting forces of the nozzle induced a displacement of the parallel laser beam away from the camera objective. The problem thwarted filming as for the main part of its permanence in the chamber the jet was not visible. The trouble found a solution by the insertion of a wedge.

The second reported trouble consisted in the miss of matching between the magnet bottom bore and the small reservoir dimensions. The diameter of the mercury reservoir was designed for a 55 mm bore outlet while the corresponding hole was 50 mm diameter. Thus the internal set up was positioned 25 cm off the center of the bore. Cause the impossibility of modifying the set up in-situ the whole experiment was carried out in this configuration. Modifying the stainless steel confinement could have compromised the perfect seal of the system, which demonstrated to be perfect.

A new series of experiment is foreseen in GHMFL. Tests with  $6^\circ$  injection angle and 20T field are foreseen.

New components have already been introduced in order to obviate a find want. Stainless steel cones will be fixed to the top part of the experimental chamber in order to improve coupling between the inner set up and the stainless steel external confinement. Movements of the internal set up respect the external confinement will be avoid. Implementation of data reliability will be entrusted to installation of two pressure gauges DYTRAN 2300V5(see Fig. 3.20).



*Fig. 4.20: Dytran 2300V5 pressure gauge*

Sensors have a frequency response of 500 kHz and will record pressure values at pump outlet and before the ball tip valve. Dynamic pressure trend will be recorded each shot in order to evaluate pressure fluctuation inside the stainless steel pipe and back reflected pressure waves due to water hammer after the fast closing of the valve.



## Chapter 5

# Study of Homogeneity on Experimental Amalgams for Mercury Waste Consolidation

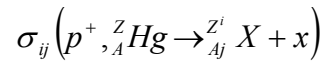
### 5.1 Radioactivity

A particle shot into a medium may have electromagnetic or nuclear interaction. The nuclear interaction follows an exponential law involving the nuclear interaction length  $\lambda_{nuc}$ .

$$-d N_p \div N_p \lambda_{nuc}$$

where  $N_p$  is the number of incoming protons that interact after a  $\lambda_{nuc}$  distance and  $-d N_p$  is the differential value if

This value is expressed in units of  $\text{g/cm}^2$  and represents the distance that a particle may cover before having nuclear interaction with the medium.  $\lambda$  is related to the sum of all reactions [44]:



Where  $\sigma_{ij}$  is the cross section value. The example above illustrates the interaction with an incoming proton  $p$  and a mercury atom. The result of the interaction is an isotope of any element  $X$  (included mercury) with charge  $Z'$  and number of protons  $A_j$ .

The function has an exponential ( $y = e^{-kx}$ ) trend. From incident particle ( $p^+$ ) and nuclei (Hg) interaction new particles born. Radioisotopes of the medium and radioisotopes of other elements as well are produced during this interaction.

Concerning the survival probability of a particle of mass  $M$ , mean proper lifetime  $\tau$  and momentum ( $E, p$ ) the probability that it lives for a time  $t_0$  or greater before decaying is given by [45]:

$$P(t_0) = e^{-\frac{M t_0 \Gamma}{E}}$$

This value is needed for estimating time necessary for short life particle to decay. To this family of particles belongs the much higher activity level.

This process is true in “thimble” test as well as in the magnetic horn where mercury becomes radioactive. At CERN all activities concerning handling radioactivity are treated accordingly to “ALARA” (As Low As Reasonably Achievable) standards. To each radioactive waste corresponds a priority for treating. For radioactive mercury produced in “thimble” test experiment priority for treating it was low. For this reason it has been possible to wait until the radioisotopes decayed of five order of magnitude their half-life time. Half-live time is the time of the live of a radioisotope during which it loses half of its activity. The law of activity decay has a logarithmic trend:

$$A = n_a \cdot \lambda = n_a \cdot \frac{\ln 2}{T_{1/2}}.$$

For this reason it is not useful to wait longer than  $10 T_{1/2}$  (half-live time) since the most radioactive isotopes have shorter live. Only isotopes  $^{194}\text{Hg}$  and  $^{203}\text{Hg}$  have live-time longer than  $10 T_{1/2}$  and survive.

## 5.2 Aims of the study and motivations

In a neutrino factory based on molten metal target and in particular based on a liquid mercury target, the problem of handling radioactive mercury produced must be investigated. According to foreseen neutrino production a few tons of mercury will be activated. Idea is to separate highly activated mercury from the target circulation by distillation. For safety reasons storage of the radioactive mercury in solid state is more convenient.

Specifically for “thimble” experiment an agreement with Swiss authorities imposes to store radioactive waste from ISOLDE experiments in form of solid amalgam. This study aims therefore to develop a procedure and acquire the knowledge for solidifying radioactive mercury in solid amalgam form.

Among proposed solutions for this topic the one of exploiting technology coming from medical field has been chosen for first investigation on the problem. The field of medicine taken in consideration is odontology. Actually within this branch of medicine no radioactive mercury is involved, but as there is no difference in treating stable or radioactive mercury, it is convenient and possible to exploit technology that involves stable mercury as in dental field.

When treating dental decays, dentists use silver dental amalgams to fill teeth. Compositions for direct filling restorations usually consist of silver, tin, copper and zinc alloy amalgams. Amalgams are produced by combining mercury with alloy particles by a process referred to as trituration.

High-speed mechanical amalgamators mix the materials in a matter of seconds. As soon as alloy powder and mercury come in mutual contact, they exothermically react and the final alloy starts to solidify. This process can be accelerated by shaking the amalgam. The deformable amalgam mass after trituration is inserted in the teeth’s cavity. Dental amalgam is

essentially a silver-mercury alloy and in minor concentrations there are also metallic composites of intermetallic compounds of Ag-Sn, Ag-Hg, Sn-Hg and Cu-Sn. The mixture hardens by a diffusion reaction in which liquid mercury is replaced by solid mercury compounds such as  $\text{Ag}_2\text{Hg}_3$  and  $\text{Sn}_7\text{Hg}$ . Dental amalgams typically contains from 40% up to 50% of mercury.

### 5.3 Equipment

The so proposed idea of using silver dental amalgam for entrapping radioactive mercury in a solid matrix needed to be investigated by planning a series of tests and metallurgical investigation. For this purpose a laboratory containing all equipment needed for preparing amalgams was set up. This equipment is quite similar to the dentist studio's one with some differences due to the diversity of purposes.

#### 5.3.1 The capsule

Ingredients of amalgam used by dentists is commonly sold in capsules ready to be shaken and used. Inside these capsules, components for amalgam are already dosed in the right amount. For our purposes it was not possible to use these capsule for different reasons. In fact, for getting rid of radioactive mercury produced in our experiment, we needed a much higher flexibility in preparing the samples.

By using ready-made capsule and by extracting mercury contained in them for substituting it with the radioactive one, it was first of all the fixed amount of amalgam we could produce in one test. In addition, it was difficult to achieve the requested precision in respecting the right proportions among powder and mercury since mercury is more difficult to be precisely weighted than powder.

One more feature that made it impossible using ready-made capsules consists in their structure. Capsules are in fact constituted of two parts embedded and a small thin plastic pocket stuck in one of the two sides used with the aim of keeping the alloy powder separated from mercury. This small plastic bag is hermetically closed and not refillable. When the capsule is shaken the plastic bag, hit by powder mass, breaks and mercury mixed with powder. Moreover no empty capsules for dental purpose are available on the market since it is now forbidden for dentists to prepare amalgams in their medical studios [46].

A capsule was designed and built corresponding to our needs. Capsule had to perfectly simulate behavior of ready-made ones (Figures 5.1, 5.2, 5.3add capsule.dwg). For this purpose a three pieces capsule has been designed (appendix 2.1, components' drawings). The number of three components has been made indispensable in order to separate mercury form powder. Capsule's structure is influenced by the presence of a paper foil, similar to cigarette paper, inserted in between the capsule to keep mercury and powder separated before shaking. The two sides, which are slightly different, are screwed to the central part that is internally threaded in both sides.

The paper foil, cut in a 13 mm diameter circle, is blocked between the central component of the capsule and one of the two side parts as shown in picture 1 of appendix 2. The contact surface between these two components has been projected to be flat in order to guarantee a perfect seal and to avoid paper fold. A conical coupling would compromise this feature.

Concerning the other side of the capsule, coupling among central part and side part is conical to assure a perfect seal and avoid mercury droplets, which could accidentally penetrate in the thin fissure, to spill out of the capsule once it is opened. When the capsule is closed, the internal surface is perfectly smooth and devoid of fissures.

Another shrewdness is concerning the material of the capsule as not every material is fully compatible with mercury. In choosing the material not only compatibility with mercury must be taken in consideration, but material density as well. Such a further restriction is lead by the mixer. This device cannot handle capsules heavier than 6 g. Among materials fully compatible with mercury, as shown in tab. 1 appendix 2, PVC has been chosen first of all for its low density and for its good mechanical properties. Other materials have been considered as well as for example HDPE (High Density Poly Ethylene) with a  $0.96 \text{ g/cm}^3$  density [47]. PVC in fact, is more dense ( $1.37\text{-}1.39 \text{ g/cm}^3$ ), but it is easier to machine. The possibility of easily machine the material is an important choice parameter as capsule's dimensions are small and building it requires high processing precision otherwise not obtainable.

By choosing PVC, and considering a capsule volume of  $2.67 \text{ cm}^3$  capsule's total weight is 3.66 g. It is so possible to fill it with more than two grams of amalgam respecting device's performances.



*Fig. 5.1: Assembled capsule*



*Fig.5.2: Capsule components*

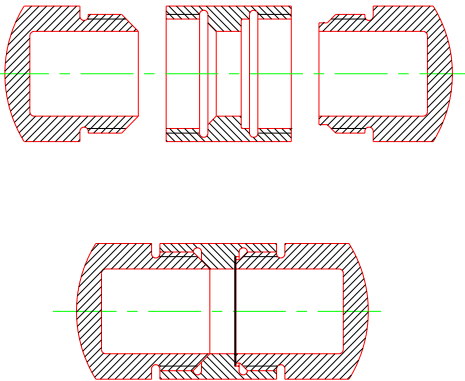


*Fig 5.3: Capsule components: assembling*

**5.3.2 Amalgamator**

In order to triturate amalgam’s components a shaking device for the capsule is needed. An industrial produced amalgamator commonly used by dentists has been purchased.

The 3M EPSE Rotomix<sup>®</sup> has been chosen for its particular mixing principle based on revolving/centrifuging. The device revolves the capsule by two super-positioned rotations. The

first movement of the capsule is around its center perpendicular to the cylindrical symmetric axis. In plane with this movement the capsule is rotated on orbit of 80 mm. This process mixes the powder and the liquid homogeneously. The centrifugal acceleration ( $3600 \text{ m/s}^2$ ) inside the capsule is applied uniformly in all directions. These mixing features permit to achieve a better amalgam of the components. The paste is then centrifuged for 3 seconds to collect it on one side in order to confer the same shape to all samples and to force the air voids out of the material.

### 5.3.3 Precision balance

The last component needed for preparing amalgams was a precision balance necessary to weight the right mixture of amalgam's components. For this purpose an electronic precision balance with 3 decimal digits has been chosen as the quantities supposed to be weighted are in the order of milligrams. The scale pan has been chosen stainless steel made in order to avoid any corrosion risk in case of mercury spills.

## 5.4 Test procedure and samples preparation

A procedure to prepare amalgams has been established (see section.3 appendix 2). All steps have been studied taking in consideration possible hazards concerning mercury's handling.

First tests with no radioactive mercury have been conducted on amalgam samples prepared using powder extracted from ready-made capsules (Valiant<sup>®</sup> from Dentsply) and an old powder, called "our" during the tests, that was available for first tests. Latest tests have been carried out on Dispersalloy<sup>®</sup> powder, the powder chosen to be used in final step with radioactive mercury. The three powders had different compositions (tab.4 appendix 2). All were based on silver, tin and copper alloy but in different proportions with one more component each (Pd for Valiant<sup>®</sup> and Zn for Dispersalloy<sup>®</sup>) but in percentage of  $0.6 \div 1\%$ . Mercury has been added to powder according to data provided by the amalgam supplier.

Several tests have been carried out using "our" powder that was of lacking quality compared with powder extracted from Valiant<sup>®</sup>'s capsules. These tests aimed to find out influence of mixing parameters as shaking time, mercury percentage in the alloy, and centrifugation of samples immediately after trituration process. The logbook can be found in tab.5 of appendix 2) containing all test parameters, description of alloy's look when extracted from the capsule and vapor emission recorded with mercury vapor detector after fixed space times.

The ratio of amalgam powder and mercury has been varied as well. This was to determine the precision needed to achieve amalgam samples with negligible different properties. Two samples for each powder have been prepared adding or subtracting 5% of mercury in rapport of the standard amount.

## 5.5 Optical microscope analysis

### 5.5.1 Samples preparation

Amalgam specimens, prepared according to the developed procedure, need to be prepared for optical microscope analysis. For this purpose each amalgam sample must be inserted in a standard rest in order to guarantee an adequate analysis quality. The rest is an epoxy resin cylinder.

Powder is inserted into an apposite oven that heats it up to 170 C and maintains it at this temperature for 20 minutes. The powder melts and solidifies into a hard cylinder with the two basis surfaces perfectly parallels. This allows analyzing the samples in a way that the specimens are perfectly parallel to the microscope stage. Once the rest is ready the sample have to be fixed to it. Two different techniques have been used in fixing the amalgam sample to the epoxy resin rest.

The first, used for samples of series from 1 to 9, consists in fixing amalgam samples to the epoxy resin rest. Samples are glued on one of the two basis of the epoxy cylinder. Amalgam sample is then smoothed by wet-grinding.

The second technique, used for specimens of series 10 and 11, consists in drilling a hole of 4 mm diameter and 5 mm depth. The hole is filled with the amalgam extracted from the capsule immediately after shaking and pressed with a pestle in order to simulate technique used by dentists when filling a tooth with amalgam. Surface smoothness is achieved by wet-grinding. Each sample is wet-grinded using grinding-wheel of decreasing granulometry starting from a 180 grain per squared centimeter grinding-wheel granulometry then passing through 240, 600, and 1200.

After this treatment the surface must be polished using a grinding-wheel covered with a woolen-cloth sprinkled with a diamond suspension first of 3  $\mu\text{m}$  and then of 1  $\mu\text{m}$ . This last step of abrasion is needed for polishing completely the surface that is supposed to be analyzed. After the polishing process, the so prepared specimens are treated for a time length of 30 seconds with ultra-sounds putting them into a glass contained in a water pool. This final operation removes all possible residual of epoxy resin and amalgam. After being dried the specimen are ready to be analyzed. Samples exploration and codification

The analysis was conduced using an optical microscope with 50x, 100x, 200x, 500x, 1000x, 1500x enlargements connected to a dedicated computer that allows fully analyzing and recording images.

Each sample's surface has been first fully explored zooming it using a lens enlargement of 50 times in order to have a first global idea of amalgam structure including air voids presence.

Samples have been successively watched increasing lens enlargement and choosing a 500 times and 1000 times enlargement for recording images. For each sample a picture of one of the most representative areas of sample's surface have been taken and recorded (see Figures 5.1-5).

These areas have been chosen because of the possibility of summarizing in them all the characteristics elements present in the sample.

Recorded images have been codified according to a nomenclature in which the first two numbers refers to sample number and the sequent refers to utilized enlargement. In pictures of particular interest picture has been taken twice but increasing enlargement to 1500 times to better estimate observed peculiarities. Whenever a picture of the same sample was taken twice conserving the same enlargement it was marked with a letter after the enlargement number in order to distinguish it from the previous one.

### 5.5.2 Results

A first observation with optical microscope with a magnification of 50 times, carried out on samples belonging to series from one to ten, pointed out, the presence of a considerable number of air voids into the alloy matrix.

As this feature has a negative influence on alloy's properties and makes difficult to carry out further tests as micro hardness, a second set of tests has been carried out pressing the alloy into holes drilled in the epoxy resin rest.

This test demonstrated that air voids presence is reduced not only by centrifugation of the sample during preparation, but also by pressing amalgam into a cavity. By using this technique, exploiting what dentists usually do, is immediately appreciable the improvement in air voids elimination as shown from the Figures 5.4, 5.5 and 5.6 below.

A second feature which appears slightly different among the samples is how the alloy microstructure looks like. They present round structures in a matrix with two types of porosity: irregular pores in the matrix and round pores in the middle of some of the structures (possible respective origins: lack of compaction during amalgamation and pores previously present in powder used for amalgamation). Round structures size varies from  $\text{Ø}50\mu\text{m}$  downwards

Most probably these rounded structures correspond to powder particles prior to amalgamation since dimension and shape of those spots seems to be related to powder's quality. Spot dimension is much higher in samples prepared using the first powder, which I called "our", then in other samples containing Valiant<sup>®</sup> or Dispersalloy<sup>®</sup> powder.



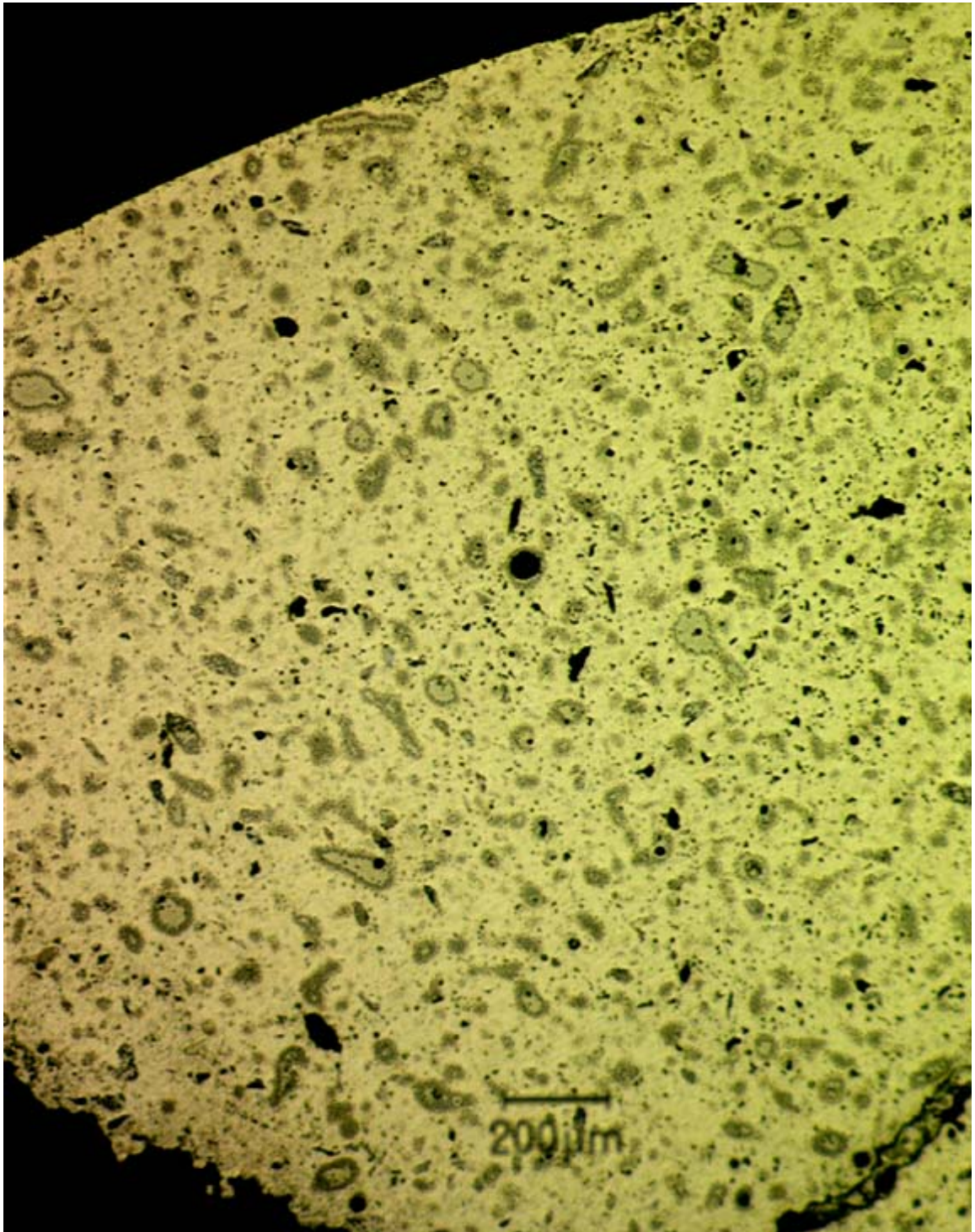


*Fig. 5.4: Sample 5.2, 50 times magnification*



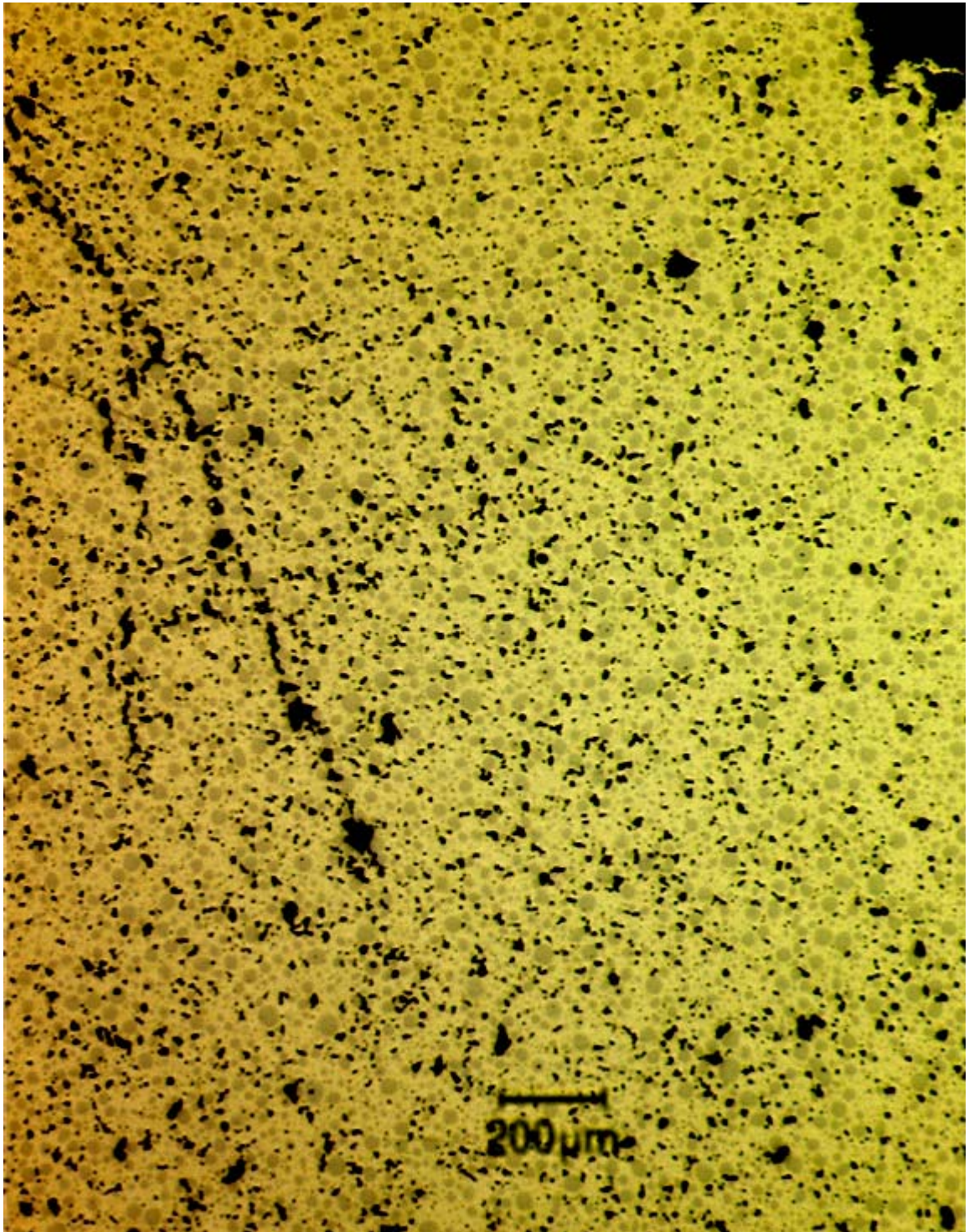


*Fig 5.5: Sample 9.3, 50 times magnification*



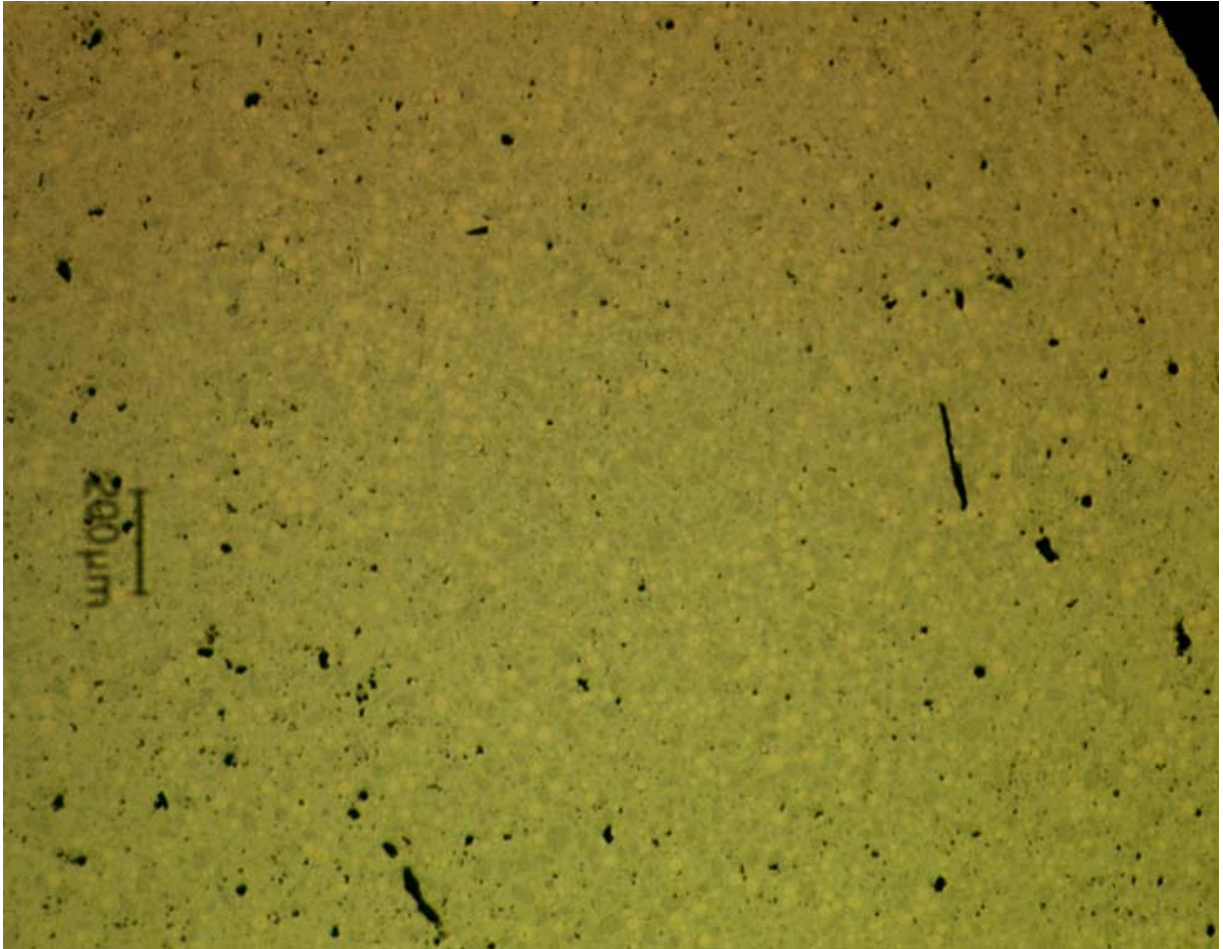


*Fig 5.6: Sample 11.1, 50 times magnification*

Analysis with a higher magnification leads to discover one more peculiar feature that differences the two powders. Spots contain, on their external surface, small bubbles that at a first look seem to be small mercury droplets. This presence is more evident in samples prepared using the old powder as illustrated in Figure 5.7. This feature is less visible in the other samples prepared with Valiant<sup>®</sup> (Fig. 5.8) powder and not visible in Dispersalloy<sup>®</sup> powder.

It is interesting to observe how after polishing once more the sample's surface by wet-grinding those small droplets disappear and reappear after few hours. However considered the small dimension of those droplets, in the order of magnitude of few microns, and the apparently impossibility of their detachment, this feature of the amalgam should not create any possibility of polluting the surrounding environment.

This peculiarity could be due to the fact that "our" powder was old and its elements could have already been partially bound together thwarting bindings formation between the different powder's components and mercury.

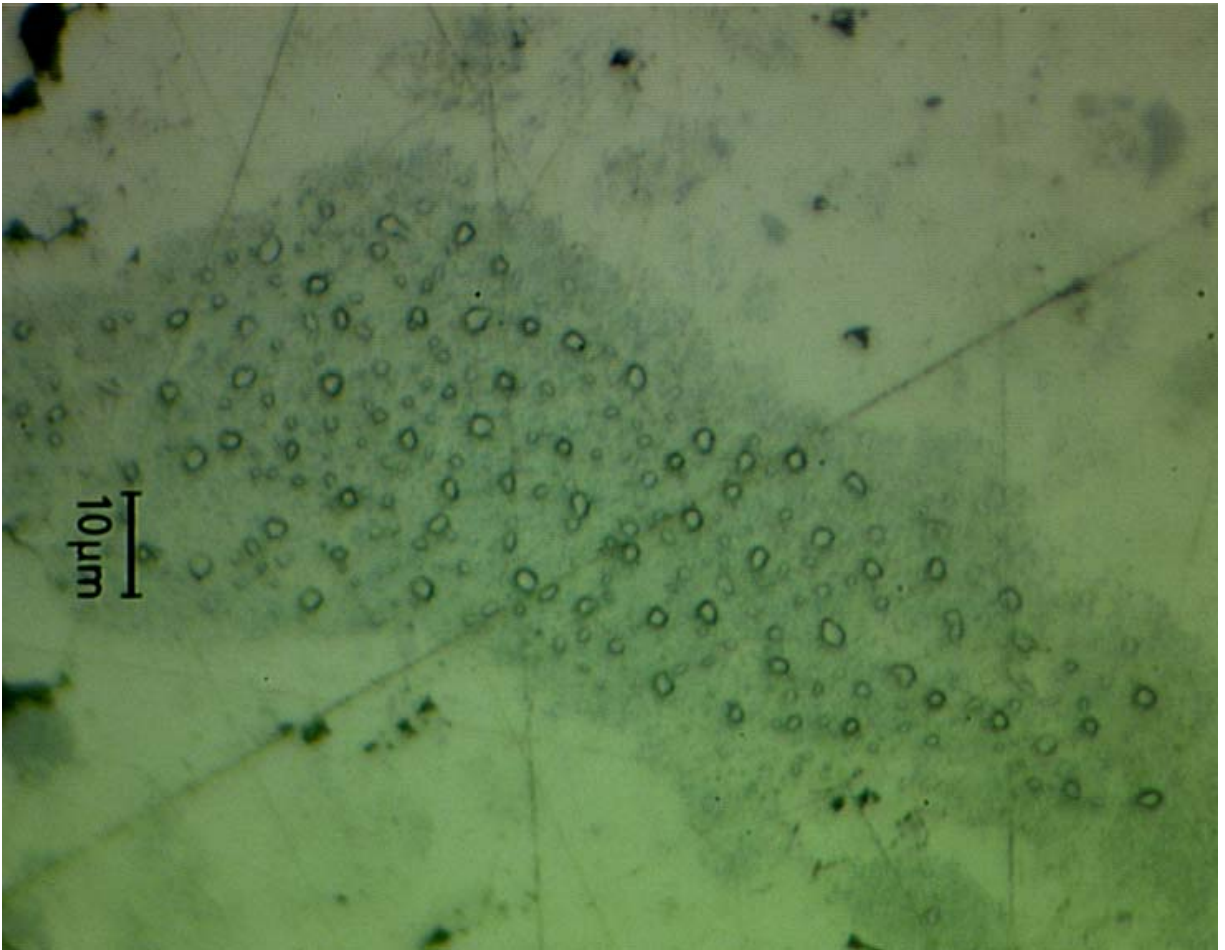


*Fig. 5.7: Sample 5.2, 1000 times magnification*

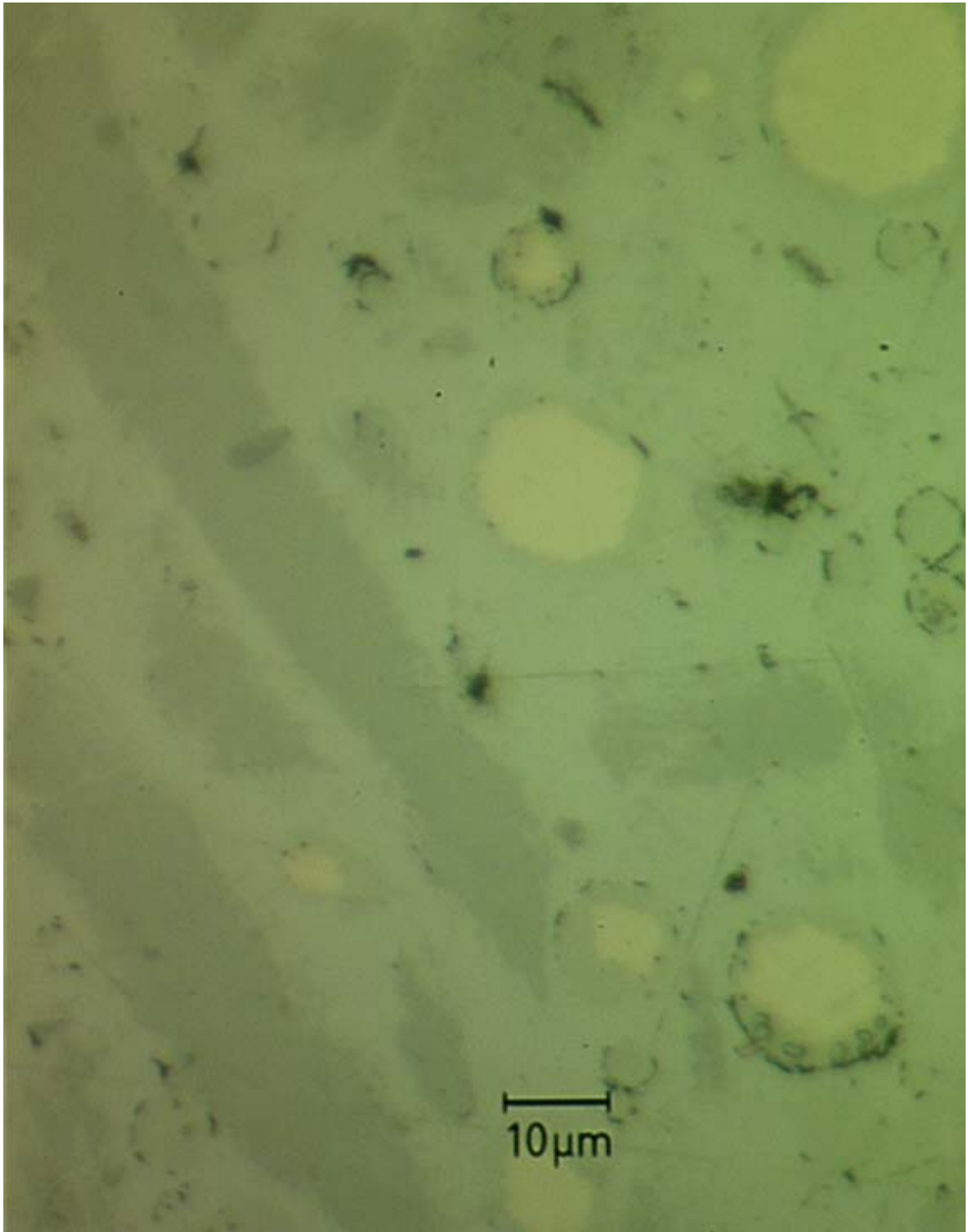


*Fig. 5.8: Sample 10.1, 1000 times magnification; almost no bubbles are visible*

## 5.6 Scanning Electron Microscopy analysis

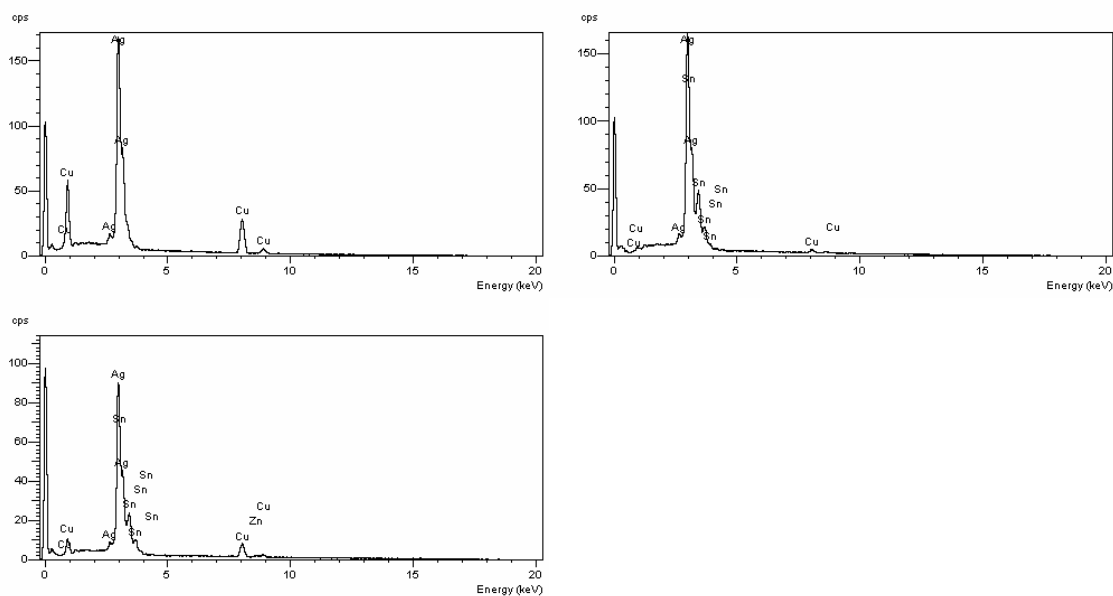
In order to analyze samples, electron microscope focalize an electron beam on the object that has to be analyzed. This energy concentration heats up the analyzed object so by focusing beam's energy on a small region of the sample containing mercury it could vaporize. Electron microscope analysis chamber is maintained in under-pressure conditions during observation. Under-pressure value ( $10^{-7}$  bar) is under mercury's vapor pressure<sup>1</sup> and eventually present mercury droplets could immediately vaporize. This vaporization could lead to microscope damage first and to risk for human health in case of vapor inhalation.

Electron microscope analysis requests two more treatments of the samples. Samples have for this reason been pumped under mercury's vapor pressure for one day in a desiccator in order to permit evaporation of eventually present mercury. Masking of mounting with graphite spray and colloidal paste was successively needed before electron microscope analysis.

Electron microscope investigation has been performed observing sample 10.1 and 11.1 at secondary electron emission (SE) and back-scattered electrons (BSE).

### 5.6.1 Amalgam powder observation

Two types of particles were identified: A) sphere particles of different sizes from  $\text{Ø}50\mu\text{m}$  downwards, textured surface and approximate composition 75Ag-25Cu, B) lather-cut particles from  $50\mu\text{m}$  length downwards and approximate composition 72Ag-25-Sn-2Cu-1Zn.

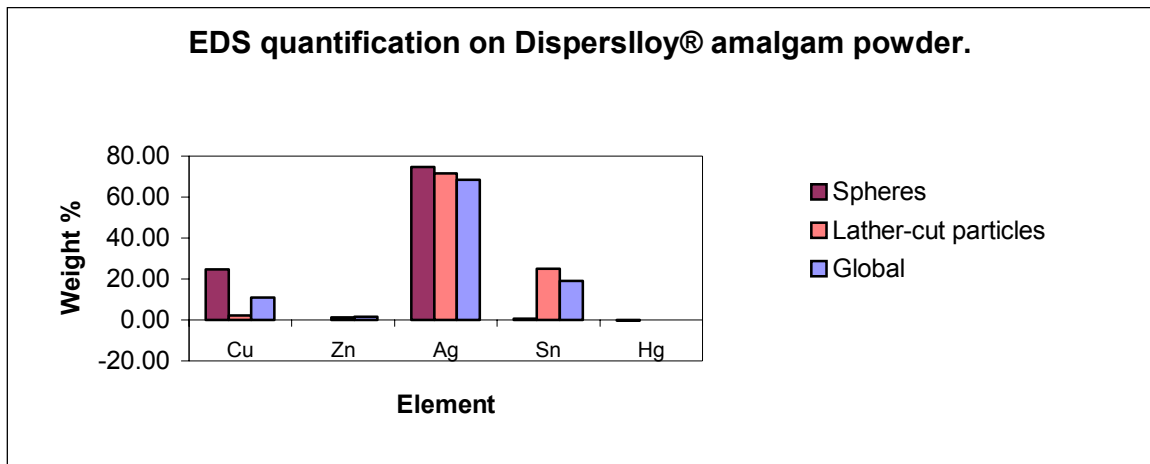


**Fig. 5.9: EDS spectra for analysis made on amalgam powder for sample 11.1.**

<sup>1</sup> Mercury vapor pressure: 0.001201 mmHg at 20 °C [48]

**Table 5.2. EDS quantification results (ZAF method, normalized results).**

Elmt	A, Sphere			B, Lather particle			Global		
	Weight %	Error	Atomic %	Weight %	Error	Atomic %	Weight %	Error	Atomic %
Cu	24.77	0.33	35.86	2.04	0.20	3.47	10.81	0.37	17.19
Zn	-	-	-	1.20	0.24	1.99	1.53	0.34	2.37
Ag	74.81	0.44	63.79	71.53	0.43	71.64	68.43	0.58	64.11
Sn	-	-	-	25.08	0.37	22.83	19.09	0.48	16.26
Hg	-	-	-	-	-	-	-	-	-

**Fig. 5.10: EDS quantification results (ZAF method, normalized results).**

Powder analysis results are reported in Figures 5.8, 5.10 and Table 5.2, while the different component images are illustrated in Figure 5.11 below.

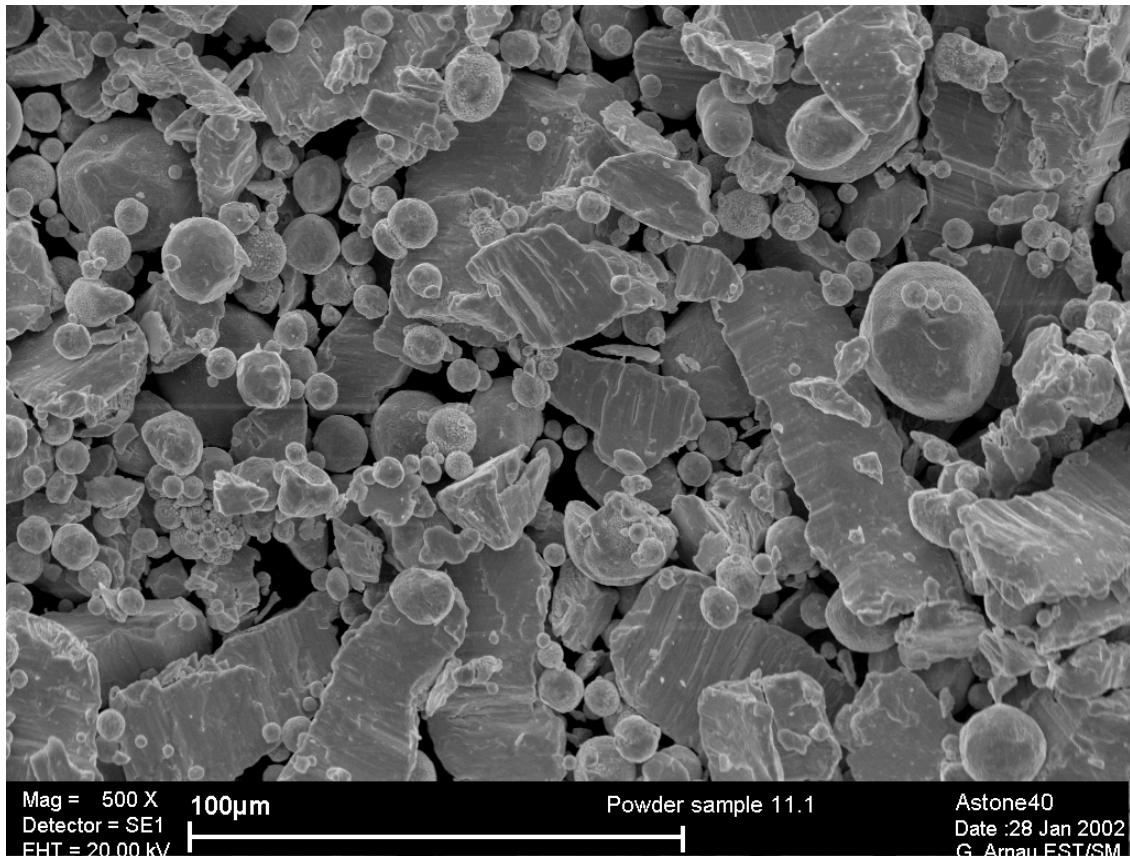


**Fig. 5.11: SE image. General view. Observation confirms manufacturer informations, powder is made of spheres (A) and lather-cut particles (B).**

### 5.6.2 Amalgam samples' analysis

Secondary electron emission analysis (SE) analysis permits to trace sample's planimetry and to evidence cavities as well as superficial roughness, but with low brightness and image definition. In SE image (Figure. 5.12) two types of porosity are visible 1) round pores always inside round structures, they correspond to previous porosity inside particles of amalgam raw powder 2) porosities in the matrix due to lack of compaction during amalgamation. The discovered cavities have dimension of approximately 10  $\mu\text{m}$ . The observation has been repeated tilting the sample of  $45^\circ$  in order to make asperities more visible (figure 5.13). With BSE analysis different phases of the material are put in evidence (Figure 5.12). Darker regions correspond to higher mean atomic number. White particles and stains are preparation artifacts.



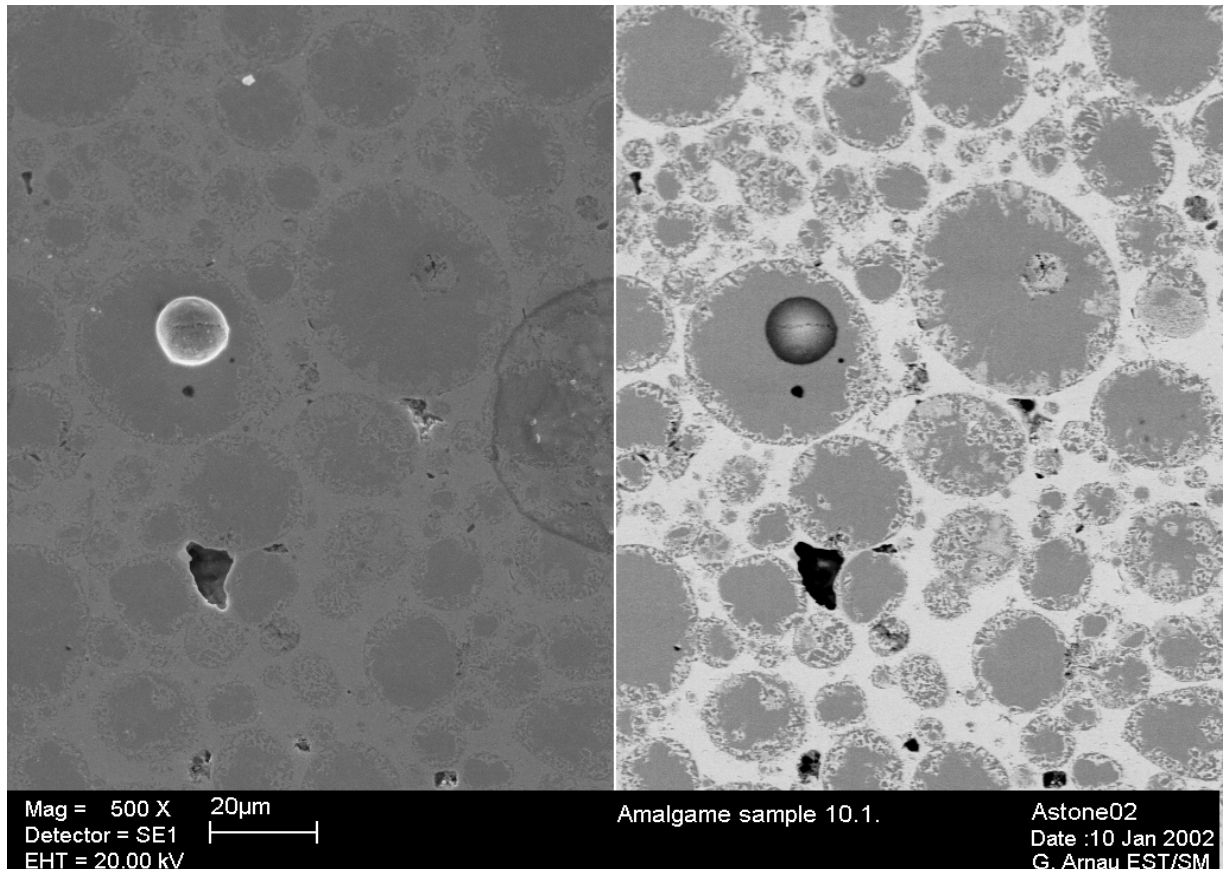


**Fig. 5.12: Sample 10.1, 500 times magnification; Left SE image, Right BSE image.**

Enlargements up to 5000 times revealed the presence of bubbles of the same kind of those observed by optical microscope. Nevertheless is not possible to identify whether those bubbles are small mercury droplets or not as their dimension is too low ( $\approx 5 \mu\text{m}$ ) for a punctual EDS analysis. The bubbles do not seem to be self-detachable from sample's surface.

Amalgam's microstructure presents two types of structures in a matrix: 1) round and 2) irregular, sizes are similar to powder particles (see section 5.7.1). Round structures present a fringe, but the different phases are smaller and not discernible. The approximate composition in the middle of round structures is equivalent to sphere particles of the powder and in the fringe is 42Sn-30Cu-17Hg-10Ag-1Zn.

Irregular structures composition is equivalent to lathe-cut particles of the powder, they present in some cases a Cu rich phase of approximate composition 57Cu-39Sn-2Ag-2Zn.

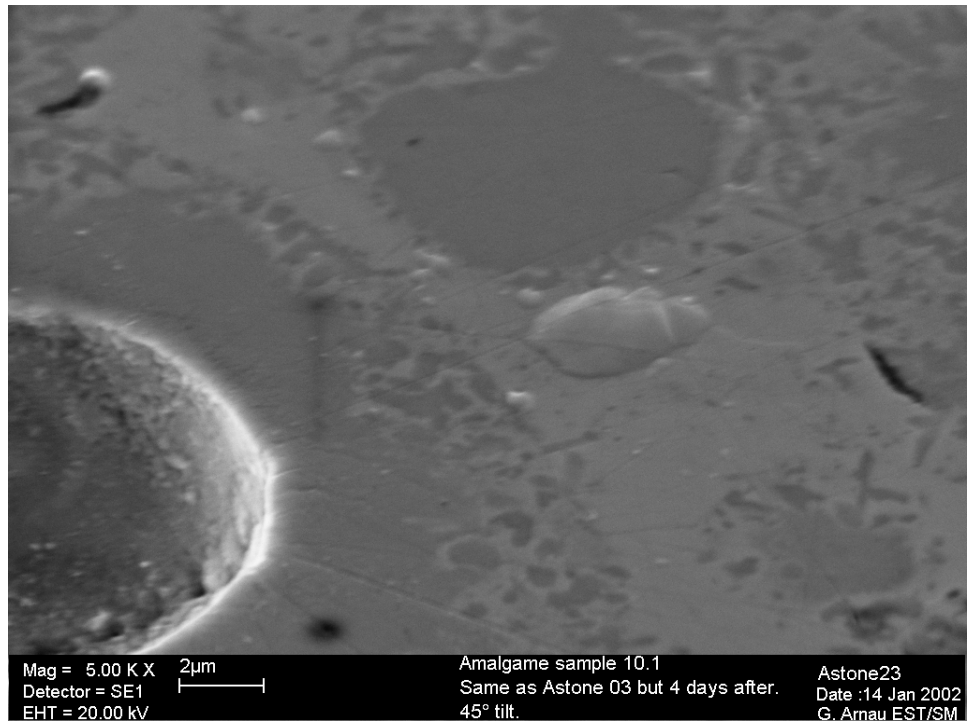


*Fig. 5.13: Sample 10.1, 5000X, SE image / 45° tilted image*

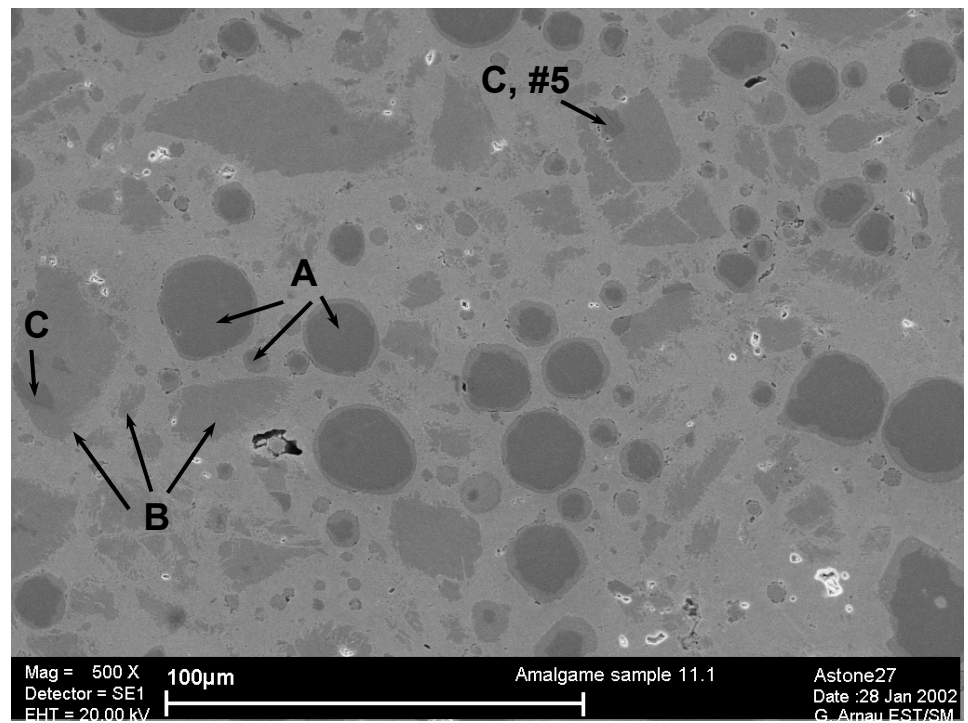


*Fig. 5.14: Sample 11.1: SE image. General view.*

On sample's surface one can distinguish four main regions characterizing the alloy (Fig. 5.14). Rounded (A) and irregular (B) structures in a matrix, they correspond to different amalgam powder particles (Ag-Cu eutectic spheres and lather-cut particles respectively, see section 5.7.1). Also some irregular structures contain small darker regions (C, EDS analysis #5, Fig. 5.12).

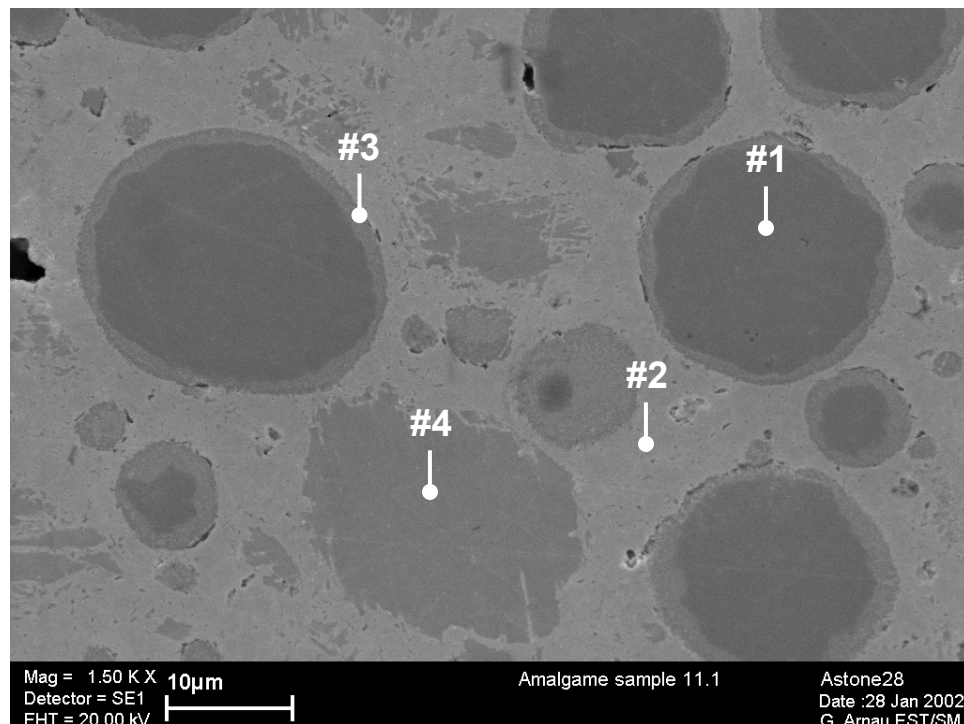


**Fig. 5.15: Sample 11.1: SE image. Detail from previous figure. Position of EDS analysis #1, #2, #3 and #4.**

The diffusion of Hg inside the rounded areas modifies the edges of type A structures creating a lighter aureole (D).

Punctual EDS analysis have been carried out in points indicated in Figure 5.15. EDS spectra are reported in Figure 5.16 while quantification of the results is summarized in Table 5.3 and Figure 5.17.

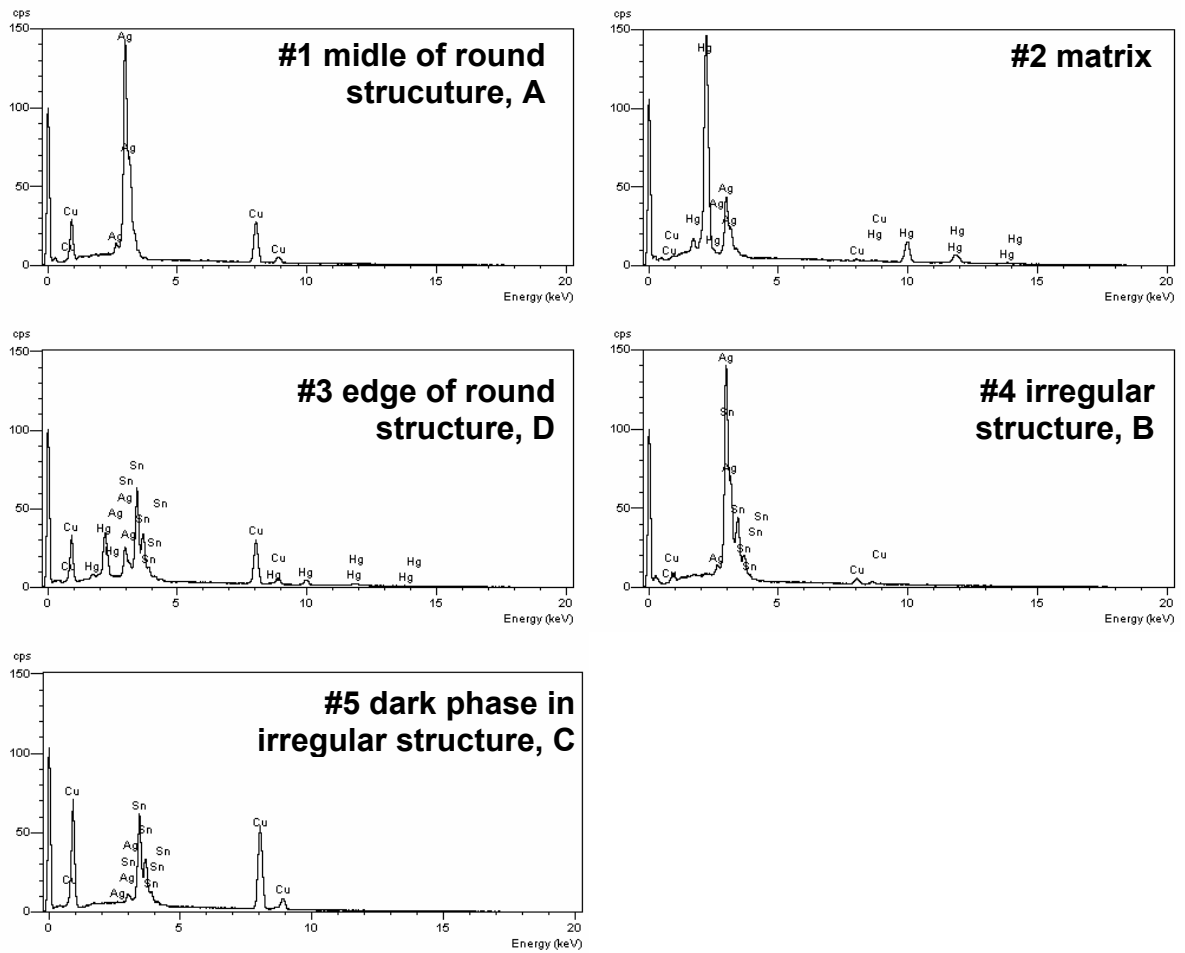
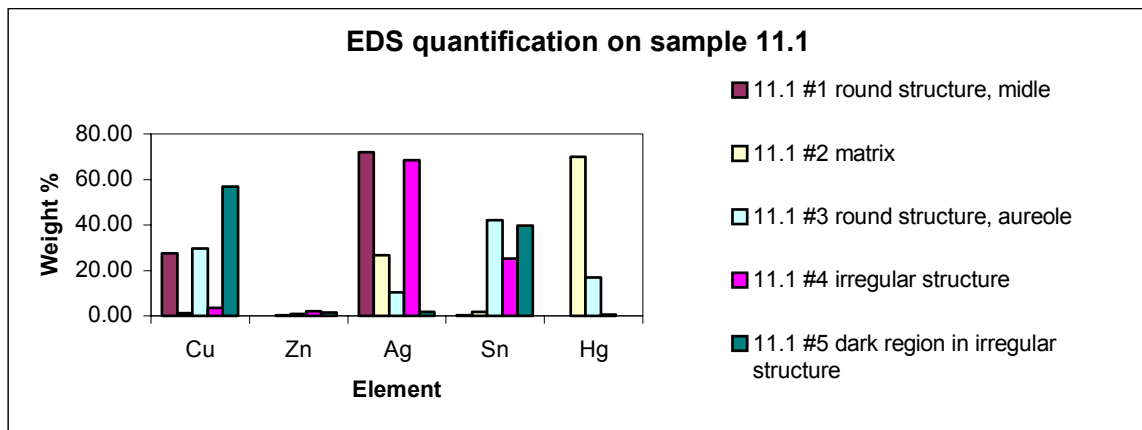


Fig. 5.16: EDS spectra for analysis on figures 5.10 and 5.

Tab. 5.3: EDS quantification results (ZAF method, normalized results).

Elmt	#1			#2			#3			#4		
	Weight %	Error	Atomic %	Weight %	Error	Atomic %	Weight %	Error	Atomic %	Weight %	Error	Atomic %
Cu	27.69	0.36	39.40	1.22	0.21	3.02	29.67	0.37	45.91	3.57	0.23	5.98
Zn	-	-	-	-	-	-	0.99	0.27	1.50	2.13	0.27	3.47
Ag	71.90	0.46	60.27	26.74	0.38	39.06	10.36	0.29	9.44	68.30	0.46	67.46
Sn	-	-	-	1.92	0.29	2.54	42.12	0.39	34.90	25.31	0.40	22.72
Hg	-	-	-	69.95	0.47	54.95	16.86	0.28	8.26	-	-	-
	#5											
Cu	56.91	0.41	70.48									
Zn	1.60	0.27	1.93									
Ag	1.77	0.22	1.29									
Sn	39.62	0.37	26.27									
Hg	-	-	-									



*Fig. 5.17: EDS quantification results (ZAF method, normalized results).*

## 5.7 EDS mapping analysis

Further investigation with EDS electron microscope analysis, permitted to trace a mapping of distribution of amalgam components after sample's preparation. Capturing photons emitted from sample's surface when bombarded with electron beam it was possible, to trace a mapping of alloy's component within the matrix.

Figure 5.18 below shows the area chose for mapping analysis. The same area is represented in figures 5.19, 5.20, 5.21, 5.22 that show components' distribution in the alloy, while Figure 5.23 illustrate the global distribution of all components.

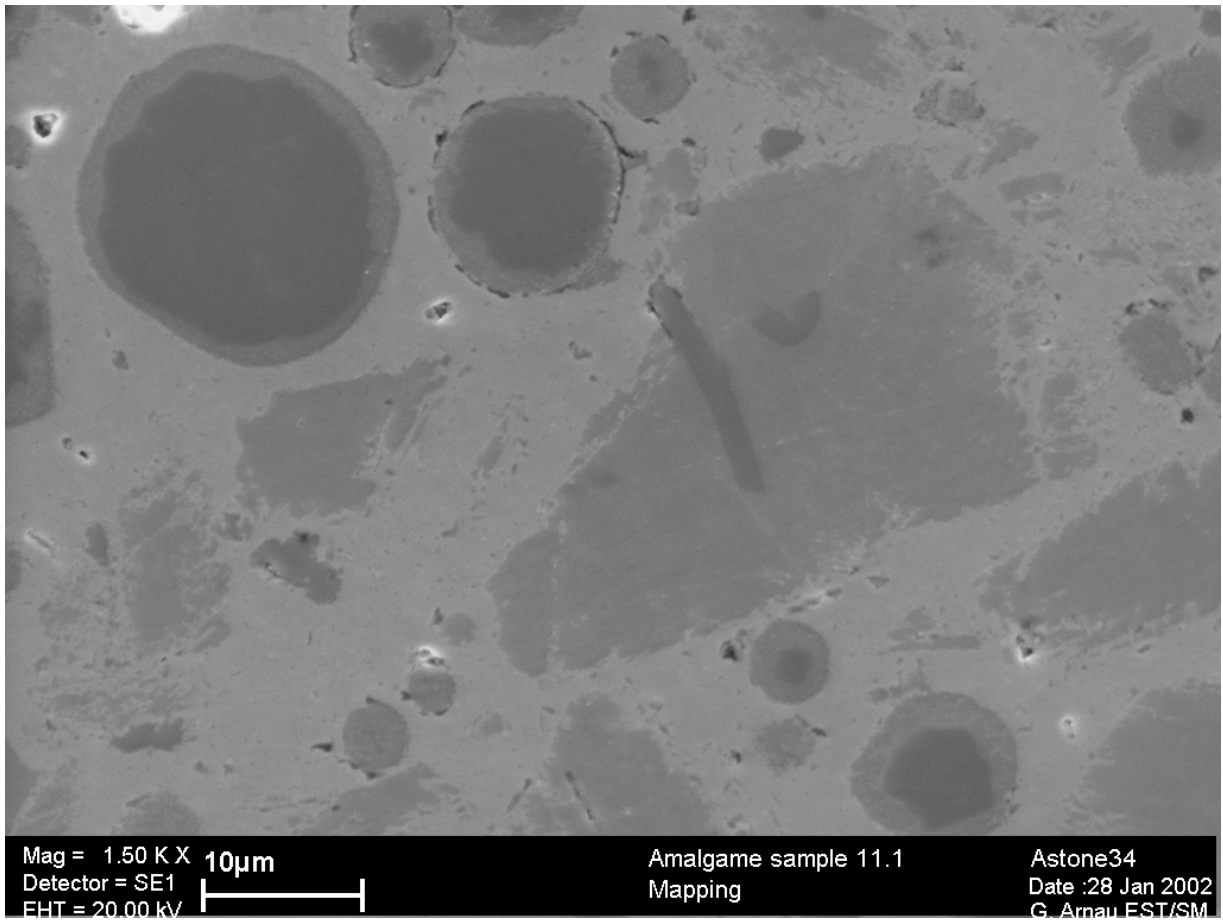


*Fig. 5.18: Sample 11.1, 1500 times magnification; BSE electrons image*

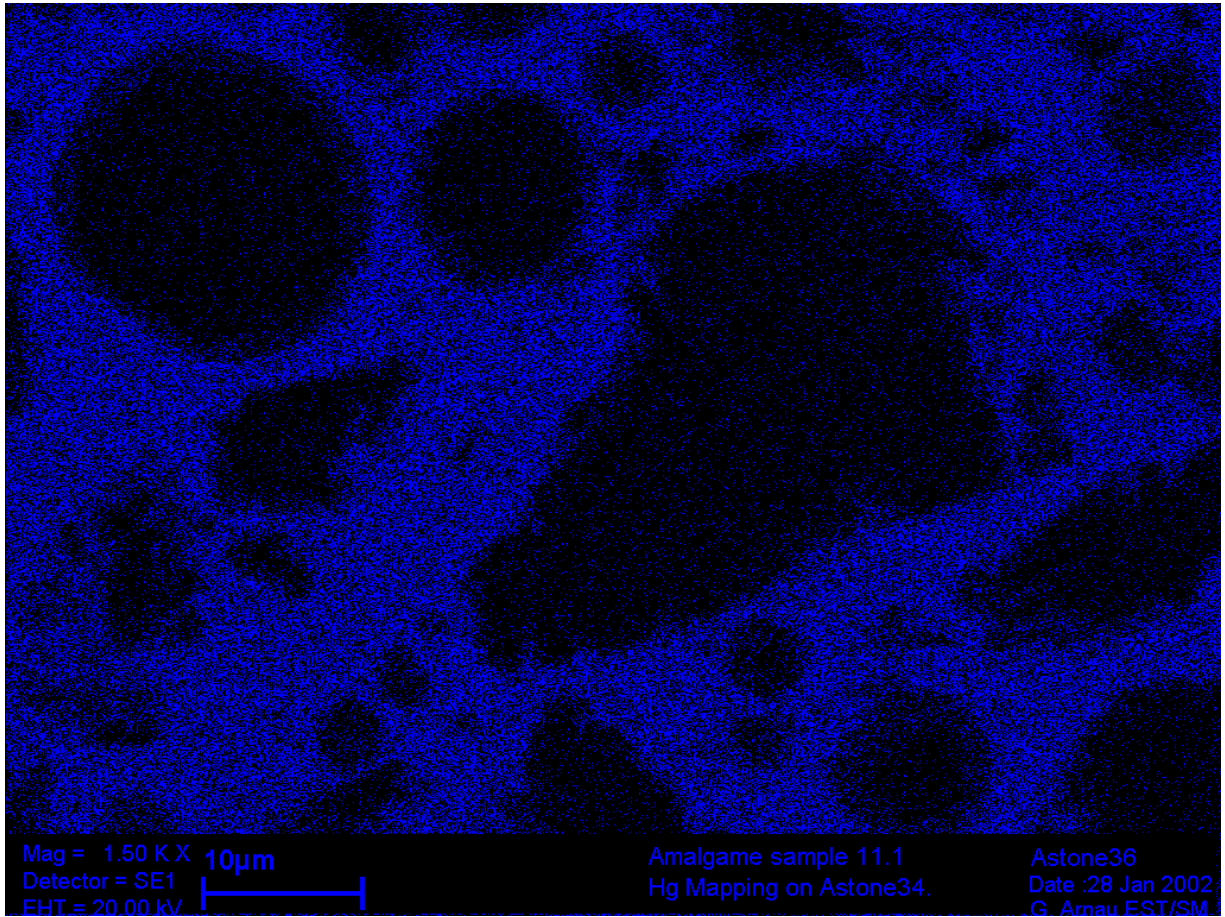


*Fig. 5.19: Sample 11.1, 1500 times magnification Hg mapping*



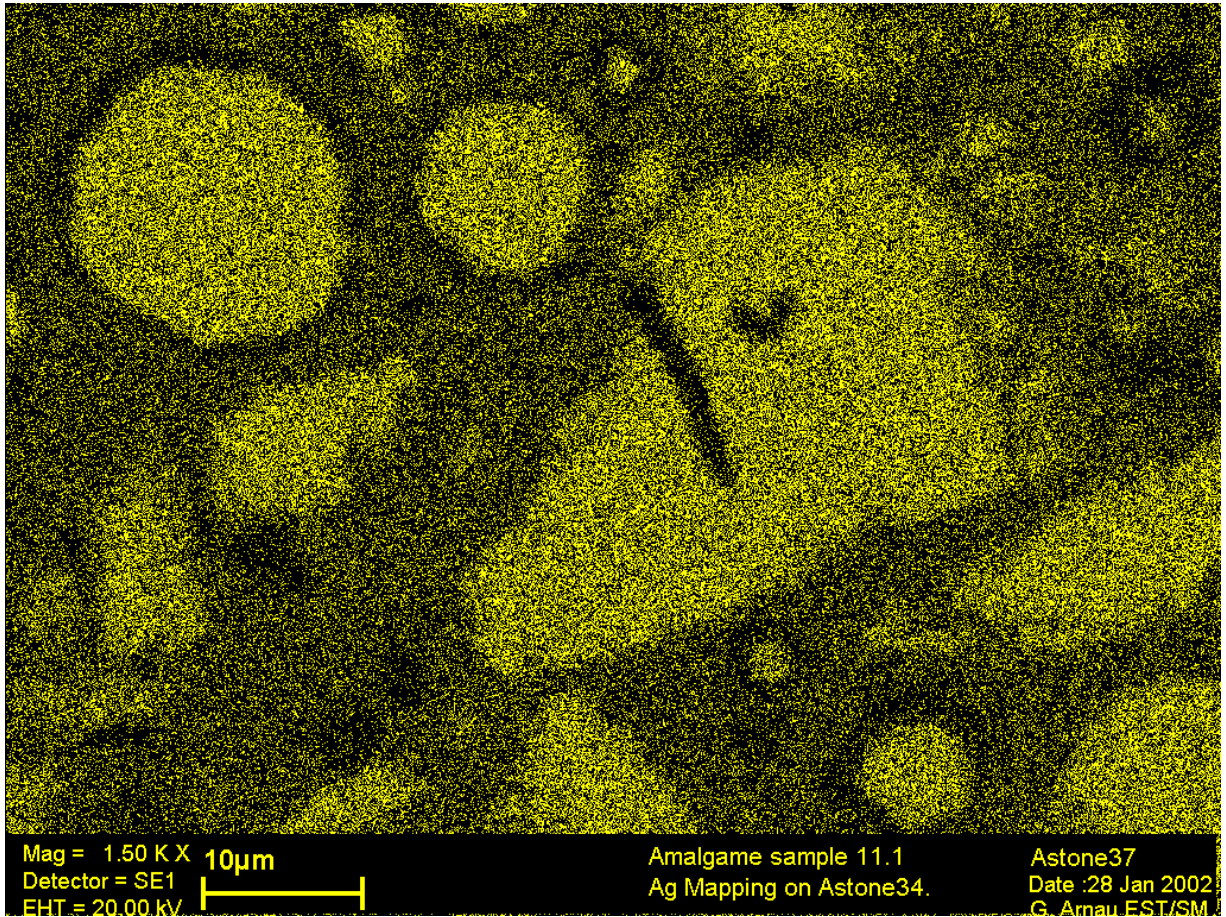


*Fig. 5.20: Sample 11.1, 1500 times magnification Ag mapping*



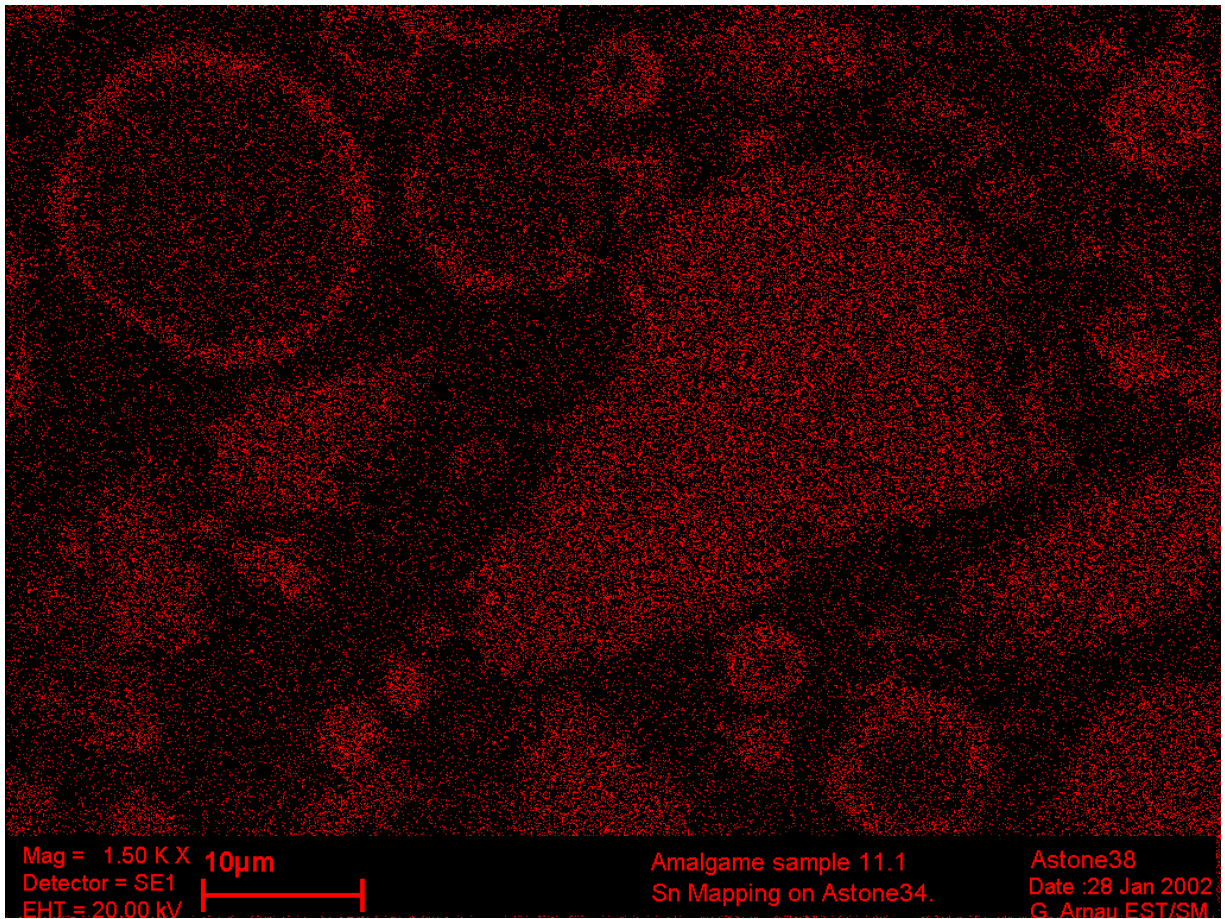


*Fig. 5.21: Sample 11.1, 1500 times magnification Sn mapping*

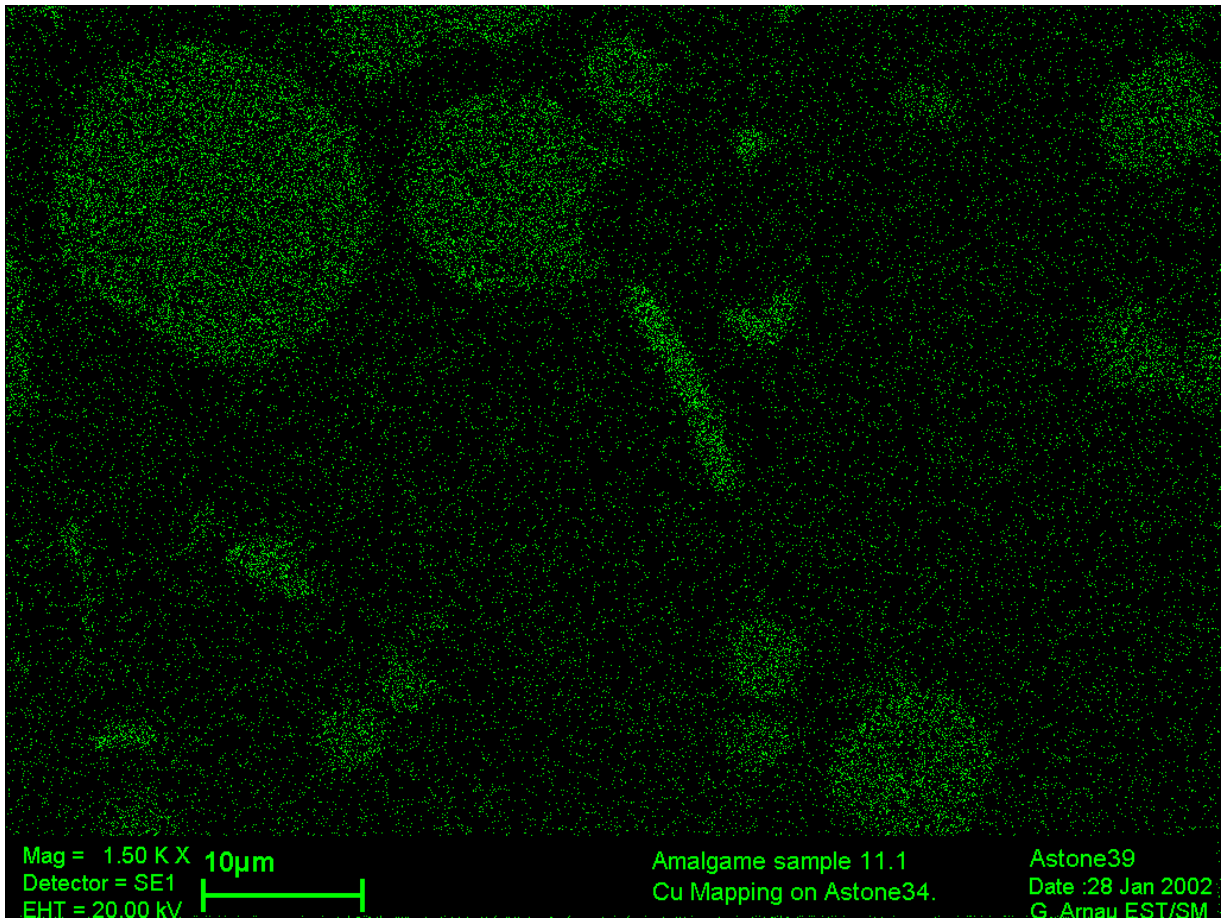


*Fig. 5.22: Sample 11.1, 1500 times magnification Cu mapping*

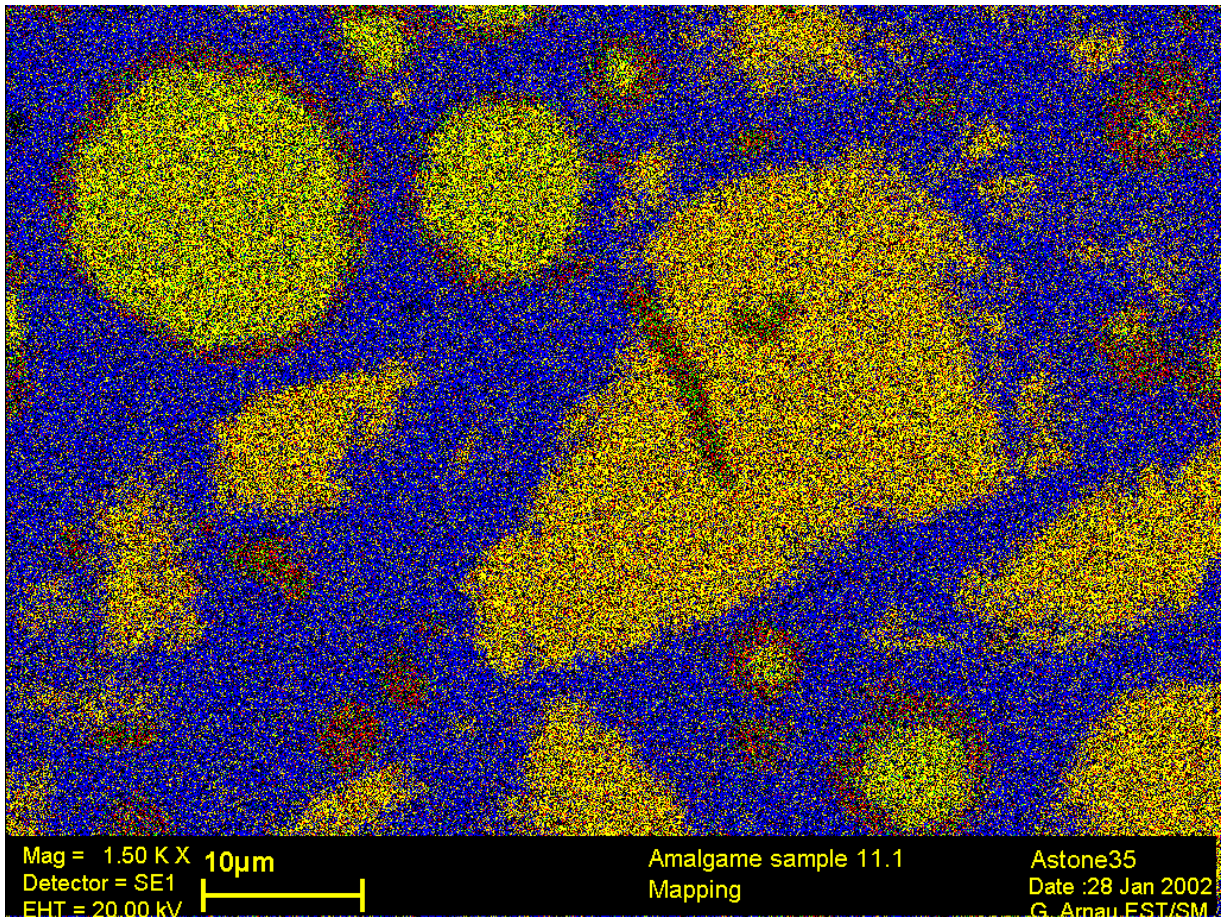


*Fig. 5.23: Sample 11.1; global mapping*

### 5.7.1 Results

The analysis confirmed the expectations that elements were almost equally distributed inside alloy's matrix. The only slight difference in element's distribution is represented from mercury and silver.

As shown from pictures 5.21 and 5.22 while tin and copper are almost homogeneously distributed, mercury and silver have different concentration and they often are separated one from each other and do not share the same area.

Mapping analysis made possible to identify dark regular and irregular spots present in amalgam matrix. Those black spots are regions in which silver's atoms concentration is higher than in other regions. Contrarily more light regions contain a larger amount of mercury atoms. This difference in components' concentration may also be checked while looking at micro hardness test as will be pointed out in section 5.10.

Form samples' mapping is possible to extrapolate why mercury seems to come out of samples' surface even once it is polished. The reason could be imputable to a too high concentration of



mercury's atom in the much lighter region. Such a gradient in concentration leads to mercury's diffusion through matter towards regions where its presence is lower, in other word towards silver occupied regions where mercury's atom presence is lower.

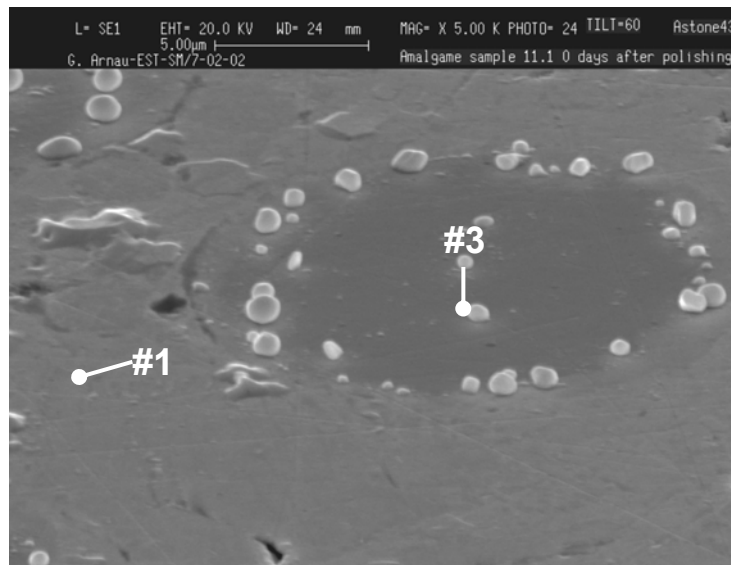
## 5.8 Sample observation in time

After a time period of ten days, small light relieves came up, either pearl-like features on the edges of round structures, or hills on some matrix regions (see Figures 5.24 and 5.25). The physical state of those features is not clear, pearls are not perfectly spherical as would correspond to a liquid. This phenomenon takes place in the dark regions in which silver's atoms concentration is higher.

From the non perfect spherical shape of bubbles formed with time on top of the flat sample 11.1 surface, one can conclude that they are not in liquid state. They could be  $\gamma$  phase [expl,ref] formed by further diffusion of mercury due to difference in elements concentration within the alloy's matrix.

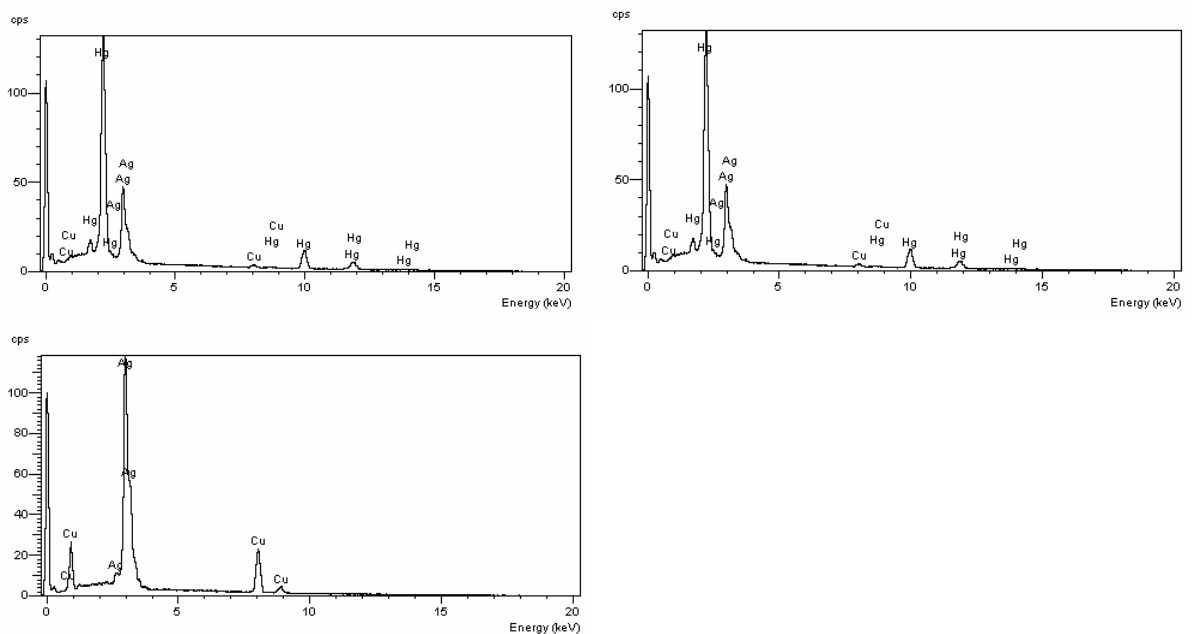


*Fig. 5.24: Sample 11.1. SE image. Tilted sample; sample 10 days after polishing.*



**Figure 5.25: SE image. Tilted sample. Detail from previous figure. Position of EDS analyses #1, #2 and #3.**

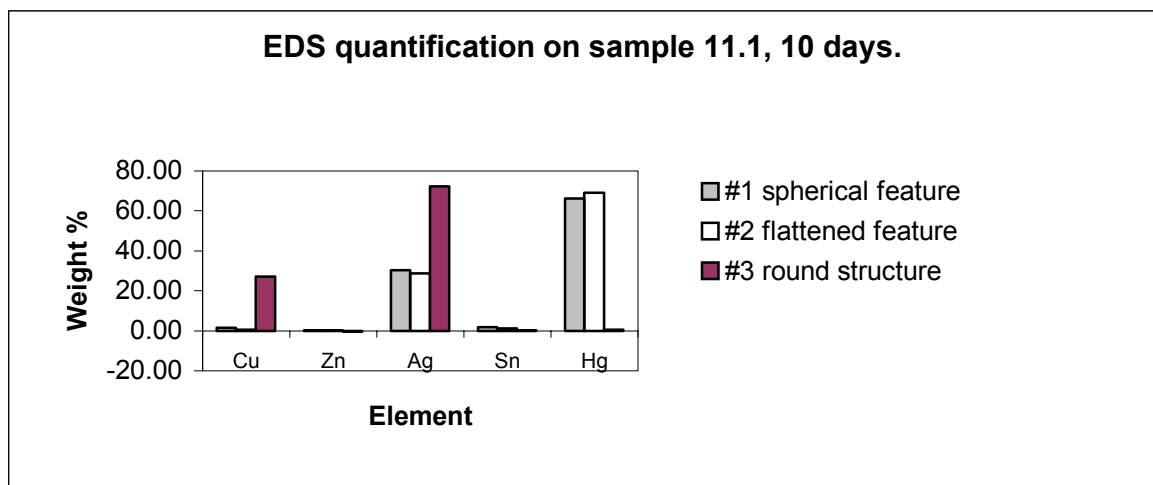
EDS analysis performed on the samples revealed the identity of these asperities (Fig.5.26, 5.27 and Table 5.4). From the analysis one may conclude that pearl-like and hilly features have a composition similar to the matrix. Round structure composition has not changed sensibly if compared with previous measurements.



**Fig. 5.26: EDS spectra for analysis on figure 20**

**Tab. 5.4. EDS quantification results (ZAF method, normalized results).**

Elmt	#1, spherical feature			#2, flattened feature			#3, round structure		
	Weight %	Error	Atomic %	Weight %	Error	Atomic %	Weight %	Error	Atomic %
Cu	1.46	0.21	3.53	0.65	0.23	1.60	27.13	0.39	38.86
Zn	-	-	-	-	-	-	-	-	-
Ag	30.28	0.39	43.02	28.87	0.41	42.15	72.39	0.51	61.08
Sn	1.87	0.31	2.42	1.18	0.32	1.57	-	-	-
Hg	66.19	0.47	50.57	69.13	0.50	54.27	-	-	-

**Fig. 5.27: EDS quantification results (ZAF method, normalized results).**

## 5.9 Micro hardness test

Micro hardness test has been on samples 10.1 and 10.2. Since the two amalgams are slightly different one from the other, test was carried out in a different way on each sample. In both case the same force of 0.5 N has been applied to the probe that had to penetrate samples' surface. A tool with a point of constant dimension has been used.

Concerning sample 10.1, as alloy's structure is more regular, it was possible to choose where to take the different measurements; if inside the dark spots or in the white matrix.

For measurements taken inside dark spots, their center was chosen as the right place to measure Vickers hardness. On the other side, for measurements taken in the white matrix, a region with a considerable extension between dark spots has been taken in consideration.

Micro hardness measurements reveals in this case values that space from 248.6 Hv up to 380 Hv inside dark spots with an average value of approximately 299 Hv. Concerning much bright regions micro hardness value recorded space from 183 Hv up to 237.5 Hv with an average value of 211.5 Hv. This means that higher hardness values correspond to regions where silver's percentage is higher.

Since structure of sample 10.2 is more complex than sample 10.1 is very difficult to distinguish between different phases. It often happens that in the area covered by the point of measurement instrument's point several phases are present. Then it has not been possible to choose measurements places accurately as done in the previous case. Technique followed is to measure hardness in a random way. A much higher number of measurements have been carried out in order to guarantee a better approximation of the average value.

The registered values vary from 144 Hv up to 336 Hv with an average value of 231 Hv.

## 5.10 Conclusions

Amalgams are metallic composites formed by diffusion reaction in which liquid mercury is replaced by solid mercury compounds. Mercury dissolves silver from both kinds of powder particles to form  $\gamma$  phase (solid below 127°C) that would constitute the matrix component of amalgam microstructure. Excess copper from sphere eutectic particles and excess tin from lather-cut particles together with mercury may form a diversity of intermetallic compounds. Since tin is more soluble in liquid mercury than copper it is reasonable that formation of those intermetallics takes place close to copper source, once the system is solid the only mechanism is diffusion, for those reasons former sphere particles are surrounded of a fringe of intermetallics.

After a global analysis of achieved results coming from all tests carried out on prepared amalgam samples, it is possible to observe that obtained alloy amalgams are not fully dense. In alloy's matrix many different phases are visible; by the way this feature does not create a problem as is demonstrated that mercury is totally bound to other components.

The presence of small regions that look like mercury droplets coming out of the samples' surface have been observed. The observed areas are of negligible dimensions (2÷4  $\mu\text{m}$ ) and show not to be detachable from samples' surface save exerting an abrasive action by grinding on it. At last taking in consideration dimensions of these (so presumed) droplets and considering their limited superficial density they seem not susceptible to pollute surrounding environment.

Described tests, carried out on samples of series from 1 to 8 (see logbook in appendix 2.5), pointed out that alloy's properties are influenced by parameters as shaking time, centrifugation and mercury percentage in the alloy. Shaking time influences alloy's malleability in a way that the longer amalgam is shaken, the harder is alloy extracted from the capsule. This test pointed out that particular attention must be paid in choosing the right shaking time as exaggerating

shaking time, alloy can change from a malleable paste to a powder composed of crumbs of amalgam.

Alloy extracted from the capsule emits a considerable quantity of mercury vapors as verified with vapor detector device. Such values are considerably over the limit established for safeguarding human health. Measured values go up to a concentration of 800  $\mu\text{g}/\text{m}^3$  while admitted level is only 50  $\mu\text{g}/\text{m}^3$ . Such a phenomenon attenuates with time and values, after one-day time re-enter in safety limit (see appendix 2.6 for international chemical safety card). Monitoring mercury vapor concentration pointed out that particular attention must be paid in handle amalgam after its production.

In conclusion the proposed idea of using silver dental amalgams as an instrument to confine radioactive mercury in a solid phase may be exploited in order to store it accordingly to safety issues.



## Bibliography

- [1] Review of particle physics, Eur. Phys. Journal C **15**, 74 (2000)
- [2] <http://public.web.cern.ch/Public/SCIENCE/ParticlePhysicsToday.html>, accessed 5-10-2001
- [3] “Quark model”; The European Physics Journal, 15, 117, number 1-4,2000
- [4] The European Physic Journal C p.VI.10 1992 edition, Phis.Rev.D45
- [5] K. R. Lang, Astrophysical Formulae, Springer-Verlag, 1986, preface.
- [6] CERN Currier – Making muon rings round neutrino factories IOP publishing.
- [7] <http://hyperphysics.phy-astr.gsu.edu/hbase/nuclear/radact2.html>, accessed 7-12-2001
- [8] Atomic structure, <http://learn.chem.vt.edu/tutorials/atomic/pep.html>, accessed 12-12-2001
- [9] Figures in radiation history, <http://orcbs.msu.edu/radiation/radhysatory/antoinebequerel.html>, accessed 31-07-2001
- [10] The neutrino, <http://choruswww.cern.ch/Public/textes/english/node1.html>, accessed 15-11-2001
- [11] What is a neutrino?, <http://www.sciam.com/askexpert/physics/physics55/physics55.html>, accessed 1-12-2001
- [12] Y. Fukuda et al.: Phis.Rev. Lett. 81, 1562 (1998)
- [13] V. M. Lobachev et. al: Direct search for neutrino mass and anomaly in the tritium beta spectrum, Physics letters B 460, 227 (1999)
- [14] Aleph Collaboration: An upper limit for the tau neutrino mass from three-and five-prong tau decays, Europ. Phys. Journal C 2, 395 (1998)
- [15] DONUT collaboration: Nucl. Phys. Proc. Suppl. 9, (1999)

- [16] The LEP collaboration: A combination of preliminary electroweak measurements and constraints on the Standard Model, CERN/EP/2001-021, 61
- [17] The sources of neutrino, <http://www.lapp.in2p3.fr/neutrinos/ansources.html>
- [18] J. N. Bahcall Rev. Mod. Phys. 50, 881 (1978)  
J. N. Bahcall and M. Pisonneault, Phys. Rev. D 58, 6016 (1998)
- [19] Z. Maki, M. Magakawa and S. Sakata, Prog. Theor. Phys. 28, 870 (1962)
- [20] Expression of interest for R&D towards a neutrino factory based on a storage ring and muon collider. Edited by K. T. McDonald, Nov 7, 1999
- [21] B. Autin, A. Blondel, J. Ellis: Prospective studies on muon storage rings at CERN, CERN yellow report, 99-02
- [22] The SPL study group, M. Vretnar, "Conceptual design of the SPL - a high-power superconducting proton H- linac at CERN", CERN 2000-012
- [23] R. Garoby, "Status of European studies for a neutrino factory at CERN", CERN/PS 2001-055 (RF), NUFAC NOTE 089
- [24] B. Autin et al., "Design of a 2.2 GeV accumulator and compressor for a neutrino factory", CERN -PS/200-011(AE), June 15, 2000
- [25] N. Simos, H. Kirk et al., Interaction of a 24 GeV Proton Beam with a Muon Collider Mercury Jet Target. Experimental Results and Thermodynamic Assessment, (Nov. 9, 2001). <http://www.hep.princeton.edu/~mcdonald/mumu/target/#jpeg>
- [26] N. V. Mokhov: Particle production for a muon storage ring: I. Targetry and  $\pi/\mu$  yield, FERMILAB-Cinf-00/208 (2000)
- [27] M. G. Catanesi et al.: HARP: A Hadron Production Experiment Neutrino Factory and the Atmospheric Neutrino Flux, CERN-SPSC P315 (1999)
- [28] B. Autin, Ph. Royer, "Transverse collection of pion", CERN/PS/HP 99-11, NUFAC NOTE 08

- [29] J.M.Maugain, S. Rangod, F. Voelker: Study of a horn with integrated target for a neutrino factory, CERN-NUFACT note 80, [http://molat.home.cern.ch/molat / neutrino/nfnotes.html](http://molat.home.cern.ch/molat/neutrino/nfnotes.html)
- [30] Review of particle physics, Eur. Phys. Journal C **15**, 161 (2000)
- [31] H. Kirk et al., Target studies with BNL E951 at the AGS, Proceedings of the 2001 PAC, Chicago, 2001, p1535
- [32] Introduction To Electroquasistatics and Magnetoquasistatics: [http://web.mit.edu/6.013\\_book/www/chapter3/3.1.html](http://web.mit.edu/6.013_book/www/chapter3/3.1.html) ,accessed 4-2-2002
- [33] D.Schaffarzick, Experimental Investigation of Proton Induced Thermal Shocks and Magnetohydrodynamic Effects in Molten Metal Pion Production Targets for a Neutrino Factory, Wels (Austria), 2001
- [34] Muon collider target, [http://www.bnl.gov/cdic/Sci\\_Projects/High\\_Energy/Muon \\_ Collider/muon\\_collider.htm](http://www.bnl.gov/cdic/Sci_Projects/High_Energy/Muon_Collider/muon_collider.htm) ,accessed 10-2-2002
- [35] Magnetohydrodynamics of Multifluid Systems: [http://www.bnl.gov/cdic/ Sci\\_Projects/Basic\\_Energy/MHD/mhd.htm](http://www.bnl.gov/cdic/Sci_Projects/Basic_Energy/MHD/mhd.htm), accessed 5-2-2002
- [36] The European physical journal, 15, number 1-4, 2000, p.163
- [37] P. Sievers and P. Pugnati, Response of solid and liquid targets to high power protons beams for neutrino factories, CERN-NuFact note 035; <http://molat.home.cern.ch/molat/neutrino/nfnotes.html>
- [38] P. Pascal, Nouveau traite de chimie minerale VI, p. 468, 477
- [39] L. Lando' Rebaudengo, G. Scersi, Appunti di meccanica dei fluidi, **2**, p. 57
- [40] H. Haserolt, CERN ideas and plans for a neutrino factory, CERN/PS 200-064 (PP), CERN-NUFACT Note 45
- [41] B. S. Massey, Mechanics of fluids, p 293-295
- [42] [www.xtronics.com/references/viscosity](http://www.xtronics.com/references/viscosity), accessed 20-1-2002
- [43] F. W. Fraim and W. H. Heiser, The Effect of a strong longitudinal magnetic field on the flow of mercury in a circular tube, J. fluid Mech. (1968), **33**, part 2, pp. 379-413

[44] The European physical journal, Vol 15, num. 1-4/2000, pag.212

[45] The European physical journal, Vol 15, num. 1-4/2000, pag.211

[46] Dott. Roberto Zambrini, private communication, 8-2001

[47] [http://www.polymerweb.com/\\_misc/specgrav.html](http://www.polymerweb.com/_misc/specgrav.html)

[48] Paul Pascal, Nouveau traite de chimie minerale, Tome V pag.495

[49] A.Fabich, J.Letry, Experimental Observation of Proton-Induced Shocks and Magneto-Fluid-Dynamics in Liquid Metal, proceedings NuFact01, to be published in NIM A

# Appendix 1

## 1.1 Camera specifications

<b>Sensor resolution</b>	656x496 pixels, each $7.4 \mu\text{m}^2$
<b>Recording rates</b>	60, 125, 250, 500, 1000, 2000, 4000 and 8000 fps
<b>Exposure rates</b>	Electronic shutter operates at rates of 1x to 20x of set recording rates. Ranges from 1/60th sec to 1 /80000 <sup>th</sup> sec.
<b>Frame storage</b>	512,1024,2048,4096,8192,12288,16384,24576,32768-frames
<b>Playback rates</b>	1,2,3,4,5,10,30,60,125,250,500,1000,2000,4000 and 8000 fps, forward or reverse. Single frame step mode.
<b>External connection</b>	Trigger, strobe data record, video out and Phase Lock in-out on the camera cable
<b>Video output</b>	RS-170 NTSC and PAL (monochrome or color, switchable) BMC connector to VCR and external monitors.
<b>Trigger input</b>	(1)0V input (held to ground by a 2K resistor at the source, rising to +5V.(2) Contact closed rising to +5V when contacts open. (3) +5V falling to 0V by a contact closure.BNC connector
<b>Data recording</b>	Two TTL inputs (inputs 0 and 1) through two BNC connectors on the camera cable. Input normally at +5V (white marker) falling to 0V by contact closure (black marker)
<b>Lens</b>	Standard C mount
<b>Size</b>	Controller, full size PCI card, two slots required. Camera head (6.2cm) H, (6.2cm) W, (10cm) L.
<b>Weight</b>	Controller 0.5 kg, camera head 0.7kg
<b>Power</b>	Controller: +12 V DC-1.5 A; +5 V-3.0 A
<b>Operating environment</b>	-18 °C to 40 °C

## 1.2 Thimble test events summary

#set	#pulse	recurrences	Intensity/bunch [ppb [TP]]	Intensity/bunch [10 <sup>×12</sup> ppb [TP]]	spot size [mm]	number of bunches [rings] bpb [rings]	intensity/pulse [10 <sup>×12</sup> ppb [TP]]	spacing [ns] spacing
1	1	2	2	2.2	1	2	-1000	
2	2	2	6	2.2	1	6	-1000	
3	2	2	8	2.2	1	8	-1000	
4	2	2	10	2.2	1	10	-1000	
5	1	1	1	2.8	1	1	-1000	
6	1	1	3	2.8	1	3	-1000	
7	1	1	7	2.8	1	7	-1000	
8	1	1	10	2.8	1	10	-1000	
9	1	1	2	3.5	1	2	-1000	
10	1	1	6	3.5	1	6	-1000	
11	1	1	10	3.5	1	10	-1000	
12	0	0	8	2.2	1	8	-1000	
13	1	1	4	2.2	2	8	350 / 286	
14	1	1	3	2.2	3	9	350 / 286	
15	1	1	2	2.2	4	8	350 / 286	
16	8	1	8	2.2	1	8	-1000	
17	1	1	4	2.2	2	8	800 / 858	
18	1	1	3	2.2	3	9	800 / 858	
19	1	1	2	2.2	4	8	800 / 858	
20	4	1	4	2.2	2	8	350 / 286	
21	4	1	4	2.2	2	8	800 / 858	
22	4	1	4	2.2	2	8	1500 / 1430	
23	1	1	4	2.2	2	8	1500 / 1430	
24	1	1	4	2.2	2	8	2400 / 2288	
25	1	1	4	2.2	2	8	5250 / 4290	
26	1	1	4	2.2	2	8	9450 / 7722	
27	1	1	1	2.2	4	4	1400 / 1144	
28	1	1	2	3.5	4	8	1400 / 1144	
29	1	1	3	3.5	4	12	1400 / 1144	
30	1	1	4	3.5	4	16	1400 / 1144	
31	1	1	6	3.5	4	24	1400 / 1144	
32	1	1	8	3.5	4	32	1400 / 1144	
33	1	1	4	2.2	2	8	1500 / 1430	
34	1	1	4	2.2	2	8	1500 / 1430	
35	1	1	4	2.2	2	8	1500 / 1430	
36	1	1	4	2.2	2	8	1500 / 1430	
37	1	1	4	2.2	2	8	1500 / 1430	
38	1	1	4	2.2	2	8	1500 / 1430	
39	1	1	4	2.2	2	8	1500 / 1430	
40	1	1	4	2.2	2	8	1500 / 1430	
41	1	1	4	2.2	2	8	1500 / 1430	



				Relative positions at time (t-to)																
		data Set	#pulse	event #		[mm]														
				Event	0.00	0.25	0.50	0.75	1.00	1.50	2.00	3.00	4.00	5.00	6.00	7.00	8.00	9.00		
ppb(1 b, h=3, s=2.2)	3	0	101	1	1	0.0	0.6	1.4	1.6	1.8	2.1	3.2	5.5	6.7	7.7	9.0	9.8	10.6	11.0	
ppb(1 b, h=3, s=2.2)	3	0	102	2	2	0.0	0.1	2.3	3.9	5.6	7.9	9.8	13.8	17.6	20.8	23.8	26.5	29.1	31.5	
ppb(1 b, h=3, s=2.2)	3	0	103	3	3	0.0	0.4	3.9	5.8	7.6	10.4	13.1	18.4	23.4	27.2	32.8	36.4	40.7	44.2	
ppb(1 b, h=3, s=2.2)	3	0	104	4	4	0.0	1.1	4.9	7.5	9.6	13.1	16.2	21.7	28.4	33.4	38.5	43.6	46.6		
ppb(1 b, h=3, s=2.8)	3	0	304	304	304	0.0	1.2	5.3	9.2	11.2	13.7	16.5	22.5	28.5	34.1	38.9	43.9	49.0		
ppb(1 b, h=3, s=2.8)	3	0																		
ppb(1 b, h=0, s=2.2)	1	1	201	201	201	0.0	0.3	0.8	1.3	1.6	2.1	3.1	4.5	5.3	5.6	6.6	7.2	8.4		
ppb(1 b, h=0, s=2.2)	1	2	202	202	202	0.0	0.2	2.6	4.9	6.5	8.8	10.7	14.3	18.0	20.6	23.6	26.2	29.3		
ppb(1 b, h=0, s=2.2)	1	3	203	203	203	0.0	1.3	4.5	6.0	7.6	10.0	12.1	16.2	20.2	24.2	28.3	31.8	34.5	37.9	
ppb(1 b, h=0, s=2.2)	1	4	204	204	204	0.0	1.6	6.2	8.3	10.1	13.6	16.0	22.0	27.9	33.5	37.9	42.9	47.3		
ppb(1 b, h=0, s=2.2)	1																			
ppb(1 b, h=0, s=2.8)	2	5	205	205	205	0.0	0.3	0.4	0.5	0.7	1.5	2.1	2.9	3.6	4.2	4.8	5.2	5.4		
ppb(1 b, h=0, s=2.8)	2	6	206	206	206	0.0	1.5	3.4	4.8	6.2	8.7	9.9	11.7	13.4	15.9	18.1	20.2	22.4	24.6	
ppb(1 b, h=0, s=2.8)	2	7	207	207	207	0.0	0.8	3.6	5.1	7.3	8.4	10.0	13.3	16.9	19.9	22.9	26.2	29.1	31.3	
ppb(1 b, h=0, s=2.8)	2	8	208	208	208	0.0	1.9	4.8	7.3	8.1	9.9	11.8	15.4	19.0	22.3	25.7	28.7	31.9	34.5	
ppb(1 b, h=0, s=2.8)	2																			
ppb(1 b, h=0, s=3.5)	3	3	9	209	209	0.0	0.0	-0.3	0.0	0.3	0.7	1.1	1.8	1.9	2.4	2.1	2.0	1.8	2.1	
ppb(1 b, h=0, s=3.5)	3	3	10	210	210	0.0	0.5	2.2	3.3	4.4	6.7	7.9	10.1	11.7	12.9	14.8	17.1	18.3	20.5	
ppb(1 b, h=0, s=3.5)	3	3	11	211	211	0.0	0.5	2.4	4.3	6.3	8.5	9.9	13.1	15.6	18.5	20.7	24.0	25.9	28.6	
ppb(1 b, h=0, s=3.5)	3	3																		
n_bunch(10Tp,<1micro)	4		203	203	203	0.0	1.3	4.5	6.0	7.6	10.0	12.1	16.2	20.2	24.2	28.3	31.8	34.5	37.9	
			not 13*																	
n_bunch(10Tp,<1micro)	2	4	13	213	213	0.0	4.1	7.5	12.5	13.2	16.4	20.0	26.5	32.9	39.7	46.0				
n_bunch(10Tp,<1micro)	2	4	14	214	214	0.0	4.3	7.8	10.8	12.0	15.4	18.7	24.8	31.6	37.2	43.0	47.5			
n_bunch(10Tp,<1micro)	2	4	15	215	215	0.0	3.7	6.7	10.4	10.8	14.4	17.8	24.0	30.6	35.9	41.0	45.5			
n_bunch(10Tp,<1micro)	2	4																		
n_bunch(10Tp,>1micro)	5		203	203	203	0.0	1.3	4.5	6.0	7.6	10.0	12.1	16.2	20.2	24.2	28.3	31.8	34.5	37.9	
n_bunch(10Tp,>1micro)	2	5	17	217	217	0.0	5.6	7.9	11.3	14.5	17.1	19.0	25.3	31.1	37.3	43.8				
n_bunch(10Tp,>1micro)	2	5	18	218	218	0.0	3.6	8.4	9.6	11.8	15.6	16.2	20.7	26.0	31.0	36.1	41.2	45.3		
n_bunch(10Tp,>1micro)	2	5	19	219	219	0.0	3.3	7.7	9.4	12.4	13.9	16.4	21.8	26.9	32.0	35.9	40.9	45.4		
n_bunch(10Tp,>1micro)	2	5																		
Staggering	6		213	213	213	0.0	4.1	7.5	12.5	13.2	16.4	20.0	26.5	32.9	39.7	46.0				
Staggering	6		217	217	217	0.0	5.6	7.9	11.3	14.5	17.1	19.0	25.3	31.1	37.3	43.8				
Staggering	2	6	22	222	222	0.0	4.9	8.1	11.4	12.5	14.5	16.8	21.9	28.0	32.6	37.7	42.4	46.4		
Staggering	2	6	23	223	223	0.0	0.5	6.2	10.0	12.3	16.4	19.3	22.8	26.9	31.7	37.0	42.0	47.1		
Staggering	2	6	24	224	224	0.0	2.5	6.2	9.9	10.1	12.8	16.1	17.9	20.1	23.7	26.5	29.5	32.3	34.7	
Staggering	2	6	25	225	225	0.0	2.6	5.6	7.5	9.4	11.7	14.3	17.3	19.1	21.9	25.1	28.0	30.8	34.9	
Staggering	2	6	26	226	226	0.0	0.3	4.9	8.3	10.0	12.3	14.8	20.1	20.6	23.3	26.7	29.7	32.9	33.5	
Staggering	2	6																		
vert_scan	7	27	227	227	227	0.0	4.9	8.3	11.5	13.2	15.5	18.0	26.1	34.1	42.0	49.2				
vert_scan	7	28	228	228	228	0.0	4.5	7.9	11.3	13.5	17.6	19.3	25.1	31.2	37.9	43.9				
vert_scan	7		222	222	222	0.0	4.9	8.1	11.4	12.5	14.5	16.8	21.9	28.0	32.6	37.7	42.4	46.4		
			not 29*																	
vert_scan	7	29	229	229	229	0.0	4.5	9.1	10.6	12.5	17.0	17.9	21.5	25.7	30.2	35.2	39.4	44.4	46.8	
vert_scan	7	30	230	230	230	0.0	0.5	2.8	5.0	6.1	7.8	9.1	12.0	13.8	15.3	17.1	17.9	19.1	19.7	
vert_scan	7	31	231	231	231	0.0														
vert_scan	7																			
PPP(4 bunches)	3	8	32	232	232	0.0	0.3	2.0	2.7	3.4	4.5	5.0	6.6	7.3	7.2	6.9	7.0	8.0	8.5	
PPP(4 bunches)	3	8	33	233	233	0.0	0.1	3.2	5.1	7.9	10.2	11.6	15.3	18.7	19.9	22.4	25.1	27.5	29.8	
PPP(4 bunches)	3	8	34	234	234	0.0	2.7	7.5	11.5	14.9	18.2	19.2	24.1	27.3	31.7	36.0	40.4	44.5		
PPP(4 bunches)	3	8	35	235	235	0.0	6.7	12.1	14.6	17.7	22.5	23.0	28.4	34.8	42.5					
PPP(4 bunches)	3	8	36	236	236	0.0	8.2	12.6	16.5	17.9	22.7	24.9	32.9	40.9	48.2					
PPP(4 bunches)	3	8																		
Full blast	3	9	37	237	237	0.0	7.9	17.2	22.4	26.1	27.3	32.3	39.1							



					Velocities at time t=													
		data Set	#pulse	event #	Event	0.13	0.38	0.63	0.88	1.25	1.75	2.50	3.50	4.50	5.50	6.50	7.50	8.50
ppb(1 b, h=3, s=2.2)	3	0	101	1	1	4.8	3.2	0.8	0.8	0.8	2.2	3.1	1.2	1.0	1.3	0.8	0.8	0.4
ppb(1 b, h=3, s=2.2)	3	0	102	2	2	0.8	8.8	6.4	6.8	6.1	3.8	5.3	3.8	3.2	3.0	2.7	2.6	2.4
ppb(1 b, h=3, s=2.2)	3	0	103	3	3	3.2	14.0	7.6	7.2	7.5	5.4	7.1	5.0	3.8	5.6	3.6	4.3	3.5
ppb(1 b, h=3, s=2.2)	3	0	104	4	4	8.8	15.2	10.4	8.4	9.3	6.2	7.3	6.7	5.0	5.1	5.1	3.0	
ppb(1 b, h=3, s=2.8)	3	0	304	304	304	9.6	16.4	15.6	8.0	6.7	5.6	8.0	6.0	5.6	4.8	5.0	5.1	
ppb(1 b, h=3, s=2.8)	3	0																
ppb(1 b, h=0, s=2.2)	1	1	201	201	201	2.4	2.0	2.0	1.2	1.3	2.0	1.9	0.8	0.3	1.0	0.6	1.2	
ppb(1 b, h=0, s=2.2)	1	2	202	202	202	1.6	9.6	9.2	6.4	6.1	3.8	4.8	3.7	2.6	3.0	2.6	3.1	
ppb(1 b, h=0, s=2.2)	1	3	203	203	203	10.4	12.8	6.0	6.4	6.4	4.2	5.5	4.0	4.0	4.1	3.5	2.7	3.4
ppb(1 b, h=0, s=2.2)	1	4	204	204	204	12.8	18.4	8.4	7.2	9.3	4.8	8.0	5.9	5.6	4.4	5.0	4.4	
ppb(1 b, h=0, s=2.2)	1																	
ppb(1 b, h=0, s=2.8)	2	5	205	205	205	2.4	0.4	0.4	0.8	2.1	1.2	1.1	0.7	0.6	0.6	0.4	0.2	
ppb(1 b, h=0, s=2.8)	2	6	206	206	206	12.0	7.6	5.6	5.6	6.7	2.4	2.4	1.7	2.5	2.2	2.1	2.2	2.2
ppb(1 b, h=0, s=2.8)	2	7	207	207	207	6.4	11.2	6.0	8.8	2.9	3.2	4.4	3.6	3.0	3.0	3.3	2.9	2.2
ppb(1 b, h=0, s=2.8)	2	8	208	208	208	15.2	11.6	10.0	3.2	4.8	3.8	4.8	3.6	3.3	3.4	3.0	3.2	2.6
ppb(1 b, h=0, s=2.8)	2																	
ppb(1 b, h=0, s=3.5)	3	3	9	209	209	0.0	-1.2	1.2	1.2	1.1	0.8	0.9	0.1	0.5	-0.3	-0.1	-0.2	0.3
ppb(1 b, h=0, s=3.5)	3	3	10	210	210	4.0	6.8	4.4	4.4	6.1	2.4	2.9	1.6	1.2	1.9	2.3	1.2	2.2
ppb(1 b, h=0, s=3.5)	3	3	11	211	211	4.0	7.6	7.6	8.0	5.9	2.8	4.3	2.5	2.9	2.2	3.3	1.9	2.7
ppb(1 b, h=0, s=3.5)	3	3																
n_bunch(10Tp,<1micro))	4		203	203	203	10.4	12.8	6.0	6.4	6.4	4.2	5.5	4.0	4.0	4.1	3.5	2.7	3.4
			not 13*															
n_bunch(10Tp,<1micro	2	4	13	213	213	32.8	13.6	20.0	2.8	8.5	7.2	8.7	6.4	6.8	6.3			
n_bunch(10Tp,<1micro	2	4	14	214	214	34.4	14.0	12.0	4.8	9.1	6.6	8.1	6.8	5.6	5.8	4.5		
n_bunch(10Tp,<1micro	2	4	15	215	215	29.6	12.0	14.8	1.6	9.6	6.8	8.3	6.6	5.3	5.1	4.5		
n_bunch(10Tp,<1micro	2	4																
n_bunch(10Tp,>1micro))	5		203	203	203	10.4	12.8	6.0	6.4	6.4	4.2	5.5	4.0	4.0	4.1	3.5	2.7	3.4
n_bunch(10Tp,>1micro	2	5	17	217	217	44.8	9.2	13.6	12.8	6.9	3.8	8.4	5.8	6.2	6.5			
n_bunch(10Tp,>1micro	2	5	18	218	218	28.8	19.2	4.8	8.8	10.1	1.2	6.0	5.3	5.0	5.1	5.1	4.1	
n_bunch(10Tp,>1micro	2	5	19	219	219	26.4	17.6	6.8	12.0	4.0	5.0	7.2	5.1	5.1	3.9	5.0	4.5	
n_bunch(10Tp,>1micro	2	5																
Staggering	6		213	213	213	32.8	13.6	20.0	2.8	8.5	7.2	8.7	6.4	6.8	6.3			
Staggering	6		217	217	217	44.8	9.2	13.6	12.8	6.9	3.8	8.4	5.8	6.2	6.5			
Staggering	2	6	22	222	222	39.2	12.8	13.2	4.4	5.3	4.6	6.8	6.1	4.6	5.1	4.7	4.0	
Staggering	2	6	23	223	223	4.0	22.8	15.2	9.2	10.9	5.8	4.7	4.1	4.8	5.3	5.0	5.1	
Staggering	2	6	24	224	224	20.0	14.8	14.8	0.8	7.2	6.6	2.4	2.2	3.6	2.8	3.0	2.8	2.4
Staggering	2	6	25	225	225	20.8	12.0	7.6	7.6	6.1	5.2	4.0	1.8	2.8	3.2	2.9	2.8	4.1
Staggering	2	6	26	226	226	2.4	18.4	13.6	6.8	6.1	5.0	7.1	0.5	2.7	3.4	3.0	3.2	0.6
Staggering	2	6																
vert_scan	7	7	27	227	227	39.2	13.6	12.8	6.8	6.1	5.0	10.8	8.0	7.9	7.2			
vert_scan	7	7	28	228	228	36.0	13.6	13.6	8.8	10.9	3.4	7.7	6.1	6.7	6.0			
vert_scan	7	7	222	222	222	39.2	12.8	13.2	4.4	5.3	4.6	6.8	6.1	4.6	5.1	4.7	4.0	
			not 29*															
vert_scan	7	7	29	229	229	36.0	18.4	6.0	7.6	12.0	1.8	4.8	4.2	4.5	5.0	4.2	5.0	2.4
vert_scan	7	7	30	230	230	4.0	9.2	8.8	4.4	4.5	2.6	3.9	1.8	1.5	1.8	0.8	1.2	0.6
vert_scan	7	7	31	231	231	0.0	0.0	0.0	0.0	0.0	0.0	0.0	0.0	0.0	0.0	0.0	0.0	0.0
vert_scan	7	7																
PPP(4 bunches)	3	8	32	232	232	2.4	6.8	2.8	2.8	2.9	1.0	2.1	0.7	-0.1	-0.3	0.1	1.0	0.5
PPP(4 bunches)	3	8	33	233	233	0.8	12.4	7.6	11.2	6.1	2.8	4.9	3.4	1.2	2.5	2.7	2.4	2.3
PPP(4 bunches)	3	8	34	234	234	21.6	19.2	16.0	13.6	8.8	2.0	6.5	3.2	4.4	4.3	4.4	4.1	
PPP(4 bunches)	3	8	35	235	235	53.6	21.6	10.0	12.4	12.8	1.0	7.2	6.4	7.7				
PPP(4 bunches)	3	8	36	236	236	65.6	17.6	15.6	5.6	12.8	4.4	10.7	8.0	7.3				
PPP(4 bunches)	3	8																
Full blast	3	9	37	237	237	63.2	37.2	20.8	14.8	3.2	10.0	9.1						



## Appendix 3

### 3.1 GHMFL events logbook

Date	Time	Event #	Pressure [bar]	Field B [T]	Delta t [ms]	Pos.Inox [cm]	Pos.mirrors [cm]	Vacuum	Average speed [m/s]
9/11/2001	23:55	001	1.5	0	140			no	8.6
9/12/2001	0:15	002	1.5	0	137			no	8
9/12/2001	0:35	003	1.5	0	137			no	8
9/12/2001	0:41	004	1.5	0	137			no	8
9/12/2001	14:30	001	1.5	0	137	71	1.4	no	7.5
9/12/2001	15:45	002	1.5	0	60	71	3	yes	7.8
9/12/2001		003	1.5	0	60	71	9.4	yes	8.2
9/12/2001	20:30	004	1.5	17	60	71	4.8	yes	6.2
9/13/2001	9:26	001	2	0	140	71	19.6	no	9.1
9/13/2001	9:29	002	4	0	140	71	19.6	no	10.3
9/13/2001	9:35	003	4	0	140	71	19.6	no	
9/13/2001	10:03	004	4	0	140	71	19.6	no	10.1
9/13/2001	10:09	005	4	0	140	71	19.6	yes	11.2
9/13/2001	10:13	006	4	0	140	71	19.6	yes	12.5
9/13/2001	22:50	007	4			71	0	yes	
9/13/2001	23:01	008	4	15	160	71	0	yes	
9/13/2001	23:18	009	4	15	160	71	6.6	yes	8.3
9/13/2001	23:31	010	4	15	160	71	14.1	yes	9
9/13/2001	23:40	011	4	15	160	71	20.1	yes	
9/13/2001	23:48	012	4	15	160	71	20.1	yes	8.8
9/13/2001	23:53	013	4	19.3	160	71	20.1	yes	3.8
9/13/2001	23:56	014	4	19.3	160	71	20.1	yes	
9/13/2001	23:58	015	4	16.3	160	71	20.1	yes	5
9/14/2001	0:00	016	4	15	160	71	20.1	yes	9.8
9/14/2001	0:01	017	4	13	160	71	20.1	yes	10.8
9/14/2001	0:04	018	4	11.8	160	71	20.1	yes	10
9/14/2001	0:05	019	4	10	160	71	20.1	yes	7.7
9/14/2001	0:06	020	4	6.5	160	71	20.1	yes	7.6
9/14/2001	0:09	021	4	3.7	160	71	20.1	yes	9.6
9/14/2001	0:15	022	4	-5.5	160	71	20.1	yes	8.1
9/14/2001	0:18	023	4	-12	160	71	20.1	yes	8
9/14/2001	0:21	024	1	-9.2	160	71	20.1	yes	4.4
9/14/2001	0:25	025	4	-4.9	160	71	20.1	yes	7
9/14/2001	0:27	026	4	-12	160	71	20.1	yes	8

Event #	Pos.mirrors [cm]	Angle [deg]	Hight [mm]	Dmin [mm]	Dmax [mm]	Pos referred center [mm]	Dmin referred to center [mm]	Pos referred to position [mm]	Dmin referred to position [mm]	Jet Po [mm]	1st frame #	Last frame #	Jet length [ms]
001													
002													
003													
004													
001	1.4												
002	3												
003	9.4												
004	4.8												
001	19.6										1467	1992	65.625
002	19.6										734	1220	60.75
003	19.6										756	1190	54.25
004	19.6										745	1120	46.875
005	19.6										751	1410	82.375
006	19.6										733	1440	88.375
007	0												
008	0												
009	6.6	3.9	206	23	25	13	15	14			825	1550	90.625
010	14.1	3.6	131	11.6	25	1.6	15	8.3			675	950	34.375
011	20.1	3.0	71	8.5	19	-1.5	9	3.75			647	990	42.875
012	20.1	4.3	71	10.8	19.9	0.8	9.9	5.35			660	992	41.5
013	20.1	0.8	71	4.9	17	-5.1	7	0.95			761	918	19.625
014	20.1	2.4	71	8.4	17.6	-1.6	7.6	3			774	890	14.5
015	20.1	2.2	71	6.5	19	-3.5	9	2.75			700	937	29.625
016	20.1	3.9	71	7	22.7	-3	12.7	4.85			660	960	37.5
017	20.1	3.2	71	6.3	21.7	-3.7	11.7	4			600	990	48.75
018	20.1	2.4	71	5.2	20.7	-4.8	10.7	2.95			547	1473	115.75
019	20.1	4.6	71	10	21.5	0	11.5	5.75			494	1140	80.75
020	20.1	3.5	71	6.7	22	-3.3	12	4.35			430	2453	252.875
021	20.1	-1.6	71	5.3	10.7	-4.7	0.7	-2			541	1360	102.375
022	20.1	0.0	71	6	14	-4	4	0			460	1740	160
023	20.1	0.6	71	6	15.6	-4	5.6	0.8			553	1060	63.375
024	20.1	2.9	71	6.5	20.6	-3.5	10.6	3.55			500	1829	166.125
025	20.1	-0.4	71	6	13	-4	3	-0.5			483	1516	129.125
026	20.1	-2.0	71	4.4	10.6	-5.6	0.6	-2.5			567	1380	101.625

h 27.2

## **Appendix 2**

### **2.1 Capsule technical drawings**

## 2.2 Compatibility of mercury with other materials

Plastics														Elastomers										Metals										Non-Metal										
ABS	Acetal (Delrin)	CPVC	Epoxy	Hytrel	LDPE	HDPE	PP	PPCO	PMP	Nylon (Polyamid)	Teflon	ECTFE (Halar)	ETFE (Tefzel)	PC	PVC	PSF	PS	PVDF (Kynar)	Noryl	PPS (Ryton)	Nitrile (Buna N)	EPDM	Hypalon	Kel-F	nat. Rubber	Neoprene	Silicone	Tygon	Viton	304 stainless steel	316 stainless steel	Aluminium	Brass	Bronze	Carpenter 20	Cast iron	Copper	Hastelloy-C	Titanium	Carbon graphite	Ceramic Al2O3	Ceramic magnet		
B	A	A	A	B	A	A	A1	A1	A	A	A	A2	A2	D	A	A	D	A	A3	-	A	A	A	A	A	A	-	D	A	A	A	D	D	A	D	A	D	A	D	A2	A	C	A	A

- A** Generally considered best choice, no effect after 30 days
- A1** compatibility above 50 degrees C not available
- A2** up to 50 degree C
- A3** at Room temperature
- B** good resistance, minimal effect after 30 days
- C** only usable under control
- D** not compatible

LDPE Polyethen Low Density  
 HDPE Polyethen High Density  
 PP Polypropylen  
 PPCO Polypropylen Copolymer  
 PMP Polymethylpenten  
 Teflon FEP Fluoroethylen propylen  
 Teflon TFE Tetrafluorethen  
 Teflon PFA Perfluoroalkoxy  
 PC Polycarbonat  
 PVC Polyvinylchlorid  
 PSF Polysulfon  
 PSF Polystyrol

sources: Cole-Parmer  
 Foxboro  
 Bioblock Scientific

## 2.3 Test Procedure

### Precautions

Job must be carried out by persons instructed to handle chemical and radioactive materials. An apposite area equipped for radioactive materials has to be used during this test.

### Special equipment required

- Rubber gloves for medical use
- Coat
- Mask with filters MP3
- Thin paper overalls
- Boots
- Protective glasses
- Capsules (appositely designed)
- Amalgam powder for dental use
- Small stainless steel spoon for powder
- Stainless steel spatula for scratching Hg
- Pliers
- Pipette
- Small cylindrical brush for cleaning the capsule after usage
- Paintbrush for cleaning the capsule after usage
- Small plastic bags
- Hg vapour detector
- Hg vacuum cleaner
- White paper lables
- Hg hazard labels
- Radioactivity hazard labels
- Indelible pen
- Precision balance (3 decimals digits)
- Amalgamator for dental use
- Tool for cutting circles (10 mm)
- Plexiglas capsule holder
- Inox container
- Beker
- 2 funnels
- Small plastic glass
- Cigarette paper
- Circles stamp

## Prerequisites

- Make sure that the mercury vapor detector is working properly and calibrate it. For this purpose see instruction manual VM-3000
- The room temperature should not be above 20°C
- Remove all sources of inflammable material

## Procedure steps

1. Prepare the working area
  - Vacuum clean it
  - Provide ventilation
  - Switch the mercury vapor detector on
  - Switch the precision balance on
  - Switch the amalgamator on and set shaking + centrifugation time up
  - Collect all listed tools in the working area
  - Open the powder bottle
2. Wear safety equipment
  - Thin paper overalls
  - Gloves
  - Mask
  - Boots
  - Glasses
3. Extract mercury from the target
  - Open the Ar connection
  - Tilt the target on this side
  - Pour mercury inside the stainless steel container
  - Pour mercury inside the beker
4. Weight  $\approx 1$ g of mercury and put it into a plastic glass
  - Put the glass on the balance plate and tare it
  - Suck mercury with the pipette
  - Fill the glass with mercury
  - Extract the glass from the balance
5. Weight the same amount of powder into a plastic glass
  - Put the glass on the balance late and tare it
  - Fill it with powder using the small spoon
  - Extract the glass
6. Collect the two glasses one next to each other in order to prevent them to be mixed with other samples
7. Repeat steps 4, 5 and 6 until mercury is finished



8. Disassembly the capsule in its three components
9. Fill the powder side with weighted powder using a funnel
10. Insert the paper foil
  - Put it on the mercury side of the capsule
  - Screw the central part of the capsule on the mercury side of the capsule
11. Fill the mercury side of the capsule using a funnel
12. Reassembly the capsule
  - Turn over the powder side + central part
  - Screw the powder side + central part to the mercury side
13. Insert the capsule into the shaker according to user manual instructions
14. Shake the capsule for 3 sec (+ 3 sec centrifugation)
15. Extract the amalgam from the capsule
  - Unscrew one of the two sides of the capsule
  - Remove the paste eventually scratching it with a spatula
16. Insert the paste into a plastic bag
17. Label the bag with radioactivity labels
18. Label bag with white paper labels and write the weight of contained amalgam with the indelible pen.
19. Repeat steps from 8 to 18 for all couples of components

## 2.4 Powders' compositions

### Our powder's composition:

	Components weight percentage	Components weight [mg]
<i>Silver</i>	46.4%	185.6
<i>Tin</i>	30.0%	120
<i>Copper</i>	23.0%	92
<i>Mercury</i>	0.6%	2.4
<b>Total</b>	<b>100.0%</b>	<b>400</b>

Hg quantity: 350.0 [mg]

### Valiant's composition:

	Components weight percentage	Components weight [mg]
<i>Silver</i>	49.5	198
<i>Tin</i>	20.0	80
<i>Copper</i>	30.0	120
<i>Palladium</i>	0.5	2
<b>Total</b>	<b>100.0</b>	<b>400</b>

Hg quantity 302 [mg]

**Dispersalloy's composition:**

	Components weight percentage	Components weight [mg]
<i>Silver</i>	69.5	208.5
<i>Tin</i>	17.7	53.1
<i>Copper</i>	11.8	35.4
<i>Zinc</i>	1	3
<i>Total</i>	100.0	300

Hg quantity

300 [mg]

## 2.5 Samples' preparation logbook


Sample number	Date	Time	Powder	Shaking time [s]	Centrifugation	$\Delta$ Hg	Vacuum pumped 2 days	Sniffer control [ $\mu\text{g}/\text{m}^3$ ]					
								30 sec	1min	10min	30 min	12 hours	36 hours
1.1	29/11/01	10:45	Our	11	no	0	N	800	400	400	200	280	
1.2	29/11/01	10:50	Our	11	yes	0	N	400	300	280	120	66	
2.1	29/11/01	11:15	Our	10	no	0	N	250	200	80	60	40	43
2.2	29/11/01	14:20	Our	10	yes	0	N	150	40	35	15	130	43
3.1	29/11/01	14:50	Our	9	no	0	N	150	120	50	40	35	93
3.2	29/11/01	14:35	Our	9	yes	0	N	50	35		20	15	230
4.1	30/11/01	10:15	Our	8	no	0	N	130	110	100	50	650	135
4.2	30/11/01	10:00	Our	8	yes	0	N	450	200	60	150	65	17
4.3	30/11/01	10:28	Our	8	yes	0	N	60	40	20	15	103	26
5.1	30/11/01	16:45	Our	7	no	0	Y	120	120	80	70	200	26
5.2	30/11/01	16:55	Our	7	yes	0	Y	130	100	70	30	60	26
6.1	30/11/01	17:15	Our	3	no	0	N	100	90	60	60	100	24
7.1	3/12/01	11:58	Dispersalloy	4	yes	0	N	450	350	180	120	350	
8.1	4/12/01	13:50	Our	7	yes	5%	Y	25	25	10	17		
8.2	4/12/01	14:13	Our	7	yes	-5%	Y	100	70	30	15		
9.1	7/12/01	12:35	Valiant	10	yes	-5%	Y	150	70	60	50		
9.2	7/12/01	14:25	Valiant	10	yes	5%	Y	140	60	25	15		
9.3	7/12/01	15:00	Valiant	10	yes	0	Y						
10.1	19/12/01	17:30	Valiant	10	yes	0%	N						
10.2	19/12/01	17:35	Our	10	yes	0%	N						
11.1	17/01/02	15:28	Dispersalloy	4	yes	0%	N						
11.2	17/01/02	15:40	Dispersalloy	4	yes	5%	N						
11.3	17/01/02	15:52	Dispersalloy	4	yes	-5%	N						
11.4	17/01/02	16:03	Dispersalloy	4	yes	0%	N						

## **2.6 International Chemical Safety Cards**

# International Chemical Safety Cards

**MERCURE**

ICSC: 0056



MERCURE  
Hg  
Masse atomique : 200.6


N° CAS : 7439-97-6  
N° RTECS : OV4550000  
N° ICSC : 0056  
N° ONU : 2809  
N° CE : 080-001-00-0

TYPES DE RISQUES/ EXPOSITIONS	RISQUES/ SYMPTOMES AIGUS	PREVENTION	PREMIER SECOURS/ AGENTS D'EXTINCTION
<b>INCENDIE</b>	Non combustible. Emission de fumées (ou de gaz) irritantes ou toxiques lors d'incendie.	PAS de contact avec les substances inflammables.	En cas d'incendie à proximité: tous les agents d'extinction sont autorisés.
<b>EXPLOSION</b>	Risques d'incendie et d'explosion au contact des substances incompatibles (voir Dangers Chimiques).		En cas d'incendie: maintenir les fûts, etc., à basse température en les arrosant d'eau.
<b>CONTACT PHYSIQUE</b>		OBSERVER UNE HYGIENE STRICTE! EVITER L'EXPOSITION DES FEMMES (ENCEINTES)! EVITER L'EXPOSITION DES ADOLESCENTS ET DES ENFANTS!	DANS TOUS LES CAS, CONSULTER UN MEDECIN!
• <b>INHALATION</b>	Douleurs abdominales. Toux. Diarrhée. Essoufflement. Vomissements.	Aspiration locale ou protection respiratoire.	Air frais, repos. Respiration artificielle si nécessaire. Consulter un médecin.
• <b>PEAU</b>	PEUT ETRE ABSORBEE !	Gants de protection. Vêtements de protection.	Retirer les vêtements contaminés. Rincer et laver la peau abondamment à l'eau et au savon. Consulter un médecin.
• <b>YEUX</b>		Ecran facial, ou protection oculaire associée à une protection respiratoire.	Rincer d'abord abondamment à l'eau pendant plusieurs minutes (retirer si possible les lentilles de contact), puis

### 3 International Chemical Safety Cards

**MERCURE**

**ICSC: 0056**

<p><b>D O N N E S  I M P O R T A N T E S</b></p>	<p><b>ASPECT PHYSIQUE; APPARENCE:</b> SANS ODEUR. METAL ARGENTE LIQUIDE, LOURD ET MOBILE.</p> <p><b>DANGERS CHIMIQUES:</b> Des fumées toxiques se forment sous l'effet de la chaleur. Réagit violemment avec les métaux alcalins, l'acétylène, les azides, le gaz ammoniac, le chlore, le dioxyde de chlore, le carbure de sodium et l'oxyde d'éthylène. Attaque le cuivre et beaucoup d'autres métaux, formant des amalgames.</p> <p><b>LIMITES D'EXPOSITION PROFESSIONNELLE (LEP):</b> TLV: 0.025 mg/m<sup>3</sup> (TWA) (peau) (ACGIH 1997) MAK: 0.01 ppm; 0.1 mg/m<sup>3</sup>; (1992).</p> <p><b>VOIES D'EXPOSITION:</b> La substance peut être absorbée par l'organisme par inhalation et à travers la peau, sous forme de vapeur aussi!</p> <p><b>RISQUE D'INHALATION:</b> Une contamination dangereuse de l'air est très rapidement atteinte lors de l'évaporation de cette substance à 20°C.</p> <p><b>EFFETS DES EXPOSITIONS DE COURTE DUREE:</b> L'inhalation des vapeurs peut causer une pneumonie. La substance peut avoir des effets sur les reins et the le système nerveux central. Les effets peuvent être retardés. L'observation médicale est conseillée.</p> <p><b>EFFETS DES EXPOSITIONS PROLONGEES OU REPETEES:</b> La substance peut avoir des effets sur le système nerveux central et les reins, entraînant une instabilité émotionnelle et psychique, des tremblements mercuriels, des troubles cognitifs, des troubles du langage. Danger d'effets cumulatifs. Les tests chez l'animal montrent que cette substance peut entraîner des effets toxiques sur la reproduction chez l'homme.</p>
<p><b>PROPRIETES PHYSIQUES</b></p>	<p>Point d'ébullition : 357°C Point de fusion : -39°C Densité relative (eau = 1) : 13.5 Solubilité dans l'eau : nulle</p> <p>Tension de vapeur à 20°C : 0.26 Pa Densité de vapeur relative (air = 1) : 6.93 Densité relative du mélange air/vapeur à 20°C (air = 1) : 1.009</p>
<p><b>DONNEES ENVIRONNEMENTALES</b></p>	<p> La substance est très toxique pour les organismes aquatiques. La bioaccumulation se produit dans la chaîne alimentaire de l'homme, en particulier dans les poissons.</p>

<b>NOTES</b>	
<p>Suivant le niveau de l'exposition, une surveillance médicale périodique est recommandée. Pas d'odeur en cas de concentration toxique. NE PAS emporter de vêtements de travail chez soi.</p>	
<b>AUTRES INFORMATIONS</b>	
<b>ICSC: 0056</b>	<b>MERCURE</b>

<b>NOTICE LEGALE IMPORTANTE:</b>	<p>La CE de même que le PISSC ou toute personne agissant au nom de la CE ou du PISSC ne sauraient être tenues pour responsables de l'utilisation qui pourrait être faite de ces informations. Cette fiche exprime l'avis du comité de révision du PISSC et peut ne pas toujours refléter les recommandations de la législation nationale en la matière. L'utilisateur est donc invité à vérifier la conformité des fiches avec les prescriptions en usage dans son pays.</p> <p>Traduction autorisée de l'International Chemical Safety Card (ICSC), publié par l'UNEP/ILO/WHO dans le cadre de la coopération entre le PISSC et la CE. Programme International sur la Sécurité des Substances Chimiques - Commission Européenne, 1993.</p>
--------------------------------------	---



## Symbols and abbreviations

Symbol	Unit	Constant values	Explanation
c	m/s	$c=3\cdot 10^8$ m/s	speed of light
B	T	$1\text{T}=1\text{ V}\cdot\text{s}/\text{m}^2$	magnetic flux density
E	eV	$1\text{ eV}=1.6\cdot 10^{-19}\text{J}$	energy
f	Hz		frequency
I	a		electrical current
l	m		distance
m	$\text{eV}/c^2$	$1\text{ eV}/c^2=1.8\cdot 10^{-36}$ kg	mass
P	W		power
t	s		time
p	Pa		pressure
Z	g/mol		atomic mass
T	C, K		temperature
v	m/s		velocity
$\alpha_v$	1/K		thermal expansion coeff.
k	$\text{m}^2/\text{N}$		compressibility
$\rho$	$\text{kg}/\text{m}^3$		density
d	m		diameter
$\lambda$	s		life time
p	kg m/s		momentum

## Terms and Abbreviations

<b>Abbreviation</b>	<b>Meaning</b>
BNL	Brokenhven National Laboratory
LHC	Large Hadron Collider
LEP	Large Electron Positron collider
LINAC	LINear ACcelerator
ISOLDE	Isotope Separator On Line DEvice
SLAC	Stanford Linear Accelerator Center
HARP	Hadron Production Experiment
CNGS	CERN Neutrino to Gran Sasso
SPL	Superconducting Proton Linac
NFWG	Neutrino Factory Working Group
ppb	protons per bunch
ppp	protons per pulse
RF cavity	Radio Frequency cavity
GHMFL	Grenoble High Magnetic Field Laboratory
DONUT	Direct Observation of the Nu Tau
Fps	frames per second
MHD	MagnetoHydroDynamic
HDPE	High Density Poly Ethylene
PVC	Poly Vinyl Chloride
BSE	Back Scattered Electrons
SE	Secondary Electrons